nature cancer

Article

https://doi.org/10.1038/s43018-024-00736-x

Targeting PRMT9-mediated arginine methylation suppresses cancer stem cell maintenance and elicits cGAS-mediated anticancer immunity

Received: 16 October 2022

Accepted: 26 January 2024

Haojie Dong[1,20], Xin He[1,20], Lei Zhang[1,20], Wei Chen[2], Yi-Chun Lin[3], Song-Bai Liu[4], Huafeng Wang[5], Le Xuan Truong Nguyen[1], Min Li[6], Yinghui Zhu[1], Dandan Zhao[1], Lucy Ghoda[1], Jonathan Serody[7,8], Benjamin Vincent[7,9], Leo Luznik[10], Ivana Gojo[10], Joshua Zeidner[7], Rui Su[11], Jianjun Chen[11], Ritin Sharma[12,13], Patrick Pirrotte[12,13], Xiwei Wu[2,14], Weidong Hu[15], Weidong Han[16], Binghui Shen[17], Ya-Huei Kuo[1], Jie Jin[5], Amandeep Salhotra[18], Jeffrey Wang[3], Guido Marcucci[1,18], Yun Lyna Luo[3] & Ling Li[1,19] ✉

Current anticancer therapies cannot eliminate all cancer cells, which hijack normal arginine methylation as a means to promote their maintenance via unknown mechanisms. Here we show that targeting protein arginine *N*-methyltransferase 9 (PRMT9), whose activities are elevated in blasts and leukemia stem cells (LSCs) from patients with acute myeloid leukemia (AML), eliminates disease via cancer-intrinsic mechanisms and cancer-extrinsic type I interferon (IFN)-associated immunity. PRMT9 ablation in AML cells decreased the arginine methylation of regulators of RNA translation and the DNA damage response, suppressing cell survival. Notably, PRMT9 inhibition promoted DNA damage and activated cyclic GMP-AMP synthase, which underlies the type I IFN response. Genetically activating cyclic GMP-AMP synthase in AML cells blocked leukemogenesis. We also report synergy of a PRMT9 inhibitor with anti-programmed cell death protein 1 in eradicating AML. Overall, we conclude that PRMT9 functions in survival and immune evasion of both LSCs and non-LSCs; targeting PRMT9 may represent a potential anticancer strategy.

The outcomes for patients with acute myeloid leukemia (AML) remain poor[1]. Allogeneic hematopoietic stem cell transplantation has emerged as the only cure. However, its applicability is restricted[2]. Success of immunotherapies has driven interest in developing effective antileukemia drugs, including immune checkpoint inhibitors (ICIs)[3–5]. However, translation of existing T cell-leveraging strategies to AML treatment remains challenging.

The cyclic GMP-AMP synthase (cGAS)–stimulator of interferon genes (STING) signaling triggers the type I interferon (IFN) response[6] and can prime T cell function. Specifically, preexisting functional T cells are required for responses to ICI treatment[6]. cGAS activity is stimulated by cytosolic DNA and generates cyclic GMP-AMP (cGAMP)[7,8]. Notably, cGAMP exported from tumor cells serves as an ‘immunotransmitter’ to activate the STING receptor on dendritic cells (DCs), which then

---

A full list of affiliations appears at the end of the paper. ✉e-mail: lingli@coh.org

activates the production of type I IFN[8]. Moreover, administration of the STING agonist blocked AML development in in vivo models[7]. However, STING agonists show only modest clinical benefits[9]. To address this challenge, we are developing a strategy based on stimulating cancer-endogenous cGAS.

Protein arginine methylation is a posttranslational modification functioning in cellular processes[10]. Protein arginine methyltransferases (PRMTs) have emerged as druggable targets. Accordingly, inhibitors of two major PRMTs to treat malignancies are under clinical trials. However, one concern is that PRMT1 and PRMT5 are responsible for most arginine methylation of essential histone markers[10]. Therefore, the relevance of other individual PRMTs to different cancers should be considered. PRMT9 is the less-known PRMT. In this study, we performed analyses that supported PRMT9 as a potential target and developed an inhibitory compound as a tool to probe PRMT9 activity.

Results

PRMT9 levels are elevated in leukemia stem cells

We assessed PRMT levels using The Cancer Genome Atlas (TCGA) program and cancer cell lines proteomic datasets[11,12]. Among deadly cancers[13], AML showed the highest *PRMT9* mRNA levels (Fig. 1a,b and Extended Data Fig. 1a). Other PRMTs showed comparable levels in AML and other cancers (Fig. 1a and Extended Data Fig. 1b–n). We observed elevated PRMT9 protein levels in AML relative to other cancers (Fig. 1b and Extended Data Fig. 1o,p). We next assessed all PRMT levels using a dataset that included transcriptome from leukemia and normal hematopoietic stem and progenitor cells (HSPCs)[14]. Notably, *PRMT9* levels were higher in leukemia stem cells (LSCs) relative to either normal hematopoietic stem cells (HSCs) or blasts (Fig. 1c). We next performed single-cell RNA sequencing (scRNA-seq) analysis on murine leukemic bone marrow from an MLL-AF9 (MA9) cKit$^+$ cell transplant mouse model. Among the leukemia cells, we identified two clusters as LSCs and blasts (Fig. 1d,e and Extended Data Fig. 1q)[15]. Notably, *Prmt9* was the only *Prmt* whose levels showed more than a onefold increase in LSCs relative to blasts (Fig. 1f). Next, we assessed PRMT9 levels in AML specimens and normal healthy donors (peripheral blood stem cells (PBSCs)). Notably, elevated PRMT9 protein levels were seen in an LSC-enriched (CD34$^+$CD38$^-$) relative to a leukemia committed progenitor (CD34$^+$CD38$^+$) subset or to either of the normal subsets (Fig. 1g). We also found that PRMT9 protein levels were higher in the AML CD34$^+$ subsets ($n = 30$; Supplementary Table 1) relative to the normal counterparts ($n = 10$) (Fig. 1h,i). Analysis of CD34$^+$ cells from another cohort with AML ($n = 94$; Supplementary Table 2) and normal donors ($n = 19$) confirmed *PRMT9* upregulation (Extended Data Fig. 1r). Analysis of another dataset ($n = 463$) showed similar results (Extended Data Fig. 2a). *PRMT9* levels were not associated with any particular cytogenetic abnormality or mutation (Extended Data Fig. 2b–d). PRMT9 protein levels were also higher in diffuse large B cell lymphoma (DLBCL) cell lines (Extended Data Fig. 1o,e)[11]. We also found that higher *PRMT9* levels predicted shorter overall survival (Fig. 1j,k). Analysis of the pediatric dataset yielded similar results (Extended Data Fig. 2f).

We next analyzed chromatin immunoprecipitation followed by sequencing (ChIP–seq) data in ChIPBase v.2.0 (ref. 16) and observed the binding sites of relevant transcription factors within 5 kb upstream of the *PRMT9* transcription start site. *CREB1*, a known prognosticator[17], showed the strongest correlation with *PRMT9* expression in the AML and DLBCL cohorts (Extended Data Fig. 2g,h). Interestingly, we observed an increase in *Creb1* in MA9 LSCs relative to blasts (Extended Data Fig. 2i). *CREB1* inhibition decreased *PRMT9* levels (Extended Data Fig. 2j). We next verified the significant enrichment of *CREB1* in Molm13 cells at the *PRMT9* promoter region relative to a control site (Extended Data Fig. 2k,l); the promoter region showed significant enrichment of H3K27Ac relative to normal cells (Extended Data Fig. 2l).

PRMT9 is dispensable for normal hematopoiesis

PRMT9 levels were higher in HSPCs than in mature lineages[18] (Extended Data Fig. 2m,n). We developed a conditional knockout (KO) model by crossing *Prmt9$^{loxP/loxP}$* with *Mx1-Cre* mice (*Mx1-Cre/Prmt9$^{loxP/loxP}$* or *Prmt9-cKO*). In this model, the *Prmt9 exon2* was flanked by *loxP* sites (Extended Data Fig. 2o). Sixteen weeks after pIpC administration, we observed no differences in complete blood count between *Prmt9-cKO* mice and littermate (*Prmt9$^{loxP/loxP}$*) controls. *Prmt9* KO modestly increased the multipotent progenitor population and did not affect mature cells (Extended Data Fig. 2p,q). To evaluate the repopulation capacity of HSPCs with *Prmt9* KO, we performed a competitive transplantation. *Prmt9* KO modestly affected CD45.2 chimerism in recipients relative to controls (Extended Data Fig. 2r), suggesting that *Prmt9* function is modestly required for HSPC self-renewal under transplantation stress.

PRMT9 ablation impairs cancer cell survival

We generated *Prmt9*-cKO/MA9 mice. We observed that *Prmt9* levels are elevated in MA9 mouse bone marrow cKit$^+$ cells (Fig. 2a). Given that other oncogenes cooperate with MA9 cells to induce AML[19–21], we assessed the effects of *Prmt9* KO in both MA9 single-hit and double-hit models; for the latter, we used *FLT3*-internal tandem duplication (ITD) as the second hit[22,23]. Specifically, we transduced Lin$^-$Sca-1$^+$cKit$^+$ bone marrow cells from *Prmt9*-cKO/MA9 or control (*Prmt9* WT/MA9) mice with

Fig. 1 | PRMT9 levels are elevated in AML. a, PRMTs mRNA levels in the most deadly cancer types from the TCGA PanCancer Atlas. AML ($n = 173$), lung adenocarcinoma (LUAD) ($n = 510$), lung squamous cell carcinoma (LUSC) ($n = 484$), colon adenocarcinoma (COAD) ($n = 438$), pancreatic adenocarcinoma (PAAD) ($n = 177$), breast cancer (BRCA) ($n = 1{,}082$), prostate adenocarcinoma (PRAD) ($n = 493$), liver hepatocellular carcinoma (LIHC) ($n = 366$), glioblastoma (GBM) ($n = 160$) and bladder carcinoma (BLCA) ($n = 407$). *Z*-scores were determined based on the average expression of each PRMT. PRMT8 was undetectable (*n* represents the number of tissue samples; https://www.cbioportal.org/). **b**, PRMT9 protein levels in AML relative to other cancer lines. Data were from the DepMap portal (https://DepMap.org/portal/). AML ($n = 10$), lung cancer ($n = 75$), COAD ($n = 29$), PAAD ($n = 17$), BRCA ($n = 29$), PRAD ($n = 5$), LIHC ($n = 12$), GBM ($n = 11$), BLCA ($n = 9$) and acute lymphoblastic leukemia (ALL) ($n = 8$). The *P* value was determined using an unpaired two-sided *t*-test (*n* represents the number of different cancer cell lines. **c**, Top: PRMTs mRNA levels in normal hematopoietic subsets from healthy donors ($n = 7$) or leukemia subsets from patients with AML ($n = 21$) in GSE63270. *Z*-scores were determined based on the average expression of each PRMT. Bottom: the violin plots show *PRMT9* expression in LSCs versus normal HSCs and in LSCs versus leukemia blasts. The LSC versus HSC *P* value was determined using an unpaired two-sided *t*-test. The LSC versus blast *P* value was determined using a paired two-sided *t*-test (*n* represents the number of patients). CMP, common myeloid progenitor; GMP, granulocyte-monocyte progenitor; LMPP, lympho-myeloid primed progenitor; MEP, megakaryocytic-erythroid progenitor; MPP, multipotent progenitor. **d**, Fifty representative genes from the MA9 mouse LSC signature. scRNA-seq of MA9 mouse bone marrow (same dataset in Fig. 5h). **e**, LSC and blast clusters from **d**. Shown are representative LSC gene (*Cbx5*) and *Prmt9* levels. **f**, Average fold change in all *Prmt* levels in an LSC versus a blast cluster based on **e**. **g**, Intracellular staining of PRMT9 in CD34$^+$CD38$^-$ or CD34$^+$CD38$^+$ populations in PBSCs from individuals with AML ($n = 3$ individuals) or normal PBSCs. **h**, PRMT9 protein levels in AML CD34$^+$ ($n = 30$) versus normal PBSC ($n = 10$) counterparts. **i**, Quantitative summary of **h**. The *P* value was determined using an unpaired two-sided *t*-test (*n* represents the number of patients or healthy donors). **j**, Kaplan–Meier survival analysis of the in-house AML cohort (Supplementary Table 2; $n = 94$) after dichotomization for median *PRMT9* mRNA levels. **k**, Kaplan–Meier survival analysis of another cohort (GSE12417) after dichotomization for *PRMT9* levels below (black, $n = 74$) or above (red, $n = 89$) 9.62 $\log_2$-transformed intensity. The threshold was discovered by classifying patients into two clusters using the partitioning around medoids algorithm. *P* values were determined using a log-rank (Mantel–Cox) test (*n* represents the number of patients).

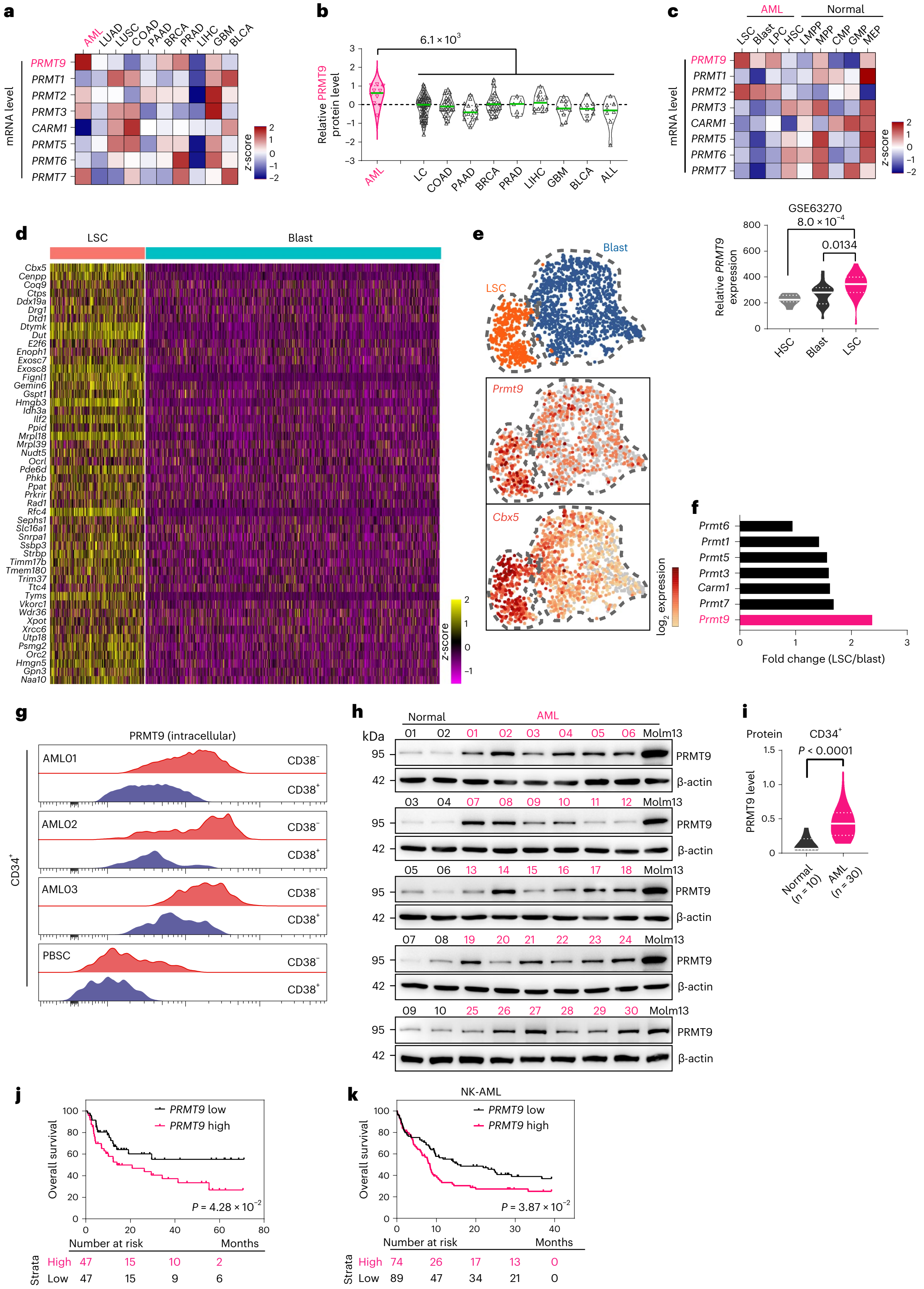
a
AML
LUAD
LUSC
COAD
PAAD
BRCA
PRAD
LIHC
GBM
BLCA
mRNA level
PRMT9
PRMT1
PRMT2
PRMT3
CARM1
PRMT5
PRMT6
PRMT7
z-score
2
1
0
−1
−2
b
6.1 × 10^3
Relative PRMT9 protein level
3
2
1
0
−1
−2
−3
AML
LC
COAD
PAAD
BRCA
PRAD
LIHC
GBM
BLCA
ALL
c
AML
Normal
LSC
Blast
LPC
HSC
LMPP
MPP
CMP
GMP
MEP
mRNA level
PRMT9
PRMT1
PRMT2
PRMT3
CARM1
PRMT5
PRMT6
PRMT7
z-score
d
LSC
Blast
Cbx5
Cenpp
Coq9
Ctps
Ddx19a
Drg1
Dtd1
Dtymk
Dut
E2f6
Enoph1
Exosc7
Exosc8
Fignl1
Gemin6
Gspt1
Hmgb3
Idh3a
Ilf2
Ppid
Mrpl18
Mrpl39
Nudt5
Ocrl
Pde6d
Phkb
Ppat
Prkrir
Rad1
Rfc4
Sephs1
Slc16a1
Snrpa1
Ssbp3
Strbp
Timm17b
Tmem180
Trim37
Ttc4
Tyms
Vkorc1
Wdr36
Xpot
Xrcc6
Utp18
Psmg2
Orc2
Hmgn5
Gpn3
Naa10
z-score
2
1
0
−1
e
Blast
LSC
Prmt9
Cbx5
log2 expression
GSE63270
8.0 × 10^−4
0.0134
Relative PRMT9 expression
800
600
400
200
0
HSC
Blast
LSC
f
Prmt6
Prmt1
Prmt5
Prmt3
Carm1
Prmt7
Prmt9
0
1
2
3
Fold change (LSC/blast)
g
PRMT9 (intracellular)
CD34+
AML01
AML02
AML03
PBSC
CD38−
CD38+
h
kDa
Normal
AML
01 02 01 02 03 04 05 06 Molm13
03 04 07 08 09 10 11 12 Molm13
05 06 13 14 15 16 17 18 Molm13
07 08 19 20 21 22 23 24 Molm13
09 10 25 26 27 28 29 30 Molm13
95
42
PRMT9
β-actin
i
Protein
CD34+
P < 0.0001
PRMT9 level
1.5
1.0
0.5
0
Normal (n = 10)
AML (n = 30)
j
PRMT9 low
PRMT9 high
Overall survival
100
80
60
40
20
0
P = 4.28 × 10^−2
0
20
40
60
80
Number at risk
Months
Strata
High 47 15 10 2
Low 47 15 9 6
k
NK-AML
PRMT9 low
PRMT9 high
Overall survival
P = 3.87 × 10^−2
0
10
20
30
40
Number at risk
Months
Strata
High 74 26 17 13 0
Low 89 47 34 21 0

either a lentiviral vector expressing *FLT3*-ITD and coexpressing green fluorescent protein (GFP). Relative to the controls, colony-forming cell (CFC) growth was inhibited in *Prmt9* KO *MA9*$^+$ bone marrow cells; more inhibition by *Prmt9* KO was seen in *FLT3*-ITD-expressing cells than in mock cells (Fig. 2b,c and Extended Data Fig. 3a). Additionally, we also transduced a doxycycline (DOX)-inducible *Prmt9* knockdown (KD) construct into MA9 cells. Those inducible constructs coexpressed red fluorescent protein (RFP) (Extended Data Fig. 3b). Consistent with the effect of *Prmt9* KO, *Prmt9* KD significantly inhibited CFC growth of MA9 and MA9/*FLT3*-ITD bone marrow cells (Extended Data Fig. 3c,d). Besides the MA9 model, we evaluated outcomes by inducing *Prmt9* KD in another CBFB-MYH11 knock-in AML model plus thrombopoietin receptor transduction (namely, CMM)[24,25] resembling inv (16) AML. *Prmt9* levels were significantly elevated in the AML cells (Fig. 2a). *Prmt9* KD inhibited the CFC growth of CMM cells (Extended Data Fig. 3c,d). *Prmt9* KD decreased LSC frequency, as shown in an in vitro limiting dilution assay[26–28], in all three models (Extended Data Fig. 3e–g).

We transduced MA9/*FLT3*-ITD double-hit *Prmt9* control KO cells (or controls) with a luciferase reporter. Compared to control mice, *Prmt9*-deficient mice had a slower AML progression, lower tumor burden, decreased splenomegaly and survival advantage (Fig. 2d–h).

We next assessed PRMT9 function in human cancers. KD of *PRMT9* (shPRMT9-1, shPRMT9-2) decreased cell growth and viability (Extended Data Fig. 3h–k). We also engineered Molm13 cells to express either a wild-type (WT) *PRMT9* or corresponding catalytically dead mutant[29]; both were designed to resist *PRMT9* short hairpin RNA (shRNA) 1 (that is, PRMT9/WT-R and PRMT9/MUT-R; Fig. 2i). Notably, unlike transduction with PRMT9/MUT-R, PRMT9/WT-R reversed the inhibition seen after *PRMT9* KD (Fig. 2j,k), indicating the requirement for catalysis. Moreover, *PRMT9* KD decreased the viability of AML CD34$^+$ cells more potently than it did with normal counterparts (Fig. 2l–o and Extended Data Fig. 3l). Molm13 cells with the DOX-inducible shPRMT9 construct were transplanted into NOD scid gamma (*NSG*) mice (Extended Data Fig. 3m). Once engraftment was confirmed (>1% in peripheral blood), DOX was administered (Fig. 2p). Notably, mice receiving *PRMT9* KD cells exhibited decreased leukemia burden and prolonged survival, compared with control mice (Fig. 2q,r).

PRMT9-mediated methylation promotes cell growth

We performed stable isotope labeling by amino acids in cell culture (SILAC)-based proteomics analysis on inducible shPRMT9-transduced or shCtrl-transduced Molm13 cells (Fig. 3a and Supplementary Tables 3 and 4). The analysis revealed 315 unique mono-methylation arginine (MMA) and 109 dimethylation arginine (DMA) sites. *PRMT9* KD resulted in marked downregulation of 16 (14.7%) DMA and 31 (9.8%) MMA sites (Fig. 3b, fold change > 1.5) in 23 unique proteins (Fig. 3c and Supplementary Table 4). However, iceLogo analysis[30,31] did not detect any consensus sequences enriched in methyl peptides (Extended Data Fig. 4a). Among 23 proteins, ten functioned in RNA translation, seven were related to the DNA damage response and six were related to RNA catabolism (Fig. 3d and Supplementary Table 5).

We next asked whether PRMT9 regulates translation. Specifically, a sucrose density gradient assay revealed that *PRMT9* KD decreased polysome-related mRNAs levels, indicating insufficient mRNA translation[32] (Fig. 3e). Next, through an O-propargyl-puromycin (OPP)-based assay[33], we found decreased global protein synthesis after *PRMT9* KD in cancer cells (Fig. 3f and Extended Data Fig. 4b–d), while protein synthesis in normal CD34$^+$ cells was modestly altered (Fig. 3f and Extended Data Fig. 4b). *PRMT9* KD downregulated the levels of short-lived proteins (Supplementary Table 3), while their mRNA levels were unchanged (Fig. 3g and Extended Data Fig. 4e). We also observed that *PRMT9* KD shifted *c-Myc* and *SAMHD1* transcripts from high-molecular-weight (HMW) to low-molecular-weight (LMW) polysomes (Fig. 3h and Extended Data Fig. 4f).

Among the downregulated methylated peptides we identified, the methylated PABPC1 peptide with dimethyl-R493 (R493me2), was most depleted by *PRMT9* KD (Fig. 3i). Posttranslational modifications of PABPC1 are critical for its function[34,35]. We thus defined PABPC1 as a PRMT9 substrate. Analysis of PABPC1 peptides in *PRMT9* KD versus PRMT9 WT cells revealed two more sites, monomethylation at R481 (R481me) and R506 (R506me), enriched in PRMT9 WT cells (Fig. 3j and Extended Data Fig. 4g,h). To validate the modifications, we constructed a FLAG-tagged PABPC1 C-terminal fragment (amino acids 476–636, PABPC1-CT) containing R481, R493 and R506, as well as a corresponding methylation-deficient (R to K) construct for each individual residue (R481K, R493K, R506K) or for all three residues (3RK). Only the 3RK mutation depleted PABPC1-CT methylation (Extended Data Fig. 4i). We next performed an in vitro methylation assay by incubating the glutathione *S*-transferase (GST)-PABPC1 fragment and full-length Myc-tagged PRMT9 (Extended Data Fig. 4j) or other PRMTs with SAM. Only PRMT9 promoted PABPC1-CT methylation (Fig. 3k, Extended Data Fig. 4k,l). We confirmed the methylation by an ex vivo tritium methylation assay (Extended Data Fig. 4m). Moreover, when we incubated a synthesized peptide containing R493 with PRMT9 and *S*-adenosyl methionine (SAM), the signal was only seen with either anti-symmetric dimethylarginine (SDMA) or anti-MMA antibody (Fig. 3l).

To assess the function of PABPC1 methylation, we ectopically expressed full-length PABPC1 WT, PABPC1-3RK or the PABPC1-R493K mutant, which are resistant to shPABPC1, and further knock down endogenous PABPC1 (Fig. 3m). WT PABPC1 rescued the *PABPC1* KD phenotypes; 3RK or R493K marginally rescued the outcomes seen after *PABPC1* KD (Fig. 3n,o). Moreover, cells expressing R493K exhibited impaired protein synthesis to the same extent as cells expressing 3RK. R493 is located in the region that mediates PABPC1 self-association on

Fig. 2 | PRMT9 ablation impairs cancer cell survival. **a**, Prmt9 levels in cKit$^+$ bone marrow cells from MA9 and CMM mice relative to normal counterparts (*n* = 2 independent experiments). **b**,**c**, CFC of MA9 and MA9-ITD cells after *Prmt9* KO (*n* = 5 independent cultures). **b**, Colony number after *Prmt9* deletion induction, as described previously[76]. Data represent the mean ± s.d. The *P* value was determined using an unpaired two-sided *t*-test. **c**, KO efficiency. **d**,**e**, MA9-ITD-luciferase cells (0.5×10^6 cells per transplant) were injected into irradiated recipients (*n* = 5 mice per group). After engraftment, mice were treated with pIpC and assessed for engraftment using imaging (**e**). **d**, Quantitative results. Data represent the mean ± s.e.m. *P* values were established using a two-way analysis of variance (ANOVA). Color bar, luminescence radiance (photons s^{-1} cm^{-2} sr^{-1}). **f**,**g**, Another cohort established as **d**, at the endpoint, spleen (**f**) of *Prmt9* KO and control mice was checked, and engraftment was evaluated based on the percentage of CD45.2$^+$ cells (**g**) (*n* = 5 mice per group). Data represent the mean ± s.e.m. **g**, The *P* value was determined using an unpaired two-sided *t*-test. **h**, Survival analysis of MA9-ITD transplants (*n* = 5 mice per group) on *Prmt9* KD. The *P* value was determined using a log-rank (Mantel–Cox) test. **i**–**k**, Molm13 were transduced with mock or *PRMT9* WT or *PRMT9* mutant vectors resistant to shPRMT9; PRMT9 expression was detected after endogenous PRMT9 was knocked down (**i**) (*n* = 2 independent experiments). Cell viability (**j**) using an MTS assay, and apoptosis (**k**), based on annexin V staining (**j**,**k**, *n* = 6 independent experiments). **j**,**k**, Data represent the mean ± s.d. The *P* value was determined using a one-way ANOVA. **l**–**o**, AML CD34$^+$ (*n* = 11 patients) or PBSC CD34$^+$ (*n* = 3 healthy donors) cells were transduced with shPRMT9. Cell viability (**l**) and apoptosis (**m**,**n**) are shown. *PRMT9* levels were evaluated using quantitative PCR (qPCR) analysis (**o**). **l**,**n**,**o**, Data represent the mean ± s.d. **l**,**n**, *P* values were determined using an unpaired, two-sided *t*-test. **p**,**q**, Molm13 cells transduced with a DOX-inducible shPRMT9 were transplanted into *NSG* mice (control, *n* = 8 mice; *PRMT9* KD, *n* = 7 mice). KD efficiency was evaluated (**p**). After engraftment, mice were treated with DOX to induce *PRMT9* KD and engraftment was evaluated based on the percentage of human CD45 cells (**q**). Data represent the mean ± s.e.m. **q**, The *P* value was determined using an unpaired two-sided *t*-test. **r**, In parallel, survival was analyzed. **r**, *P* was determined using a log-rank (Mantel–Cox) test.

the 3′ RNA poly(A) tail[36]; thus, we asked if R493 methylation favored self-interaction (Fig. 3p). Notably, R493K pulled down less hemagglutinin (HA)-tagged PABPC1 than PABPC1 WT (Fig. 3q). Next, we performed a poly(A) agarose pull-down assay to evaluate whether R493 methylation altered PABPC1 binding to poly(A)[34]. Less FLAG-tagged PABPC1 was pulled down from R493K-expressing cells than from PABPC1-WT-expressing cells (Fig. 3r). Furthermore, because R493 is near the PABPC1 C terminus (amino acids 541–636), we asked

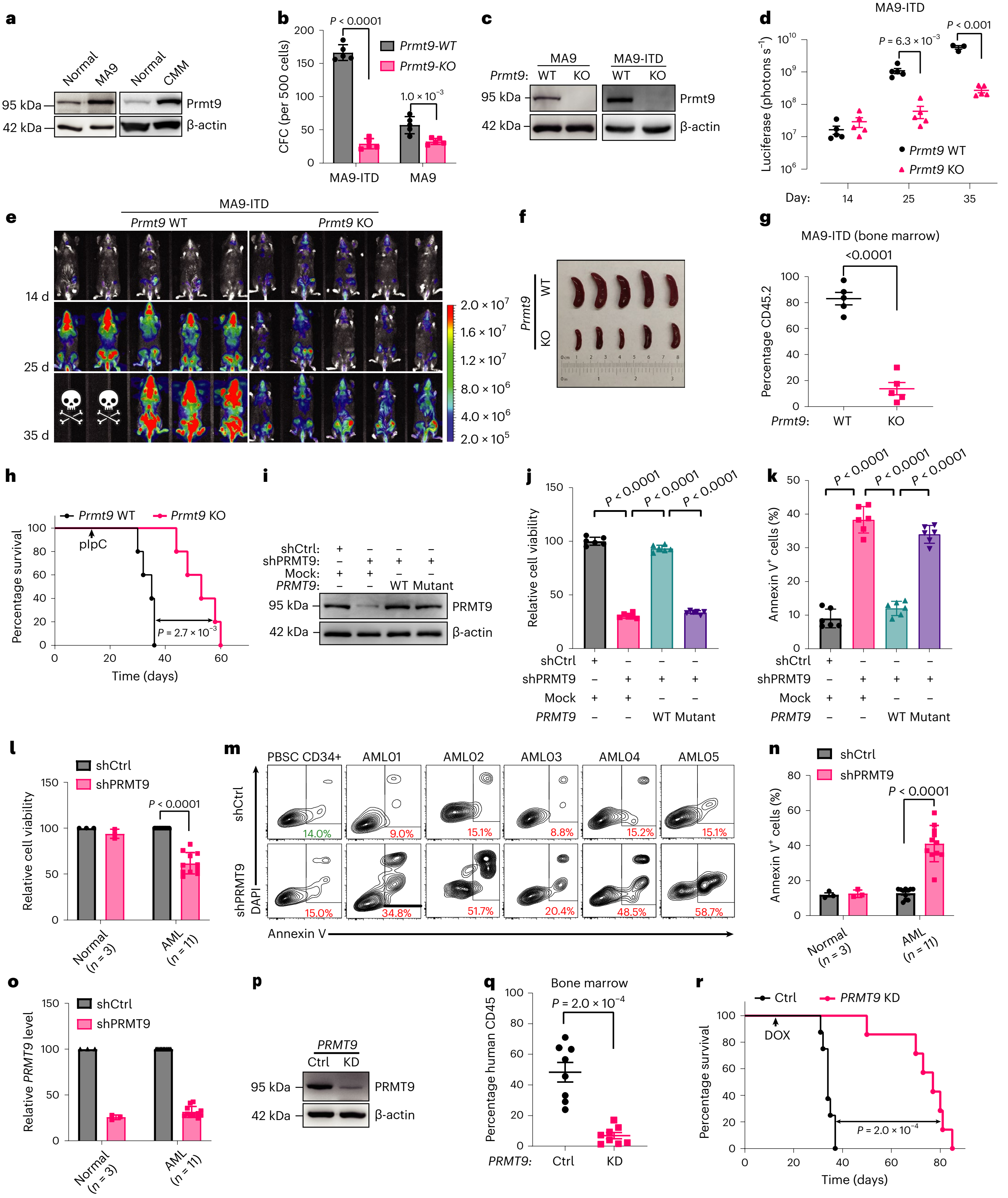

if R493 methylation facilitated binding of the C terminus to other translational factors, such as eRF3 (ref. 37). We analyzed the interaction of FLAG-tagged PABPC1 variants with Myc-tagged eRF3 using co-immunoprecipitation (co-IP). R493K exhibited less affinity to eRF3 than PABPC1 WT (Fig. 3s). In contrast, R493K did not alter the PABPC1 interaction with eIF4G (Extended Data Fig. 4n), which binds to the N terminus[38].

We next generated an antibody to detect symmetrically dimethylated R493 (R493me) (Fig. 3t). Moreover, mutation of only R493, but not R481 or R506, completely abolished the methylation signals (Extended Data Fig. 4o). Knockdown of endogenous *PRMT9* blocked PABPC1 R493 methylation but not R455 or R460 methylation (Fig. 3u and Extended Data Fig. 4p), while *PRMT9* overexpression increased R493 methylation (Extended Data Fig. 4q). Moreover, inhibitors of other PRMTs did not alter R493 methylation levels (Extended Data Fig. 4r,s). CARM1 catalyzed PABPC1 R455 and R460 methylation did not cross-regulate R493 methylation (Supplementary Fig. 1a,b). Consistent with other reports[35], CARM1-dependent methylation did not alter RNA translation (Supplementary Fig. 1c,d).

We sorted the leukemia CD34$^+$ subset and CD34$^-$CD33$^+$ blasts from specimens ($n = 7$; Extended Data Fig. 5a–c). Notably, CD34$^+$ cells expressed higher PRMT9 and R493me levels than blasts (Fig. 3v). R493me and PRMT9 levels were positively correlated (Fig. 3w). We conducted similar analyses in MA9 and CMM cells and observed higher PRMT9 and R493me levels in cKit$^+$ cells relative to cKit$^-$ cells (Extended Data Fig. 5d,e).

Identification of a PRMT9 inhibitor

We performed virtual screening. Briefly, we screened compounds for binding affinity to PRMT9; compounds were from the National Cancer Institute (NCI) and ZINC library (Fig. 4a,b). According to the highest binding affinity to the catalytic pocket, we identified top candidates to assess their activity. We used doses of 1 and 5 µM in a Molm13 cell-based viability assay (Extended Data Fig. 6a). We selected the top 20 compounds exhibiting robust cell inhibitory effects for further analysis (Fig. 4c). Specifically, we assessed their effects on PRMT9 catalysis (Extended Data Fig. 6b). Of the 20 compounds tested, three structurally similar compounds showed PRMT9 inhibition (Extended Data Fig. 6c). Among the three, NSC641396 showed the highest inhibition effects (Extended Data Fig. 6d,e).

The NSC641396 docking pose indicated that the quinone ring next to the carbazole moiety extended outside the hydrophobic pocket (Extended Data Fig. 6f). We then conducted a Tanimoto-based two-dimensional similarity search after removing the quinone ring and introducing heteroatoms at different locations of the carbazole moiety (Extended Data Fig. 6g), which yielded 69 compounds. The top nine were purchased; only nos. 1, 2 and 8 showed PRMT9 inhibition efficacy superior to or similar to that of NSC641396, with no. 1 (thereafter called LD2) being the most potent (Fig. 4d,e). Next, we confirmed direct LD2 interaction with PRMT9 protein using nuclear magnetic resonance (NMR) (Fig. 4f,g and Supplementary Table 6). We also assessed the intracellular interaction of the compound and PRMT9 protein using a cellular thermal shift assay[39,40]. Specifically, we engineered Molm13 cells to overexpress FLAG-tagged PRMT9 WT or PRMT9 mutant (W152A, D258A and E433A). All three residues were predicted LD2 binding sites (Fig. 4e). Notably, LD2 treatment led to substantial shifts in the thermal stability of PRMT9 WT but not PRMT9 mutant (Fig. 4h,i).

LD2 treatment preferentially inhibited the viability of cancer cells (Fig. 4j and Extended Data Fig. 6h) and their protein synthesis (Fig. 4k). LD2 at a relatively low dose decreased PRMT9 activity while sparing other PRMTs (Fig. 4l and Extended Data Fig. 6i–j). At a relatively high dose (20 µM), LD2 treatment slightly decreased PRMT5 activity (Supplementary Fig. 2). We also performed docking analysis of LD2 into CARM1, PRMT5, PRMT7 and PRMT9. The relatively lower docking score suggested that LD2 binds PRMT9 (-7.15 kcal mol^{-1}) with greater affinity than the other PRMTs tested (Extended Data Fig. 6k). Molecular dynamic simulation analyses confirmed the stronger binding of PRMT9 by LD2 (Extended Data Fig. 6l). Finally, *PRMT9* KD in Molm13 cells reduced their sensitivity to LD2 (at 2.5 µM), suggesting that the LD2 effects at that dose are PRMT9-dependent (Extended Data Fig. 6m).

Next, we treated mononuclear cells (MNCs) from the AML specimens for 4 days[41] with LD2 (2.5 µM) under physiological cytokine conditions[42] and then performed cytometry by time-of-flight (CyTOF) analysis. The bone marrow subsets (Supplementary Figs. 3–5) in the vehicle group exhibited modest levels of apoptosis. AML cells from patients ($n = 3$) exhibited expansion of the immature CD34$^+$CD45$^{\mathrm{dim}}$ subset (Fig. 4m). In these immune and leukemia cell cocultures, LD2 treatment ablated leukemia cells and relatively increased the T cell ratio (Fig. 4m, Extended Data Fig. 6n,o and Supplementary Fig. 4). Notably, LD2 treatment expanded the number of IFN-γ-expressing T cells relative to vehicle controls (Supplementary Fig. 6). We also depleted autologous CD3$^+$ T cells of the AML samples ($n = 3$) before treatment (Fig. 4n). Notably, the inhibitory effects of LD2s were partially impaired by the depletion (Fig. 4o). T cell viability was not affected by LD2 treatment (Extended Data Fig. 6p). To analyze the correlation between PRMT9 activity and T cell function, we analyzed the RNA-seq results from GSE12417GSE14468 and used a reported[43] cytotoxic T lymphocyte (CTL) score. Those scores were negatively correlated with *PRMT9* levels (Fig. 4p and Extended Data Fig. 6q).

Fig. 3 | PRMT9-mediated methylation promotes cancer cell growth. **a**, SILAC workflow. **b**, Alteration of sites carrying DMA (red) or MMA (green) on *PRMT9* KD. LC–MS/MS, liquid chromatography–tandem mass spectrometry. **c**, Cytoscape[77] visualization of proteins carrying PRMT9-regulated R-methyl peptides. **d**, Percentage of hits among all PRMT9-methylated proteins according to Gene Ontology categories. **e**, Polysome profiling of RNAs from control and *PRMT9* KD Molm13 cells. Shown is the representative trace of one of three biological replicates. **f**, AML ($n = 3$ patients) or normal PBSC CD34$^+$ ($n = 3$ healthy donors) cells with *PRMT9* KD, analyzed for protein synthesis using an OPP assay. Left: representative. Right: summarized results. Data are the mean ± s.d. **g**, Validation of representative proteins from the SILAC analysis of Molm13 cells ($n = 2$ independent experiments). **h**, *c-Myc* mRNA levels in RNAs extracted from the indicated fractions in ribosome profiling. **i**, Downregulated translation factors with a methylated R site after *PRMT9* KD. **j**, Schematic model of methylated arginine at the PABPC1 C terminus. **k**, In vitro methylation assay of GST-tagged PABPC1-CT mixed with PRMT9. Methylation was analyzed using immunoblotting as indicated ($n = 2$ independent experiments). **l**, Methylation assay of PABPC1 peptides mixed with PRMT9. Methylation was analyzed as indicated ($n = 3$ independent experiments). **m**, Molm13 cells were transduced with mock or PABPC1 (WT, R493K or 3RK) vectors resistant to PABPC1 shRNA; PABPC1 expression was assessed after endogenous *PABPC1* KD ($n = 2$ independent experiments). **n**, Protein synthesis. **o**, Cell viability ($n = 5$ independent experiments). Data are the mean ± s.d. The *P* value was determined using a one-way ANOVA. NS, not significant. **p**, Schematic model of the translation function of PABPC1. **q**, 293T cells were cotransfected with HA-tagged PABPC1 plus FLAG-tagged PABPC1 (WT or R493K). Cell lysates were then subjected to FLAG pull-down and detected using immunoblotting ($n = 1$). **r**, 293T cells were transfected with FLAG-tagged PABPC1 and subjected to poly(A) pulldown, then detected using immunoblotting ($n = 2$ independent experiments). **s**, 293T cells were cotransfected with Myc-tagged eRF3 and FLAG-tagged PABPC1 and subjected to FLAG pulldown, then detected as indicated ($n = 1$). **t**, Indicated amounts of unmodified, SDMA-R493 or ADMA-R493 PABPC1 peptides (amino acids G491–T507) were spotted for a dot blot assay. PABPC1 peptides were detected using anti-R493me-specific or control antibodies. **u**, R493 methylation. PRMT9 levels after *PRMT9* KD in Molm13 ($n = 2$ independent experiments) cells. **v**, PRMT9 and R493 methylation levels in CD34$^+$ subsets versus the blast (CD34$^-$CD33$^+$) subset from the cases with AML ($n = 7$ patients). *P* values were determined using a paired two-sided *t*-test. **w**, Pearson correlation of R493 methylation with PRMT9 levels in AML CD34$^+$. The *P* value was determined using simple linear regression analysis. The immunoblot analysis is shown in Extended Data Fig. 5c.

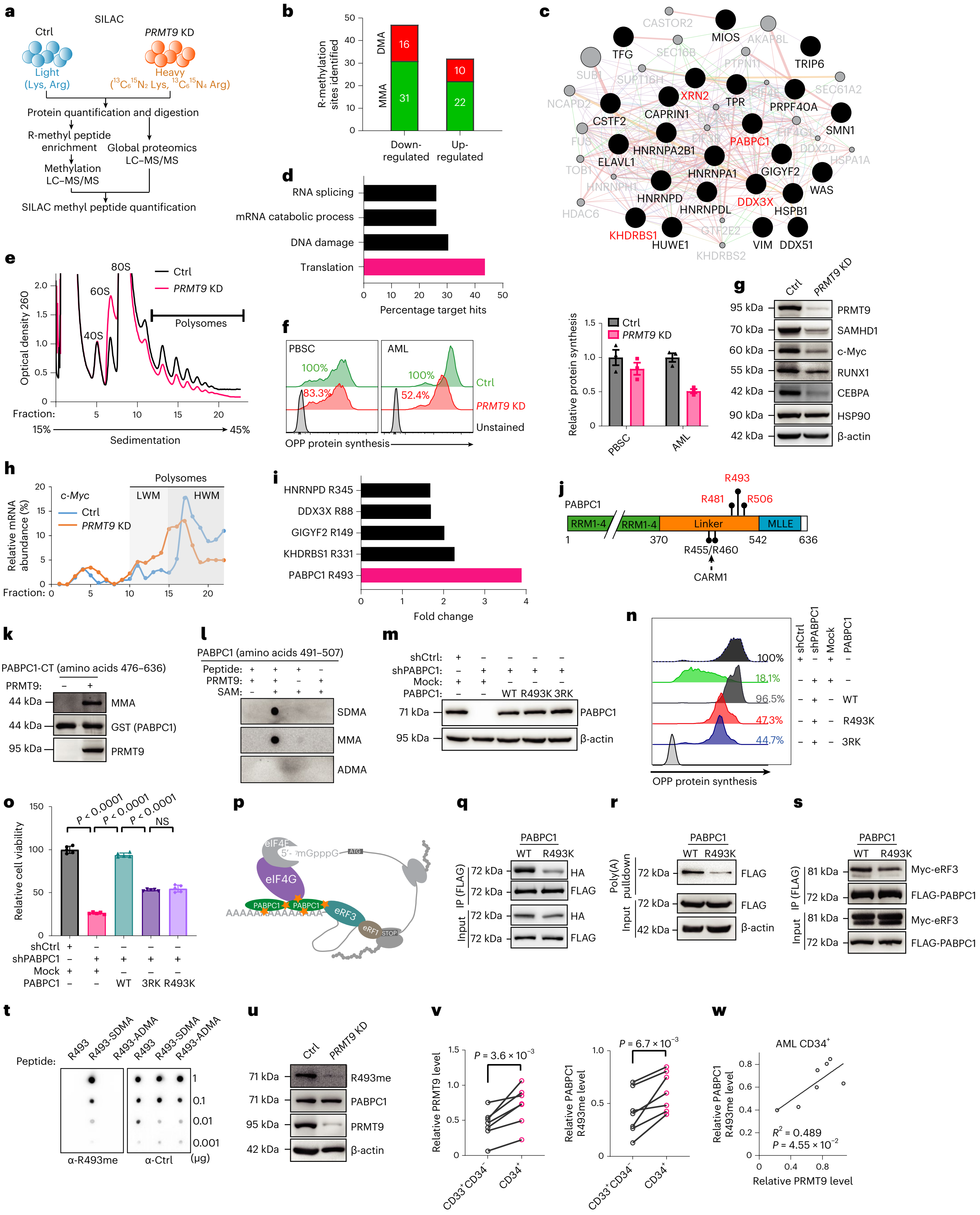
a
SILAC
Ctrl
PRMT9 KD
Light
(Lys, Arg)
Heavy
($^{13}C_6$ $^{15}N_2$ Lys, $^{13}C_6$ $^{15}N_4$ Arg)
Protein quantification and digestion
R-methyl peptide enrichment
Global proteomics LC–MS/MS
Methylation LC–MS/MS
SILAC methyl peptide quantification
b
R-methylation sites identified
DMA
MMA
16
31
10
22
Down-regulated
Up-regulated
c
CASTOR2
MIOS
AKAP8L
TFG
SEC16B
TRIP6
SUB1
SUPT16H
PTPN11
XRN2
TPR
EIF4E
SEC61A2
NCAPD2
CSTF2
CAPRIN1
EIF3A
PRPF40A
SMN1
FUS
PABPC1
EIF4G1
ELAVL1
HNRNPA2B1
DDX20
HSPA1A
TOB1
HNRNPA1
GIGYF2
HNRNPH1
HNRNPD
HNRNPDL
DDX3X
WAS
HDAC6
HSPB1
KHDRBS1
GTF2E2
HUWE1
VIM
DDX51
KHDRBS2
d
RNA splicing
mRNA catabolic process
DNA damage
Translation
Percentage target hits
e
Optical density 260
80S
60S
40S
Ctrl
PRMT9 KD
Polysomes
Fraction:
15%
45%
Sedimentation
f
PBSC
AML
100%
83.3%
52.4%
Ctrl
PRMT9 KD
Unstained
OPP protein synthesis
Relative protein synthesis
PBSC
AML
g
Ctrl
PRMT9 KD
95 kDa PRMT9
70 kDa SAMHD1
60 kDa c-Myc
55 kDa RUNX1
42 kDa CEBPA
90 kDa HSP90
42 kDa β-actin
h
Polysomes
c-Myc
LWM
HWM
Relative mRNA abundance (%)
Ctrl
PRMT9 KD
Fraction:
i
HNRNPD R345
DDX3X R88
GIGYF2 R149
KHDRBS1 R331
PABPC1 R493
Fold change
j
PABPC1
R493
R481
R506
RRM1-4
RRM1-4
Linker
MLLE
1
370
542
636
R455/R460
CARM1
k
PABPC1-CT (amino acids 476–636)
PRMT9:
44 kDa MMA
44 kDa GST (PABPC1)
95 kDa PRMT9
l
PABPC1 (amino acids 491–507)
Peptide:
PRMT9:
SAM:
SDMA
MMA
ADMA
m
shCtrl:
shPABPC1:
Mock:
PABPC1:
WT R493K 3RK
71 kDa PABPC1
95 kDa β-actin
n
shCtrl
shPABPC1
Mock
PABPC1
100%
18.1%
96.5%
47.3%
44.7%
WT
R493K
3RK
OPP protein synthesis
o
Relative cell viability
P < 0.0001
P < 0.0001
P < 0.0001
NS
shCtrl
shPABPC1
Mock
PABPC1
WT
3RK
R493K
p
eIF4E
5′- mGpppG
ATG
eIF4G
PABPC1
PABPC1
eRF3
eRF1
STOP
AAAAAAAAAAAAAAAA
q
PABPC1
WT R493K
IP (FLAG)
Input
72 kDa HA
72 kDa FLAG
r
PABPC1
WT R493K
Poly(A) pulldown
Input
72 kDa FLAG
42 kDa β-actin
s
PABPC1
WT R493K
IP (FLAG)
Input
81 kDa Myc-eRF3
72 kDa FLAG-PABPC1
t
Peptide:
R493
R493-SDMA
R493-ADMA
α-R493me
α-Ctrl
(μg)
u
Ctrl
PRMT9 KD
71 kDa R493me
71 kDa PABPC1
95 kDa PRMT9
42 kDa β-actin
v
$P = 3.6 \times 10^{-3}$
Relative PRMT9 level
$P = 6.7 \times 10^{-3}$
Relative PABPC1 R493me level
$CD33^+CD34^-$
$CD34^+$
w
AML $CD34^+$
Relative PABPC1 R493me level
$R^2 = 0.489$
$P = 4.55 \times 10^{-2}$
Relative PRMT9 level

PRMT9 inhibition eradicates AML in vivo

To assess whether cancer-intrinsic PRMT9 inhibition induces immune responses, we used an MA9 AML transplant model (Fig. 5a,d). These MA9 AML cells were transduced with either a DOX-inducible shPrmt9 or shCtrl construct. Congenic WT *C57BL/6* (B6) mice were used as recipients; *Rag2*$^{-/-}$ (Fig. 5b) or *NSG-SGM3* (*NSGS*) (Fig. 5c) mice were also used. After engraftment, DOX was administered. *Rag2*$^{-/-}$ (Fig. 5b,e) or *NSGS* (Fig. 5c,f) mice bearing *Prmt9* KD transplants survived significantly longer than mice with *Prmt9* WT transplants, but succumbed to leukemia within 60 days (Fig. 5e,f). In contrast, five of seven B6 mice receiving *Prmt9* KD transplants survived until day 120 (Fig. 5d). We established another cohort of MA9 leukemia transplants using B6 recipients and induced *Prmt9* deletion on day 30. As shown (Extended Data Fig. 7a,b), *Prmt9* KD modestly decreased AML progression.

We also performed antibody-based depletion of T or natural killer (NK) cells before in vivo DOX administration to KD *Prmt9* (Extended Data Fig. 7c,d). CD4 and CD8 T cell depletion significantly abolished *Prmt9* KD-induced AML regression, while NK depletion had minor effects (Extended Data Fig. 7c,d).

To verify the role of *Prmt9* inhibition in a different AML model, we used the CMM transplant model[25]. Thus, *Prmt9* KD-mediated leukemia elimination effects are comparable in both models (Fig. 5g). Notably, *Prmt9* KD remarkably decreased leukemia-initiating cell frequency in both models (Fig. 5d,g and Supplementary Table 7).

We performed scRNA-seq analysis of the MA9 tumor microenvironment. A cohort of WT B6 mice transplanted with DOX-inducible *Prmt9* KD AML cells was established; we evaluated the transcriptional status of all immune lineages in transplants 7 days after DOX treatment. At that time, mice receiving *Prmt9* KD cells began to exhibit decreased AML engraftment (Extended Data Fig. 7e). We then collected bone marrow and spleen cells from a representative mouse in each group for scRNA-seq. Our transcriptomes include 9,741 control and 11,291 *Prmt9* KD bone marrow cells. We visualized transcriptionally homogeneous cell clusters (Fig. 5h,i and Supplementary Fig. 7). Notably, *Prmt9* levels were more abundant in leukemic cells than other cells; *Prmt9* KD decreased tumor cell frequency relative to controls (Fig. 5j and Extended Data Fig. 7f,g) and induced T cell activation (Fig. 5k). To verify T cell function, we assessed leukemia-specific T cell responses after *Prmt9* KD using major histocompatibility complex (MHC)-survivin peptide as described in Stroopinsky et al.[44]. We confirmed the elevated expression of Birc5 (encoding survivin) in cancer relative to the other subsets (Supplementary Fig. 8). We also noted that *Prmt9* KD mice exhibited increased CD8^{+} T cells recognizing tumor survivin relative to *Prmt9* WT controls (Fig. 5l). The results were confirmed using MA9/OVA cells (Fig. 5m).

We analyzed the scRNA-seq results of spleen, where T cells are more abundant (Extended Data Fig. 7h–k). We focused on T cells (Fig. 5n,o and Extended Data Fig. 7l). Accordingly, ten distinct T cell subpopulations (c0–9) were characterized, including c0 (naive CD4^{+}), c1 (naive CD8^{+}), c2 (memory CD8^{+}cells), c3 (effector CD4^{+}cells), c8 (memory T cells), c4 and c9 (effector T (T_{eff}) cells), c5 (CTLs) and c6 (regulatory (T_{reg}) cells) (Fig. 5n,o). Notably, *Prmt9* KD altered the proportions of the subpopulations (Fig. 5o–r). *Prmt9* KD reduced the naive T cell subsets (c0, c1) and expanded the populations of effector and memory T cells (c2, c3, c4, c8 and c9) (Fig. 5q,r). *Prmt9* KD also increased CTLs (c5) and decreased T_{reg} cells (c6) (Fig. 5q,r). In bone marrow, *Prmt9* KD expanded *Cd44*-expressing T cells and decreased *Foxp3*-expressing T_{reg} cells (Extended Data Fig. 7m,n).

To assess immune memory, we selected primary B6 mice that had shown complete regression of MA9 tumors on *Prmt9* KD. We rechallenged them and the naive control cohort by injecting them with comparable numbers of MA9 cells. Unlike the control cohort (Fig. 5s), tumor-free mice exhibited a survival benefit after being rechallenged (Extended Data Fig. 7o).

Prmt9 KD upregulated IFN-stimulated gene (ISG) levels in T cells (Fig. 5t). Gene set enrichment analysis (GSEA) highlighted the activation of the IFN response pathways in T cells (Fig. 5u and Extended Data Fig. 7p). Similarly, ISG upregulation, including *Isg15* (Extended Data Fig. 7q,r), *Ifit1* (Extended Data Fig. 7s,t) and *Cxcl10* (Extended Data Fig. 7u), was seen in other immune cell types. To verify that type I IFN responses underlined the outcomes, *Prmt9* KD MA9 cells were transplanted into WT recipient or type I IFN receptor KO (*Ifnar1* KO) mice. After leukemia cell engraftment, we induced *Prmt9* KD and monitored leukemia development. The anti-AML effects of *Prmt9* KD were significantly abolished on an *Ifnar1* KO background (Fig. 5v).

Immunity after PRMT9 inhibition requires cGAS activity

By analyzing the scRNA-seq transcriptomes of MA9 cells, we observed upregulation of multiple ISGs after *Prmt9* KD (Fig. 6a and Extended Data Fig. 8a). GSEA showed top enrichment of the IFN-α and IFN-γ pathways after *Prmt9* KD (Fig. 6b and Extended Data Fig. 8b). Consistently, transcriptome profiling of the AML lines confirmed innate immune signaling activation by targeting Prmt9 (Fig. 6c and Extended Data Fig. 8c,d). To determine if innate immune activation was associated with PRMT9 activity, we compared ISG expression in Molm13 cells overexpressed WT or catalytic mutant PRMT9 after KD of endogenous *PRMT9*. Notably, only expression of PRMT9 WT, but not the mutant rescued ISG upregulation (for example, *ISG15*, *IFI44*) (Fig. 6d and Extended Data Fig. 8e). LD2 treatment also stimulated ISGs expression (Fig. 6e and Extended Data Fig. 8f,g).

We used THP1-*Lucia* luciferase to monitor IFN regulatory factor (IRF) signaling downstream of innate immune sensors, including the double-stranded DNA (dsDNA) sensor cGAS or dsRNA sensors. *PRMT9* KD or LD2 treatment of THP1-*Lucia* luciferase increased luciferase signals (Fig. 6f and Extended Data Fig. 8h); an increase was blocked

Fig. 4 | Identification of a PRMT9 inhibitor. **a**, Screening pipeline. HT, high throughput. **b**, Docking pose of the top 30 hits. **c**, Effects of the top 20 compounds on Molm13 viability. **d**, Screening of nine compounds using the R493 methylation assay. Catalytic activity was assessed using a dot blot assay with an anti-R493-specific antibody. No. 1: LD2. **e**, Three-dimensional docking model. Left: LD2 in the pocket. Right: LD2 binding sites. **f**, CPMG NMR for 40 µM LD2 (blue); LD2 in the presence of PRMT9. **g**, STD NMR. (i) Reference (blue) and saturated (red) spectra. (ii) STD spectrum showing the difference between reference and saturated spectra. Asterisk denotes impurity. **h**,**i**, Thermal shift assay (**h**) and relative PRMT9 protein (**i**) of WT mutant PRMT9 from Molm13 cells treated with 2.5 µM LD2. The catalysis inhibition curves are based on the gray intensity of blots normalized to intensity at 37 °C ($n = 3$ independent experiments). A comparison was made between LD2-treated PRMT9 WT versus LD2-treated PRMT9 mutant. **i**, Data ($n = 3$ independent replicates) are represented as the mean ± s.d. *P* values were determined using a two-way ANOVA. **j**, Half-maximal inhibitory concentration (IC_{50}) of LD2 in the indicated cells. Cells were treated for 4 days with LD2. MV4-11 ($n = 6$), NB4 ($n = 3$), U937 ($n = 3$), PBSC CD34^{+} ($n = 6$), MA9.6ITD ($n = 3$), Molm13 ($n = 3$) and THP1 ($n = 4$); data are the mean ± s.d. *n* indicates independent experiments and represents the number of independent experiments. **k**, Protein synthesis in the indicated cells after treatment with 2.5 µM LD2, based on an OPP assay. Right: results in vehicle versus LD2 ($n = 3$ independent experiments). Data are presented as the mean ± s.d. **l**, R493 methylation of Molm13 cells treated as indicated ($n = 3$ independent experiments). **m**, CyTOF of AML MNCs after 4 days of treatment with LD2 (2.5 µM). The frequency of T cells and CD34^{+}CD45^{dim} AML blast cells was noted. Color bar: CD34 intensity. **n**, Flow plots showing T cell and AML populations in the AML01, before and after T cell depletion. **o**, T cell depleted or bulk MNCs ($n = 3$ patients) were treated with LD2 (2.5 µM). AML blasts were determined using flow cytometry. Data are the mean ± s.d. from three independent experiments. **p**, Frequency of PRMT9^{hi} ($n = 43$) versus low ($n = 67$) AML samples displaying the CTL score high versus low signatures in GSE12417. The *P* value was determined using a two-sided Fisher exact test. *n* represents the number of patients.

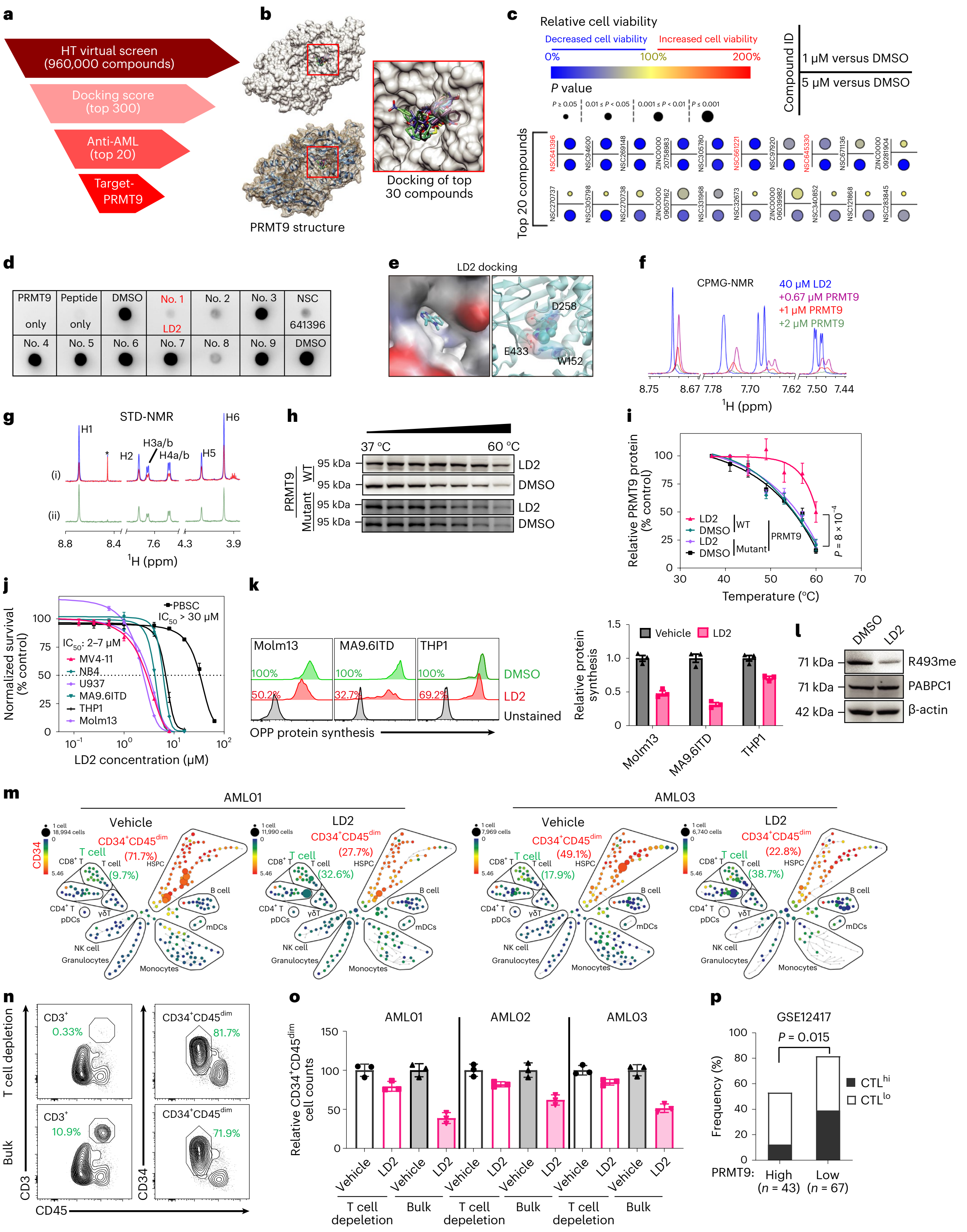
a
HT virtual screen (960,000 compounds)
Docking score (top 300)
Anti-AML (top 20)
Target-PRMT9
b
PRMT9 structure
Docking of top 30 compounds
c
Relative cell viability
Decreased cell viability
Increased cell viability
0%
100%
200%
P value
P ≥ 0.05
0.01 ≤ P < 0.05
0.001 ≤ P < 0.01
P ≤ 0.001
Compound ID
1 μM versus DMSO
5 μM versus DMSO
Top 20 compounds
NSC641396
NSC94600
NSC269148
ZINC0000 20758983
NSC305780
NSC661221
NSC97920
NSC645330
NSC671136
ZINC0000 09281904
NSC270737
NSC305798
NSC270738
ZINC0000 09057162
NSC331968
NSC32673
ZINC0000 06039982
NSC340852
NSC121868
NSC283845
d
PRMT9 only
Peptide only
DMSO
No. 1 LD2
No. 2
No. 3
NSC 641396
No. 4
No. 5
No. 6
No. 7
No. 8
No. 9
DMSO
e
LD2 docking
D258
E433
W152
f
CPMG-NMR
40 μM LD2
+0.67 μM PRMT9
+1 μM PRMT9
+2 μM PRMT9
8.75
8.67
7.78
7.70
7.62
7.50
7.44
¹H (ppm)
g
STD-NMR
H1
*
H2
H3a/b
H4a/b
H5
H6
(i)
(ii)
8.8
8.4
7.6
4.3
3.9
¹H (ppm)
h
37 °C
60 °C
PRMT9
WT
Mutant
95 kDa
LD2
DMSO
LD2
DMSO
i
Relative PRMT9 protein (% control)
LD2
DMSO
WT
LD2
DMSO
Mutant
PRMT9
P = 8 × 10⁻⁴
Temperature (°C)
30
40
50
60
70
0
25
50
75
100
j
Normalized survival (% control)
PBSC
IC50 > 30 μM
IC50: 2–7 μM
MV4-11
NB4
U937
MA9.6ITD
THP1
Molm13
LD2 concentration (μM)
10⁻¹
10⁰
10¹
10²
k
Molm13
MA9.6ITD
THP1
100%
100%
100%
50.2%
32.7%
69.2%
DMSO
LD2
Unstained
OPP protein synthesis
Relative protein synthesis
Vehicle
LD2
Molm13
MA9.6ITD
THP1
0
0.5
1.0
1.5
l
DMSO
LD2
71 kDa
R493me
71 kDa
PABPC1
42 kDa
β-actin
m
AML01
AML03
Vehicle
LD2
Vehicle
LD2
1 cell
18,994 cells
11,990 cells
7,969 cells
6,740 cells
CD34
5.46
0
CD34⁺CD45dim
(71.7%)
(27.7%)
(49.1%)
(22.8%)
T cell
(9.7%)
(32.6%)
(17.9%)
(38.7%)
CD8⁺ T
T cell
HSPC
B cell
CD4⁺ T
γδT
pDCs
mDCs
NK cell
Granulocytes
Monocytes
n
T cell depletion
Bulk
CD3⁺
0.33%
10.9%
CD34⁺CD45dim
81.7%
71.9%
CD3
CD34
CD45
o
Relative CD34⁺CD45dim cell counts
AML01
AML02
AML03
Vehicle
LD2
Vehicle
LD2
T cell depeletion
Bulk
0
50
100
150
p
GSE12417
P = 0.015
Frequency (%)
CTLhi
CTLlo
PRMT9:
High (n = 43)
Low (n = 67)
0
20
40
60
80
100

by deletion of cGAS. *PRMT9* KD also enhanced cGAS activity, as evidenced by increased cGAMP (Fig. 6g). Overexpression of ENPP1, which degrades cGAMP, abrogated this effect (Fig. 6g and Extended Data Fig. 8i). *PRMT9* KD increased γH2AX levels, which is indicative of DNA damage (Fig. 6h and Extended Data Fig. 8j,l), and promoted the accumulation of cytoplasmic dsDNA (Fig. 6i and Extended Data Fig. 8k,m). To determine whether tumor-intrinsic cGAS activity was required for *Prmt9* KD-mediated immunity, MA9-OVA cells with *cGAS* KO (Extended Data Fig. 8n) were transduced with either inducible shPrmt9 or shCtrl and implanted into WT recipients. Unlike controls, *cGAS* KO mice did not show the tumor-specific T cell response seen after *Prmt9* KD (Fig. 5m). Survival advantages were abolished on a *cGAS* KO background (Fig. 6j). To test the outcomes of cGAS activation in cancer cells, we transduced *cGAS* KO MA9 cells with an inducible cGAS-activating mutant (ΔN)[45] or corresponding *cGAS* WT (Fig. 6k) and then implanted parental (*cGAS* KO), *cGAS* WT or ΔN-expressing cells into B6 mice to analyze leukemogenesis. A reduced AML burden was seen in ΔN transplants (Fig. 6l). Mice with AML cells exhibiting cGAS activation showed significantly extended survival relative to other groups (Fig. 6m). cGAS levels were remarkably high in AML relative to normal donors (Fig. 6n), while ENPP1 levels were relatively lower in AML (Extended Data Fig. 8o). Moreover, among deadly cancers, AML cells exhibited the highest cGAS and lowest ENPP1 levels (Extended Data Fig. 8p,q).

We hypothesized that the T cell priming effects seen after *Prmt9* KD could be mediated by increases in the immune transmitter cGAMP. Indeed, we observed elevated cGAMP levels in bone marrow fluid from *Prmt9* KD MA9 mice (Fig. 6o). Moreover, the single-cell transcriptomes of DCs and macrophages revealed increased levels of *Cd86* and MHC class II (*H2-ab1*), suggesting activation (Fig. 6p and Extended Data Fig. 8r). To determine whether the T cell priming effects seen after Prmt9 inhibition were due to antigen cross-presentation by DCs, we cocultured LD2-pretreated *cGAS* KO or *cGAS* WT MA9/OVA cells with bone marrow-derived DCs and then purified the DCs, which were exposed to naive OT-I$^+$CD8$^+$ T cells. We observed increased IFN-γ production by CD8$^+$ T cells after coculture with DCs purified from the LD2-pretreated AML group (Fig. 6q). *cGAS* KO antagonized the DC-mediated cross-priming capacity, based on decreased IFN-γ production (Fig. 6q). We then assessed IFN-β production by DCs after coculture with MA9-OVA cells pretreated with LD2 and observed increased IFN-β production (Fig. 6r), an effect abolished by *cGAS* KO, suggesting that tumor *cGAS* activation underlies type I IFN signaling in DCs. We further assessed DC function in *Prmt9* KD-induced AML regression using *Batf3* KO mice because Batf3 is critical to cross-prime T cells[46]. Specifically, we implanted *Batf3* WT or KO mice with AML cells for assessment of AML progression. Relative to *Batf3* WT mice, *Batf3* KO partially decreased the *Prmt9* KD-induced survival advantage (Fig. 6s).

Loss of XRN2 methylation underlies *cGAS* activation

PRMT9 inhibition in THP1 cells via LD2 (48 h) or shRNA significantly increased Rad3-related (ATR) signaling, whereas γH2AX elevation and changes in ataxia-telangiectasia-mutated (ATM) signaling were modest (Fig. 7a,b). However, we observed remarkably increased levels of γH2AX and pCHK2 after 72 h of PRMT9 inhibition (Figs. 6h and 7a,b), corresponding with the formation of DNA double strand breaks (Fig. 7c). These findings suggest that PRMT9 inhibition triggers an early insult that selectively activates ATR.

We next asked whether any PRMT9 substrate functions in the DNA damage response and whether its loss underlies ATR activation and cGAS stimulation. SILAC showed that seven of the 23 most downregulated methylated proteins after *PRMT9* KD (Fig. 3c) regulate the DNA damage response (Fig. 3d and Extended Data Fig. 8s). To determine whether KO of any of them phenocopied the PRMT9 inhibition effects, we electroporated THP1-*Lucia* luciferase cells with Cas9 protein and bound guide RNA (gRNA) targeting the respective candidate genes[47]. Of the seven genes, KO of *XRN2*, *DDX3X* or *KHDRBS1* increased reporter activity (Fig. 7d,f); an in vitro methylation assay confirmed PRMT9 catalysis (Fig. 7e). We then ectopically expressed gRNA-resistant full-length XRN2 WT or DDX3X WT complementary DNAs or corresponding methylation-deficient constructs (*XRN2*-R946K or *DDX3X*-R88K) in THP1-*Lucia* luciferase cells and the corresponding *cGAS* KO/THP1-*Lucia* luciferase line, then KO the corresponding endogenous genes. Notably, *XRN2*-R946K expression increased THP1 reporter activity, an effect blocked by *cGAS* deletion (Fig. 7g), while methylation-deficient DDX3X did not increase reporter activity (Fig. 7h). We confirmed that *XRN2*-R946K is methylated by PRMT9, based on in vitro methylation and responses to LD2 treatment (Fig. 7i,j).

We next focused on the exoribonuclease XRN2 whose C terminus interacts with p54nrb to prevent R-loop formation[48]. SILAC analysis revealed that among all XRN2 R residues, only R946 methylation levels were altered by *PRMT9* KD (Supplementary Table 8). To determine if R946 methylation promotes XRN2 recruitment by p54nrb, we performed co-IP analysis. FLAG-tagged XRN2 interaction with p54nrb was decreased in the presence of R946K (Fig. 7k and Extended Data Fig. 8t). Relative to *XRN2* WT, expression of the gRNA-resistant *XRN2*-R946K mutant in THP1 cells engineered to lack endogenous XRN2 promoted R-loop formation (Fig. 7l,m), resulting in ATR activation and γH2AX elevation (Fig. 7k). Consistently, LD2 treatment or *PRMT9* KD promoted excess R-loop formation and activated ATR signaling as early as 48 h after treatment (Fig. 7a,b,n,o). Cell cycle analysis after LD2 treatment showed an increased percentage of G_2/M (Fig. 7p). Finally, *RNASEH1* overexpression to resolve R-loops (Fig. 7n) decreased ATR/CHK1 activation, partially rescuing the THP1-luciferase reporter activity induced by LD2 (Fig. 7q,r). Collectively, these results indicate that loss of XRN2 methylation contributes to DNA damage by PRMT9 inhibition.

Fig. 5 | PRMT9 inhibition eradicates AML in vivo. **a**–**c**, MA9-luciferase cells were injected into B6 (**a**, $n = 7$ mice per group), *Rag2*$^{-/-}$ (**b**, $n = 5$ mice per group) and *NSGS* (**c**, $n = 5$ mice per group) mice. After engraftment, mice were administered DOX water. Engraftment was tracked using imaging; color bars, luminescence radiance (photons $s^{-1} cm^{-2} sr^{-1}$). **d**–**f**, Kaplan–Meier curves showing the survival of B6 (**d**), *Rag2*$^{-/-}$ (**e**) and *NSGS* (**f**) mice. *P* values were determined using a log-rank (Mantel–Cox) test. **g**, CMM cells were injected into B6 mice ($n = 7$ mice per group). *Prmt9* KD was induced as above. The Kaplan–Meier curves show the survival of mice. *P* values were determined using a log-rank (Mantel–Cox) test. **h**,**i**, Different populations (**h**) or markers (**i**) identified in bone marrow. **j**, *Prmt9* level in the bone marrow populations. **k**, *Cd69*, *Ifng* and *Gzmb* levels in T cells of Ctrl ($n = 249$ cells) and *Prmt9* KD ($n = 231$ cells) bone marrow. Right: *Ifng* levels. Data are presented as the mean ± s.e.m. The *P* value was determined using an unpaired two-sided *t*-test. **l**, Frequency of AML-specific CD8$^+$ T cells in *Prmt9* KD mice ($n = 5$ mice) relative to *Prmt9* WT controls ($n = 5$ mice). Data are the mean ± s.e.m. The *P* value was determined using an unpaired two-sided *t*-test. **m**, Indicated MA9/OVA cells were implanted into B6 mice ($n = 5$ mice per group). After engraftment, *Prmt9* KD was induced. MA9-OVA-specific T cells were assessed. Data are the mean ± s.e.m. The *P* value was determined using a one-way ANOVA test. **n**, Subpopulations identified among T cells from the spleen in the merged Ctrl and *Prmt9* KD groups. **o**, Expression levels of the indicated genes in the T cell clusters. **p**, Distribution of the clusters annotated in **n**. **q**,**r**, Percentage of clusters in CD8$^+$ (**q**) or CD4$^+$ (**r**) T cells annotated in **n**. **s**, Survivors of *Prmt9* KDMA9 cell-challenged mice ($n = 4$) were rechallenged with 1×10^6 parental MA9 *Prmt9* KD cells (without DOX induction). Control naive C57BL/6 mice ($n = 5$ mice per group) inoculated with the same number of cells. The Kaplan–Meier curves show the survival of mice. The *P* value was determined using a log-rank (Mantel–Cox) test. **t**, Upregulated ISGs in T cells. **u**, GSEA of DEGs in bone marrow T cells after *Prmt9* KD. **v**, MA9-luciferase cells were injected into WT ($n = 7$ mice) or *Ifnar1* KO mice ($n = 5$ mice). *Prmt9* KD was induced as above. The Kaplan–Meier curves show the survival of mice. The *P* value was determined using a log-rank (Mantel–Cox) test.

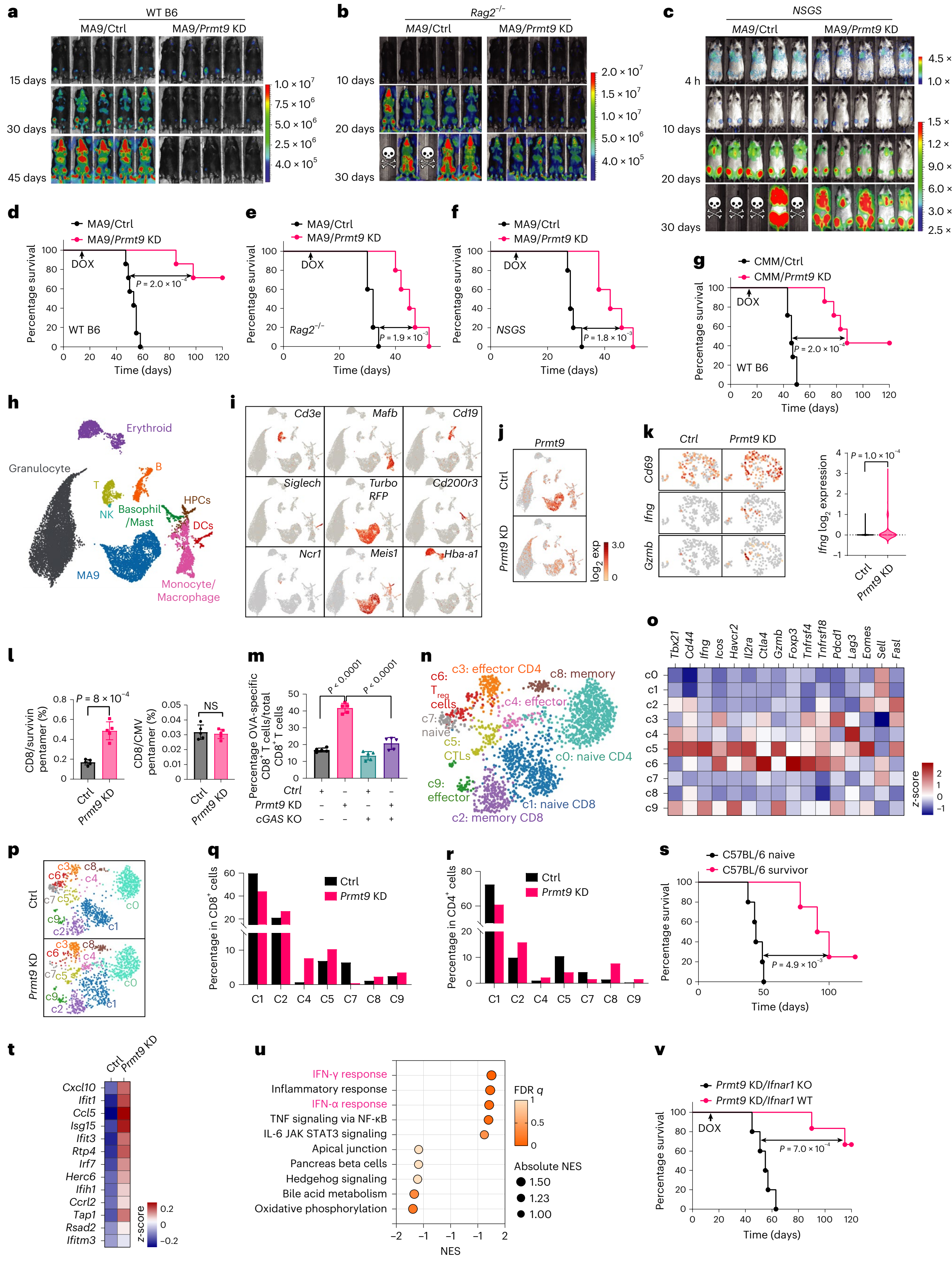
a
WT B6
MA9/Ctrl
MA9/Prmt9 KD
15 days
30 days
45 days
1.0 × 10^7
7.5 × 10^6
5.0 × 10^6
2.5 × 10^6
4.0 × 10^5
b
Rag2^-/-
MA9/Ctrl
MA9/Prmt9 KD
10 days
20 days
30 days
2.0 × 10^7
1.5 × 10^7
1.0 × 10^7
5.0 × 10^6
4.0 × 10^5
c
NSGS
MA9/Ctrl
MA9/Prmt9 KD
4 h
10 days
20 days
30 days
4.5 × 10^5
1.0 × 10^5
1.5 × 10^7
1.2 × 10^7
9.0 × 10^6
6.0 × 10^6
3.0 × 10^6
2.5 × 10^5
d
MA9/Ctrl
MA9/Prmt9 KD
Percentage survival
DOX
P = 2.0 × 10^-3
WT B6
Time (days)
e
MA9/Ctrl
MA9/Prmt9 KD
DOX
Rag2^-/-
P = 1.9 × 10^-3
f
MA9/Ctrl
MA9/Prmt9 KD
DOX
NSGS
P = 1.8 × 10^-3
g
CMM/Ctrl
CMM/Prmt9 KD
DOX
P = 2.0 × 10^-4
WT B6
h
Erythroid
Granulocyte
B
T
NK
Basophil/Mast
HPCs
DCs
MA9
Monocyte/Macrophage
i
Cd3e
Mafb
Cd19
Siglech
Turbo RFP
Cd200r3
Ncr1
Meis1
Hba-a1
j
Prmt9
Ctrl
Prmt9 KD
log2 exp
3.0
0
k
Ctrl
Prmt9 KD
Cd69
Ifng
Gzmb
P = 1.0 × 10^-4
Ifng log2 expression
Ctrl
Prmt9 KD
l
P = 8 × 10^-4
CD8/survivin pentamer (%)
Ctrl
Prmt9 KD
NS
CD8/CMV pentamer (%)
m
P < 0.0001
P < 0.0001
Percentage OVA-specific CD8+ T cells/total CD8+ T cells
Ctrl + − + −
Prmt9 KD − + − +
cGAS KO − − + +
n
c3: effector CD4
c8: memory
c6: Treg cells
c4: effector
c7: naive
c5: CTLs
c0: naive CD4
c9: effector
c1: naive CD8
c2: memory CD8
o
Tbx21
Cd44
Ifng
Icos
Havcr2
Il2ra
Ctla4
Gzmb
Foxp3
Tnfrsf4
Tnfrsf18
Pdcd1
Lag3
Eomes
Sell
Fasl
c0
c1
c2
c3
c4
c5
c6
c7
c8
c9
z-score
2
1
0
−1
p
Ctrl
Prmt9 KD
q
Percentage in CD8+ cells
Ctrl
Prmt9 KD
C1
C2
C4
C5
C7
C8
C9
r
Percentage in CD4+ cells
Ctrl
Prmt9 KD
s
C57BL/6 naive
C57BL/6 survivor
Percentage survival
P = 4.9 × 10^-3
Time (days)
t
Ctrl
Prmt9 KD
Cxcl10
Ifit1
Ccl5
Isg15
Ifit3
Rtp4
Irf7
Herc6
Ifih1
Ccrl2
Tap1
Rsad2
Ifitm3
z-score
0.2
0
−0.2
u
IFN-γ response
Inflammatory response
IFN-α response
TNF signaling via NF-κB
IL-6 JAK STAT3 signaling
Apical junction
Pancreas beta cells
Hedgehog signaling
Bile acid metabolism
Oxidative phosphorylation
FDR q
1
0.5
0
Absolute NES
1.50
1.23
1.00
NES
v
Prmt9 KD/Ifnar1 KO
Prmt9 KD/Ifnar1 WT
DOX
P = 7.0 × 10^-4
Percentage survival
Time (days)

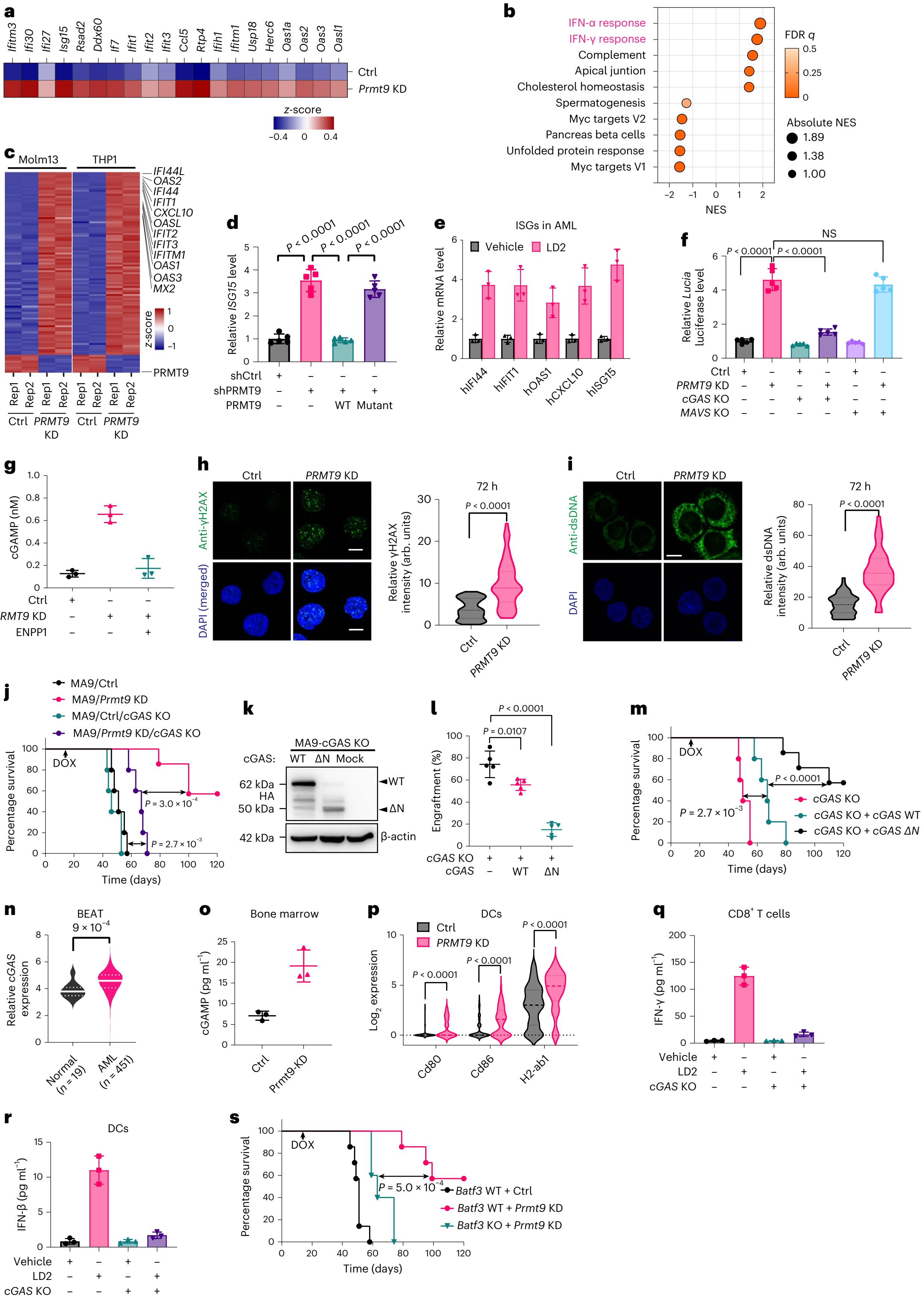
a
Ifitm3 Ifi30 Ifi27 Isg15 Rsad2 Ddx60 If7 Ifit1 Ifit2 Ifit3 Ccl5 Rtp4 Ifih1 Ifitm1 Usp18 Herc6 Oas1a Oas2 Oas3 Oasl1
Ctrl
Prmt9 KD
z-score
−0.4 0 0.4
b
IFN-α response
IFN-γ response
Complement
Apical juntion
Cholesterol homeostasis
Spermatogenesis
Myc targets V2
Pancreas beta cells
Unfolded protein response
Myc targets V1
NES
−2 −1 0 1 2
FDR q
0.5 0.25 0
Absolute NES
1.89 1.38 1.00
c
Molm13 THP1
IFI44L OAS2 IFI44 IFIT1 CXCL10 OASL IFIT2 IFIT3 IFITM1 OAS1 OAS3 MX2
PRMT9
z-score 1 0 −1
Rep1 Rep2 Rep1 Rep2 Rep1 Rep2 Rep1 Rep2
Ctrl PRMT9 KD Ctrl PRMT9 KD
d
Relative ISG15 level
P < 0.0001 P < 0.0001 P < 0.0001
shCtrl + – – –
shPRMT9 – + + +
PRMT9 – – WT Mutant
e
ISGs in AML
Vehicle LD2
Relative mRNA level
hIFI44 hIFIT1 hOAS1 hCXCL10 hISG15
f
Relative Lucia luciferase level
P < 0.0001 P < 0.0001 NS
Ctrl + – + – + –
PRMT9 KO – + – + – +
cGAS KO – – + + – –
MAVS KO – – – – + +
g
cGAMP (nM)
Ctrl + – –
PRMT9 KD – + +
ENPP1 – – +
h
Ctrl PRMT9 KD
Anti-γH2AX
DAPI (merged)
72 h
P < 0.0001
Relative γH2AX intensity (arb. units)
Ctrl PRMT9 KD
i
Ctrl PRMT9 KD
Anti-dsDNA
DAPI
72 h
P < 0.0001
Relative dsDNA intensity (arb. units)
Ctrl PRMT9 KD
j
MA9/Ctrl
MA9/Prmt9 KD
MA9/Ctrl/cGAS KO
MA9/Prmt9 KD/cGAS KO
Percentage survival
DOX
P = 3.0 × 10^−4
P = 2.7 × 10^−3
Time (days)
k
MA9-cGAS KO
cGAS: WT ΔN Mock
62 kDa
HA
50 kDa
42 kDa
WT
ΔN
β-actin
l
Engraftment (%)
P < 0.0001
P = 0.0107
cGAS KO + + +
cGAS – WT ΔN
m
Percentage survival
DOX
P < 0.0001
P = 2.7 × 10^−3
cGAS KO
cGAS KO + cGAS WT
cGAS KO + cGAS ΔN
Time (days)
n
BEAT
9 × 10^−4
Relative cGAS expression
Normal (n = 19)
AML (n = 451)
o
Bone marrow
cGAMP (pg ml^−1)
Ctrl Prmt9-KD
p
DCs
Ctrl
PRMT9 KD
Log2 expression
P < 0.0001 P < 0.0001 P < 0.0001
Cd80 Cd86 H2-ab1
q
CD8+ T cells
IFN-γ (pg ml^−1)
Vehicle + – + –
LD2 – + – +
cGAS KO – – + +
r
DCs
IFN-β (pg ml^−1)
Vehicle + – + –
LD2 – + – +
cGAS KO – – + +
s
Percentage survival
DOX
P = 5.0 × 10^−4
Batf3 WT + Ctrl
Batf3 WT + Prmt9 KD
Batf3 KO + Prmt9 KD
Time (days)

Fig. 6 | Immunity after PRMT9 inhibition requires cGAS activity. **a**, Upregulated ISGs in MA9 cells. **b**, GSEA of DEGs in *Prmt9* KD MA9 cells. **c**, Overlapped DEGs in the indicated cells (fold change > 2). NES, normalized enrichment score. **d**, *ISG15* expression in Molm13 cells with endogenous *PRMT9* KD and after rescuing with PRMT9 WT or a catalytically dead mutant ($n = 5$ independent experiments). Data are the mean ± s.d. The *P* value was determined using a one-way ANOVA. **e**, ISG levels in AML CD34$^+$ cells. Data are the mean ± s.d. from three independent experiments. **f**, Luciferase activity of THP1-IRF cells engineered as indicated ($n = 5$ independent experiments). Data are the mean ± s.d. The *P* value was determined using a one-way ANOVA. **g**, cGAMP levels in engineered THP1 supernatant ($n = 3$ independent experiments). Data are the mean ± s.d. **h**, Left: immunostaining for γH2AX in THP1 cells. Right: γH2AX intensity ($n = 100$ cells per group). Scale bars, 10 µm. The *P* value was determined using an unpaired two-sided *t*-test. **i**, dsDNA using immunostaining in THP1 cells. Right: dsDNA intensity ($n = 50$ cells per group). Scale bar, 10 µm. The *P* value was determined using an unpaired two-sided *t*-test. **j**, MA9/OVA cells (Ctrl, $n = 5$ mice), *Prmt9* KD ($n = 7$ mice), Ctrl + *cGAS* KO ($n = 5$ mice) and *Prmt9* KD + cGAS WT ($n = 5$ mice)) were transplanted to establish AML. *Prmt9* KD was induced. The Kaplan–Meier curves show the survival. *P* values were determined using a log-rank (Mantel–Cox) test. **k**, *cGAS* KO *MA9* cells were transduced with inducible HA-tagged cGAS WT or ΔN. Exogenous cGAS was then assessed ($n = 1$). **l**,**m**, *cGAS* KO ($n = 5$ mice), *cGAS* WT ($n = 5$ mice) or *cGAS*-ΔN MA9 ($n = 7$ mice) cells were transplanted. DOX was given to induce expression of cGAS variants. **l**, AML engraftment was assessed. Data are the mean ± s.e.m. *P* values were determined using a one-way ANOVA. **m**, For another cohort, Kaplan–Meier curves show survival. *P* values were determined using a log-rank (Mantel–Cox) test. **n**, *cGAS* levels in BEAT AML cases ($n = 451$ patients) and healthy donors ($n = 19$). The *P* value was determined using an unpaired two-sided *t*-test. **o**, cGAMP levels in the bone marrow of mice ($n = 3$ mice per group). Data are the mean ± s.d. **p**, Expression of *Cd80*, *Cd86* and *H2-ab1* in the DCs of the scRNA-seq of Ctrl ($n = 108$ cells) and *Prmt9* KD ($n = 57$ cells) bone marrow. *P* values were determined using an unpaired two-sided *t*-test. **q**,**r**, LD2-pretreated MA9/OVA cells were cocultured with bone marrow-derived DCs. DCs were then cocultured with OT-I transgenic CD8$^+$ T cells. **q**, IFN-γ production by CD8$^+$ T cells. **r**, IFN-β production by DCs. $n = 3$ independent experiments. Data are the mean ± s.d. **s**, MA9 AML cells were implanted into *Batf3* WT or KO mice: (1) *Prmt9* KD/*Batf3* KO ($n = 5$ mice), (2) *Prmt9* KD/*Batf3* WT ($n = 7$ mice) and (3) *Prmt9* WT/*Batf3* WT ($n = 7$ mice). Kaplan–Meier curves show survival. *P* values were determined using a log-rank (Mantel–Cox) test.

Combining LD2 with an ICI ablates cancers

Based on the scRNA-seq results, among the reported relevant immune checkpoint proteins, *Prmt9* KD significantly upregulated *PD-L1* in cancer cells (Fig. 8a,b), although *PD-L2* and *CTLA-4* were also modestly upregulated (Fig. 8a,b and Extended Data Fig. 9a,b). Notably, in two of three primary AML cocultures, upregulation of *PD-L1* on Prmt9 inhibition was seen (Fig. 8c and Extended Data Fig. 9c).

To determine if a PRMT9 inhibitor synergizes with PD-1 monoclonal antibody (mAb) treatment, we treated AML samples for 4 days ex vivo. The combination elicited T cell expansion and reduced tumor cell frequency (Fig. 8d,e and Extended Data Fig. 9d,e). Activation of T cells was seen among combination-treated cells (Fig. 8f,g).

We next investigated cooperation between PRMT9 inhibitor and αPD-1 treatment using an A20 lymphoma syngeneic model (Extended Data Fig. 9f). Once A20 tumors reached 100 mm^3, we treated mice with isotype control (vehicle), anti-PD-1 mAb (10 mg kg^{-1} intraperitoneally every other day for 2 weeks), LD2 (100 mg kg^{-1} intratissue injection once a day for 2 weeks) or combined LD2 and anti-PD-1. Tumor volumes were monitored through the end (Extended Data Fig. 9g). A humane endpoint was reached in a vehicle group mouse on day 29. The tumor size of the combined treatment was smaller than that of the vehicle (Ctrl) group starting on day 17. LD2 administration alone significantly decreased tumor size relative to controls after day 21 (Extended Data Fig. 9g–i). We also evaluated LD2 single treatment effects in *NSGS* mice xenografted with A20 cells; treatment modestly decreased A20 tumor growth (Extended Data Fig. 9j,k), probably because of its effects on translation (Extended Data Fig. 9l). Notably, A20 tumor weight in BALB/c mice was reduced in the combination group versus the vehicle controls (Extended Data Fig. 9h,i). LD2 treatment upregulated ISGs and *PD-L1 (Cd274)* (Extended Data Fig. 9m,n). We also observed an increased number of tumor-infiltrating T cells or CD8$^+$ T cells after LD2 treatment or combination treatment (Extended Data Fig. 9o–r). Moreover, a remarkable increase in the number of active CD8$^+$ T cells was seen in the LD2 single treatment group; the effects were enhanced by the combination treatment (Extended Data Fig. 9s–v).

We next evaluated the combination treatment in an MA9 AML transplant model. We treated AML-bearing mice for 3 weeks with vehicle, anti-PD-1 mAb (10 mg kg^{-1} intraperitoneally every other day), LD2 or LD2 plus anti-PD-1. LD2 was administered at a dose of 10 mg kg^{-1} intravenously twice a day. After treatment, compared to LD2 only, combination treatment significantly decreased leukemia engraftment and expanded tumor-specific T cells (Fig. 8h–j). Notably, combination treatment extended mouse survival and decreased LSC activity (Fig. 8k,l).

We established a humanized AML model. Specifically, in a cohort of MHC class I and II double-KO (DKO) *NSG* mice, we implanted 2 million MNCs from an AML specimen using intrafemoral injection of each DKO mouse. DKO mice showed long-term engraftment of T and CD33$^+$ cells (Extended Data Fig. 10a,b), without acute graft-versus-host disease, consistent with other reports[49]. Importantly, we confirmed bone marrow engraftment of human hematopoietic subsets (Extended Data Fig. 10c) and observed selective expansion of the immature

Fig. 7 | Loss of XRN2 methylation underlies *cGAS* activation. **a**,**b**, Phospho-CHK1, CHK2 and γH2AX levels after *PRMT9* KD (**a**) or LD2 (**b**) in THP1 ($n = 2$ independent experiments). **c**, Comet assay of THP1 after *PRMT9* KD for 48 and 72 h. Right: summary of each group ($n = 50$ cells). Scale bar, 50 µm. The *P* value was determined using an unpaired two-sided *t*-test. **d**, Luciferase activity of THP1-IRF cells after KO of the indicated genes. Data are the mean ± s.d. from three independent experiments. **e**, Methylation assay of KHDRBS1 (amino acids 326–339), XRN2 (amino acids 937–950) or DDX3X (amino acids 80–92) peptides. Methylation was analyzed using an anti-MMA antibody ($n = 2$ independent experiments). **f**, XRN2 and DDX3X levels after respective KO ($n = 2$ independent experiments). **g**, Luciferase activity of WT and *cGAS* KO THP1-IRF cells. gRNA-resistant *XRN2* WT and R946K constructs were ectopically expressed in THP1-IRF cells ($n = 5$ independent experiments). A reporter assay was performed using the cells with KO endogenous XRN2. Data are the mean ± s.d. The *P* value was determined using a one-way ANOVA. **h**, Luciferase activity of THP1-IRF cells ($n = 5$ independent experiments). gRNA-resistant DDX3X WT or R88K constructs were ectopically expressed in THP1-IRF cells. A reporter assay was performed using the cells with KO endogenous DDX3X. Data are the mean ± s.d. The *P* value was determined using an unpaired two-sided *t*-test. **i**,**j**, In vitro methylation of XRN2 peptides with PRMT9 (**i**) or PRMT5 (**j**) with increased dose of LD2 (**i**) or EPZ015666 (**j**) ($n = 1$). **k**, XRN2-engineered THP1 cells were prepared for IP using anti-FLAG beads; interactors were detected as indicated ($n = 2$ independent experiments). **l**,**m**, R-loop signals by dot blots (**l**, $n = 2$) or immunostaining (**m**) in THP1 cells. Scale bar, 10 µm. ssDNA, single-stranded DNA. **n**,**o**, R-loop signals in *RNASEH1*-overexpressed THP1 cells treated with LD2 (2.5 µM) (**n**) or *PRMT9* KD (**o**) ($n = 2$ independent experiments). **p**, Cell cycle of THP1 cells treated for 48 h with LD2 (2.5 µM), $n = 5$ independent experiments. Right: statistics. Data are the mean ± s.d. Right: *P* values were determined using a one-way ANOVA. **q**, Phospho-CHK1 in engineered THP1 cells treated with LD2 (2.5 µM) ($n = 2$ independent experiments). **r**, Luciferase activity of THP1-*Lucia* luciferase cells treated with (2.5 µM) LD2 ($n = 5$ independent experiments). Data are the mean ± s.d. The *P* value was determined using a one-way ANOVA.

$CD33^{+}CD34^{+}CD45^{dim}$ subset (Extended Data Fig. 10c). We then divided mice into vehicle and LD2 treatment groups. After 3 weeks of treatment, we observed decreased numbers of leukemic $CD34^{+}$ cells (Fig. 8m,n) and increased numbers of active $CD8^{+}$ T cells (Fig. 8o,p) in LD2 relative to the control group.

Also, we assessed the correlation between PRMT9 activity and the response of PD-1 and PD-L1 inhibitors using clinical datasets[6,50,51]. To do that, we defined the *PRMT9* KD gene signature established from RNA-seq analysis of *PRMT9* KD versus Ctrl AML lines (Fig. 6c and Supplementary Table 9). The signature consists of 102 differentially expressed genes (DEGs) common to two AML cell lines (fold change > 2, $P < 0.05$). Notably, higher levels of the *PRMT9* KD gene signature were positively associated with complete response (CR) to ICI versus progressive disease (PD) in two clinical cohorts (Fig. 8q,r). Relevant to AML, we failed

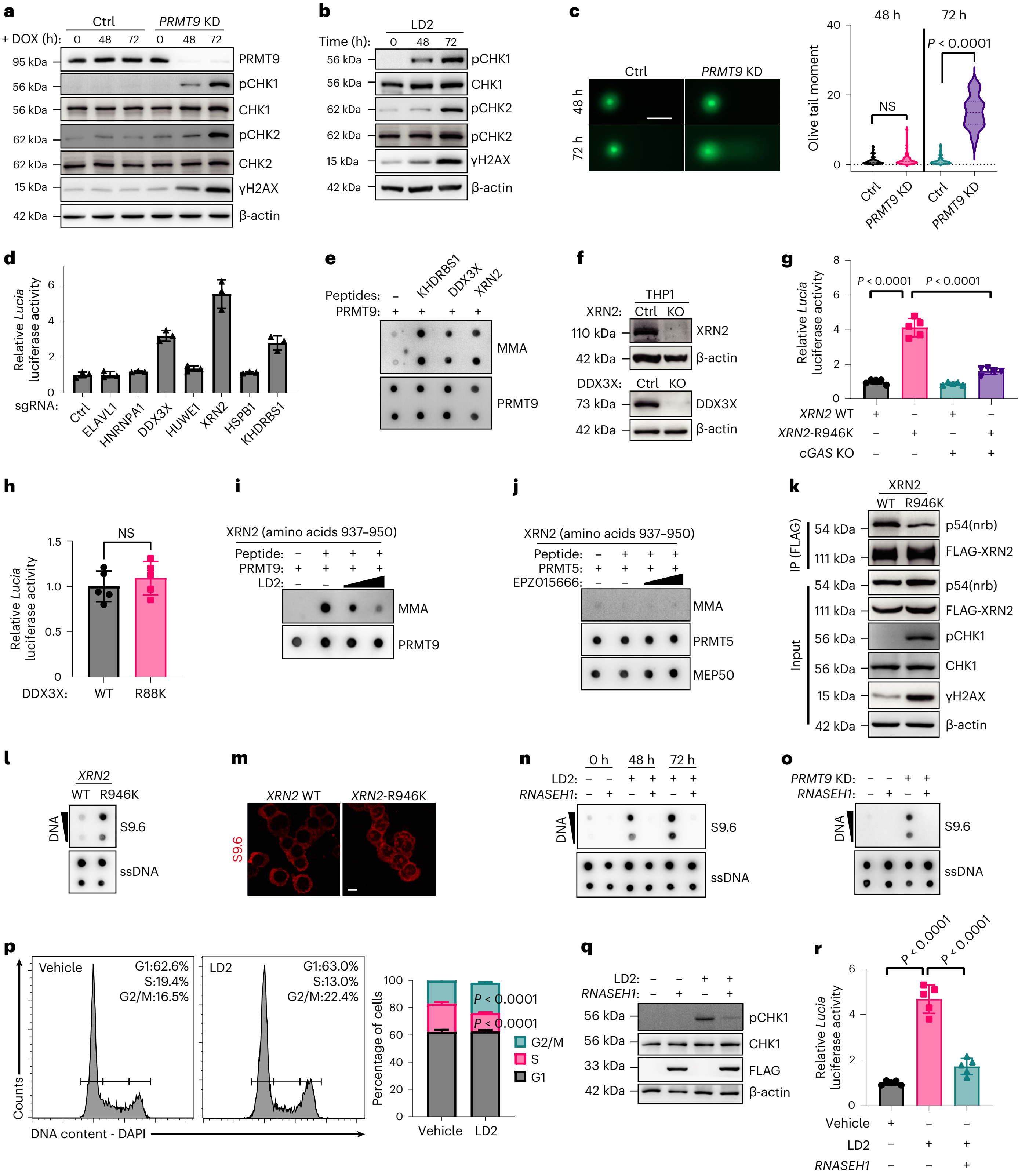

to detect any correlation of the signature with clinical responses to PD-1 inhibitors using the only available dataset (Extended Data Fig. 10d).

Discussion

PRMT9^{hi} LSCs may give rise to immune-evasive leukemia blasts. Our results reveal that targeting PRMT9 not only ablates LSCs but stimulates an anticancer immune response to achieve maximal therapeutic effects. This strategy, when combined with an ICI, could approach a cure. Specifically, our approach targets the arginine methyltransferase PRMT9 to ablate AML LSCs by downregulating the synthesis of short-lived oncoproteins; targeting PRMT9 also induces DNA damage-mediated activation of cGAS and release of cGAMP, thereby cross-priming T cells via a type I IFN response. Moreover, we identified that the lead compound LD2 as a potent inhibitor of PRMT9 activity that promotes robust anti-AML activity (Extended Data Fig. 10e).

PRMT9, one of two SDMA-forming PRMTs, is characterized by a unique duplicated methyltransferase domain[29,52]. In this study, we used a quantitative proteomic method to profile changes in global arginine methylation on PRMT9 knockdown and identified undefined targets. Specifically, methylation at residue R493 enables the PABPC1 protein to bind to the mRNA poly(A) tail, promoting translation. Moreover, XRN2 methylation at R946 may allow complex formation with p54nrb to prevent the DNA double-strand breaks associated with the role of XRN2 in resolving the R-loop (RNA/DNA hybrid) structure[48]. Indeed, PRMT9 inhibition or expression of *XRN2*-R946K in AML cells promoted R-loop formation and ATR signaling, which underlies cGAS activation in cancer cells. Moreover, PRMT9 did not catalyze cGAS methylation (Supplementary Fig. 9).

Our study demonstrates that tumor elimination induced by Prmt9 deletion relies on type I IFN responses. scRNA-seq analysis revealed that the changes in T cell subpopulations seen after *Prmt9* KD are associated with immune memory. Other studies used high-dose cytotoxic chemotherapies that dampen immune responses[53–55]. Interestingly, we found that neither *Prmt9* KO nor LD2 treatment perturbed T cell function.

How does PRMT9 inhibition in cancer cells elicit a distinct response in T cells? In this study, we showed that cGAS-dependent dsDNA sensing by cancer cells is critical for the effects of T cell priming. Notably, leukemia cells express higher levels of cGAS relative to normal counterparts from healthy donors. On *PRMT9* KD, cancer cells accumulate cytosolic dsDNA, providing abundant substrate for cGAS catalysis (Fig. 6i). Such changes in dsDNA are partially due to DNA damage induced by the loss of XRN2 methylation seen after PRMT9 inhibition. Interestingly, GSEA of single-cell transcriptomes from *PRMT9* KD versus control MA9 cells showed significant enrichment of DNA damage response gene signatures (Extended Data Fig. 10f), confirming an association between PRMT9 inhibition and DNA damage.

Moreover, PRMT9 inhibition also downregulated SAMHD1 (Fig. 3g), which antagonizes cGAS–STING activity as reported previously[56]. Consequently, cGAS-activating cancer cells can produce high levels of the immunotransmitter cGAMP. Among all cancers, leukemia cells express the lowest levels of ENPP1, which hydrolyzed cGAMP (Extended Data Fig. 8o,q), allowing sustained cGAMP production in cancer cells. Extracellular cGAMP may be transferred via gap junctions from cancer cells to DCs[57]. Indeed, scRNA-seq analysis of the MA9 model revealed ISG upregulation in DCs (Extended Data Fig. 10g). Moreover, subsequent GSEA analysis showed upregulation of the IFN-α response pathway in T cells from *Prmt9* KD AML bone marrow (Extended Data Fig. 7p). As an outcome of the type I IFN response, T cells (Fig. 5k) exhibited IFN-γ upregulation after *Prmt9* KD. Indeed, we observed significant enrichment of IFN-γ response genes in MA9 cancer cells and in T cells (Extended Data Fig. 10h,i).

Collectively, we showed a biological role for PRMT9 in cancer. We developed a small molecule inhibitor blocking PRMT9 activity. Our study also prompts an appraisal of anticancer drugs with consideration of their impact on immune cells within the tumor microenvironment and provides a rationale for further evaluation of PRMT9 inhibition combined with a PD-1/PD-L1 inhibitor against AML.

Methods

Ethics statement

This study follows ethical regulations. Experiments using patient specimens were approved in part by the institutional review boards of City of Hope Comprehensive Cancer Center (COHCCC) and conducted in accordance with the Declaration of Helsinki (2013). Samples were acquired as part of the COHCCC institutional review board-approved clinical protocol no. 18067. All mouse experiments were completed in accordance with the Guidelines for the Care and Use of Laboratory Animals and were approved by the Institutional Animal Care and Use Committee (IACUC) at COHCCC. Experiments were performed in accordance with a protocol approved by the COHCCC ICUC (no. 15046). The maximum tumor size (humane endpoint) permitted by IACUC is 15 mm (diameter). All animals were euthanized before tumor size reached 15 mm in diameter. Maximum tumor size did not exceed 15 mm.

Patient cells

De-identified, clinically annotated primary patient samples including those derived from peripheral blood or bone marrow were obtained from patients with AML at COHCCC. The annotations are shown in Supplementary Table 1. Normal cells derived from peripheral blood were obtained from the COHCCC. Informed written consent was completed and acquired from all involved participants before sample acquisition.

Fig. 8 | Combining LD2 with an ICI ablates AML. a,**b**, Uniform manifold approximation and projection (UMAP) (**a**) and histogram (**b**) showing *Cd274* (*PD-L1*) and *Pdcd1lg2* (*PD-L2*) expression in MA9 cells from the scRNA-seq analysis of Ctrl (n = 1,827 cells) and *Prmt9* KD (n = 1,124 cells) leukemic cells. Data are the mean ± s.e.m. P values were determined using unpaired two-sided t-tests. **c**, CyTOF of AML MNCs treated with LD2 (2.5 µM for 4 days), colored according to the expression of PD-L1 based on the CD34$^+$CD45^{dim} subsets (n = 3 patients). **d**, CyTOF of AML MNCs after treatment. The frequency of CD3$^+$ T cells and CD34$^+$CD45^{dim} AML blasts were noted. The color bar shows the intensity of CD34 expression. **e**, Relative leukemia cell (CD34$^+$CD45^{dim}) frequencies of AML01 in **d** and Fig. 4m. **f**,**g**, CD69 (**f**) and IFN-γ (**g**) levels in CD8$^+$ T cells in AML01. **h**–**j**, MA9 cells were transplanted (**i**, n = 5 mice per group). We treated AML-bearing mice for 3 weeks with vehicle, a PD-1 inhibitor (10 mg kg^{-1} intraperitoneally every other day), LD2 (10 mg kg^{-1} intravenously twice a day) or LD2 plus PD-1 inhibitor. After treatment, leukemic progenitor (GFP$^+$cKit$^+$) engraftment was assessed (**h**). MA9-specific CD8$^+$ T cells were assessed (representative plots are shown in **j**). Cytomegalovirus (CMV)-specific pentamers were the negative control. **i**, Histograms. **j**, Data summary. Data are the mean ± s.e.m. **h**,**i**, P values were determined using a one-way ANOVA. **k**, As in **h**, Kaplan–Meier curves show the survival of mice (n = 5 mice per group). P values were determined using a log-rank (Mantel–Cox) test. **l**, Secondary transplantation (n = 5 mice per group) based on bone marrow cells from the first transplants (**h**); MA9 (GFP$^+$) cells in the bone marrow were assessed. Data are the mean ± s.e.m. P values were determined using a one-way ANOVA. **m**–**p**, Two million AML MNCs were implanted intrafemorally into an irradiated MHC class I and 2 DKO mouse (**n**,**o**,**p**, n = 6 mice per group). After engraftment, mice were treated with vehicle or LD2 (10 mg kg^{-1} intravenously twice a day). After 3 weeks of treatment, the number and frequency of leukemic CD34$^+$ cells (**m**,**n**) and frequencies of CD8$^+$ T cells expressing CD69 (**o**) and IFN-γ (**p**) were assessed. Data are the mean ± s.e.m. **n**,**p**, P values were determined using an unpaired two-sided t-test. **q**,**r**, *PRMT9* KD gene signature levels in the indicated ICI-treated cohorts of patients enrolled in clinical trials against melanoma (**q**) and BLCA (**r**) cancer with CR and PD[6,50,51]. Single-sample GSEA was applied. Violin plots were used to compare the distribution of NES between groups. Statistical comparisons were carried out using unpaired two-sided t-tests. n; represents the number of patients.

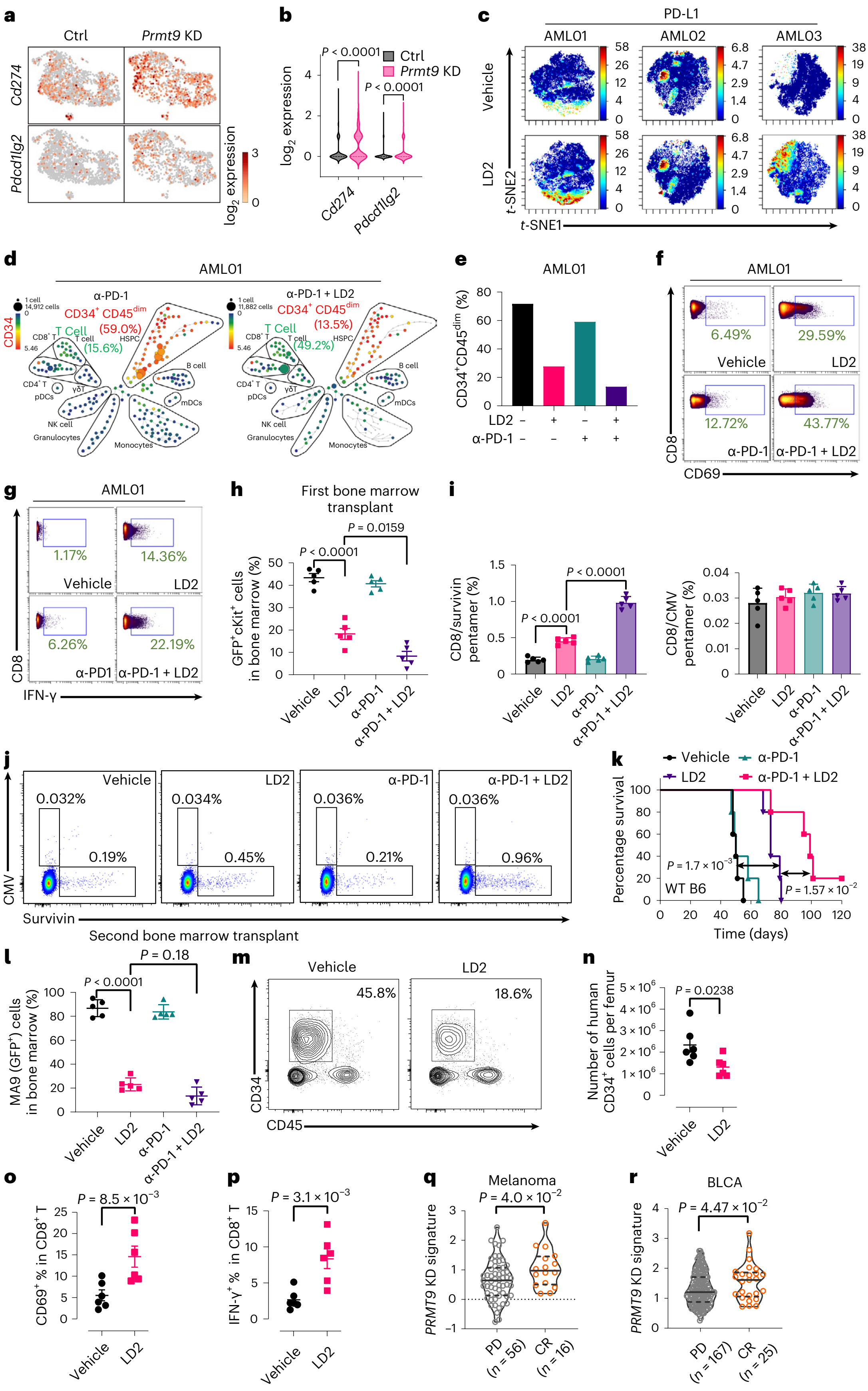
a
Ctrl
Prmt9 KD
Cd274
Pdcd1lg2
log2 expression
3
0
b
P < 0.0001
P < 0.0001
Ctrl
Prmt9 KD
log2 expression
4
2
0
Cd274
Pdcd1lg2
c
PD-L1
AML01
AML02
AML03
Vehicle
LD2
58 26 12 4 0
6.8 4.7 2.9 1.4 0
38 19 9 4 0
t-SNE2
t-SNE1
d
AML01
α-PD-1
α-PD-1 + LD2
CD34+ CD45dim
(59.0%)
(13.5%)
T Cell
(15.6%)
(49.2%)
1 cell
14,912 cells
11,882 cells
CD34
5.46
0
CD8+ T
T cell
HSPC
B cell
CD4+ T
γδT
pDCs
mDCs
NK cell
Granulocytes
Monocytes
e
AML01
CD34+CD45dim (%)
80 60 40 20 0
LD2 – + – +
α-PD-1 – – + +
f
AML01
6.49%
29.59%
Vehicle
LD2
12.72%
43.77%
α-PD-1
α-PD-1 + LD2
CD8
CD69
g
AML01
1.17%
14.36%
Vehicle
LD2
6.26%
22.19%
α-PD1
α-PD-1 + LD2
CD8
IFN-γ
h
First bone marrow transplant
P = 0.0159
P < 0.0001
GFP+cKit+ cells in bone marrow (%)
50 40 30 20 10 0
Vehicle
LD2
α-PD-1
α-PD-1 + LD2
i
P < 0.0001
P < 0.0001
CD8/survivin pentamer (%)
1.5 1.0 0.5 0
CD8/CMV pentamer (%)
0.04 0.03 0.02 0.01 0
Vehicle
LD2
α-PD-1
α-PD-1 + LD2
j
Vehicle
LD2
α-PD-1
α-PD-1 + LD2
0.032%
0.19%
0.034%
0.45%
0.036%
0.21%
0.036%
0.96%
CMV
Survivin
k
Vehicle
α-PD-1
LD2
α-PD-1 + LD2
Percentage survival
100 80 60 40 20 0
P = 1.7 × 10−3
P = 1.57 × 10−2
WT B6
0 20 40 60 80 100 120
Time (days)
Second bone marrow transplant
l
P = 0.18
P < 0.0001
MA9 (GFP+) cells in bone marrow (%)
100 80 60 40 20 0
Vehicle
LD2
α-PD-1
α-PD-1 + LD2
m
Vehicle
LD2
45.8%
18.6%
CD34
CD45
n
P = 0.0238
Number of human CD34+ cells per femur
5 × 106
4 × 106
3 × 106
2 × 106
1 × 106
0
Vehicle
LD2
o
P = 8.5 × 10−3
CD69+ % in CD8+ T
25 20 15 10 5 0
Vehicle
LD2
p
P = 3.1 × 10−3
IFN-γ+ % in CD8+ T
15 10 5 0
Vehicle
LD2
q
Melanoma
P = 4.0 × 10−2
PRMT9 KD signature
3 2 1 0 −1
PD (n = 56)
CR (n = 16)
r
BLCA
P = 4.47 × 10−2
PRMT9 KD signature
4 3 2 1 0
PD (n = 167)
CR (n = 25)

MNC separation, CD34$^+$ cell enrichment or CD3$^+$ T cell depletion was performed as described previously[58].

Cell culture

Molm13 (catalog no. ACC 554, DSMZ), MV4-11 (catalog no. CRL-9591, ATCC), THP1 (catalog no. TIB-202, ATCC), NB4 (catalog no. ACC 207, DSMZ), U937 (catalog no. CRL-1593.2, ATCC), HL-60 (catalog no. CCL-240, ATCC), MA9.6ITD and RAJI (catalog no. ACC 319, DSMZ), UPN1 (catalog no. CVCL_A795, Cellosaurus), BL41 (catalog no. ACC 160, DSMZ), Rec1 (catalog no. ACC 584, DSMZ), OCI-Ly3 (catalog no. ACC 761, DSMZ) and A20 (a gift from Y. Fu) were cultured in Roswell Park Memorial Institute (RPMI) 1640 medium with 10% FCS as described previously[58,59]. All other cell lines, including 293FT (catalog no. R70007, Thermo Fisher Scientific), DMS273 (a gift from R. Salgia), DMS114 (a gift from R. Salgia), SW1573 (a gift from E. Wang), A549 (a gift from E. Wang), SW620 (catalog no. CCL-227, ATCC), HCT116 (catalog no. CCL-247, ATCC), HepG2 (catalog no. HB-8065, ATCC), PC3 (a gift from S. Priceman), DU145 (a gift from S. Priceman), MDA-MB-231 (catalog no. CRM-HTB-26, ATCC), HT1197 (catalog no. CRL-1473, ATCC), A172 (catalog no. CRL-1620, ATCC), MIAPACA2 (catalog no. CRM-CRL-1420, ATCC) and HT1080 (catalog no. CCL-121, ATCC) were cultured in DMEM with 10% FCS. MA9.6ITD cells (MLL-AF9 plus *FLT3*-ITD) were established by J. Mulloy[60]. The human primary normal and AML CD34$^+$ cells used for transduction were maintained as described previously[59]. Specifically, as noted in that paper, the medium was StemSpan SFEM (STEMCELL Technologies) supplemented with 50 ng ml^{-1} recombinant human stem cell factor (SCF), 100 ng ml^{-1} Flt3 ligand (Flt3L), 100 ng ml^{-1} thrombopoietin, 25 ng ml^{-1} interleukin-3 (IL-3) and 10 ng ml^{-1} IL-6 (PeproTech). Mouse AML cells were cultured in RPMI 1640 medium with cytokines (mouse IL-3, 10 ng ml^{-1}; mouse IL-6, 10 ng ml^{-1}; mouse SCF, 30 ng ml^{-1}; Supplementary Table 10) as described previously[59].

Mice

In all experiments, male and female, 6–10-week-old, WT C57BL/6J (strain no. 000664, The Jackson Laboratory), B6(Cg)-*Rag2*$^{tm1.1Cgn}$/J (strain no. 008449, *Rag2*$^{-/-}$, The Jackson Laboratory), B6(Cg)-*Ifnar1*$^{tm1.2Ees}$/J (strain no. 028288, *Ifnar1*$^{-/-}$, The Jackson Laboratory), *Kmt2a*$^{tm2(MLLT3)Thr}$/KsyJ (strain no. 009079, MLL-AF9 knock-in, The Jackson Laboratory), B6.129S(C)-*Batf3*^{tm1Kmm}/*J* (strain no. 013755, *Batf3*$^{-/-}$, The Jackson Laboratory), NOD.Cg-*Prkdc*^{scid} *Il2rg*^{tm1Wjl}/SzJ (strain no. 005557, *NSG*, The Jackson Laboratory), NOD.Cg-*Prkdc*^{scid} *Il2rg*^{tm1Wjl} Tg(CMV-IL3,CSF2,KITLG)1Eav/MloySzJ (strain no. 013062, *NSGS*, The Jackson Laboratory) and NOD.Cg-*Prkdc*^{scid} *H2-K1*$^{b-tm1Bpe}$ *H2-Ab1*^{em1Mvw} *H2-D1*^{tm1Bpe} *Il2rg*^{tm1Wjl}/SzJ (strain no. 025216, *NSG-MHC I/II DKO*, The Jackson Laboratory) mice were used. B6-Ly5.1 (CD45.1, NCI 564) and BALB/c (NCI 028) mice were available from an outside vendor. Male and female mice were housed at the COH Animal Resource Center. All care and experimental procedures followed established institutional guidelines. The mouse room is conditioned with a 14 h light–10 h dark cycle, temperatures of 65–75 °F and 40–60% humidity. The procedure was run in accordance with a protocol approved by the IACUC at COHCCC.

Mouse experiments were performed once: Fig. 2d,e,h (male and female; five WT B6 mice per group); in Fig. 2f,g (male and female; five WT B6 mice per group); Fig. 2q (male and female; eight *NSGS* mice per group); Fig. 2r (male and female; eight *NSGS* mice for Ctrl, seven *NSGS* mice for *Prmt9* KD); Extended Data Fig. 2p (male and female; six *Prmt9*$^{loxP/loxP}$/*Mx1Cre*$^-$ mice for *Prmt9* WT, nine *Prmt9*$^{loxP/loxP}$/*Mx1Cre*$^+$ mice for *Prmt9* KD); Extended Data Fig. 2q (male and female; eight *Prmt9*$^{loxP/loxP}$/*Mx1Cre*$^-$ mice for *Prmt9* WT, 15 mice (*Prmt9*$^{loxP/loxP}$/*Mx1Cre*$^+$) for *Prmt9* KD); Extended Data Fig. 2r (male and female; seven B6-Ly5.1 mice per group); Fig. 5d (male and female; seven WT B6 mice per group); Fig. 5e (male and female; five *Rag2*$^{-/-}$ mice per group); Fig. 5f (male and female; five *NSGS* mice per group); Fig. 5g (male and female; seven WT B6 mice per group); Fig. 5s (male and female; five WT B6 mice for naive mice, four survival mice from Fig. 5d for survivors); Fig. 5v (male and female; five *Ifnar1*$^{-/-}$ mice for *Ifnar1* KO, six WT B6 mice for *Ifnar1* WT); Fig. 6j (male and female; seven WT B6 mice for the *Prmt9* KD group, five WT B6 mice for each of the other three groups); Fig. 6m (male and female; seven WT B6 mice for *cGAS* KO + *cGAS*ΔN group, five WT B6 mice for each of the other two groups); Fig. 6s (seven WT B6 mice for each Batf3 WT group, five *Batf3*$^{-/-}$ mice for the *Batf3* KO group); Extended Data Fig. 7c (seven WT B6 mice for the Ctrl and *Prmt9* KD groups, five WT B6 mice for the T and NK cell depletion groups); Extended Data Fig. 9g–i (five *BALB/c* mice per group); and Extended Data Fig. 9j,k (five *NSGS* mice per group). scRNA-seq and bulk RNA-seq were performed once per sample and are shown in Figs. 1e, 5h and 6c. If not otherwise specified, in vitro experiments were repeated at least three times.

DNA constructs and oligonucleotides

The CD530-EF1A-IRES-GFP vectors were purchased from System Biosciences. The CD530-EF1A-T2A-GFP vectors were modified from CD530-EF1A-IRES-GFP, replacing IRES with T2A sequences. Full-length WT or LDIG-to-AAAA mutant PRMT9 (ref. 29) were cloned into CD530-EF1A-IRES-GFP vectors. FLAG-tagged XRN2 and FLAG-tagged DDX3X variants, and FLAG-tagged either full-length WT or C-terminal (amino acids 436–636) PABPC1 or R493K, R481K, R506K or 3RK mutants were cloned into the CD530-EF1A-T2A-GFP vector. All plasmids were synthesized by Genscript. shRNAs targeting human *PRMT9*, mouse *Prmt9*, *PABPC1* and *CREB1* were purchased from Sigma-Aldrich (MISSION shRNA) and cloned into pLKO-SFFV-RFP, as described elsewhere[58]. cGAS WT and the activation mutant ΔN were purchased from Addgene and constructed into a DOX-inducible expression vector. SMARTvectors with shPRMT9 were purchased from Dharmacon (Horizon Discovery). The oligonucleotides used are listed in Supplementary Table 11.

Compounds

Compounds were sourced from the NCI Developmental Therapeutics Program (DTP), ZINC libraries or MolPort. The PEGylated liposome packaging of LD2 used for animal treatment was prepared using the thin film hydration method. Lipids (distearoylphosphatidylcholine, cholesterol and DSPE-PEG(2000) at a ratio of 3:1:0.2) plus compound were dissolved in chloroform; then, organic solvent was separated in a vacuum to form a thin film. Subsequently, lipids were hydrated in PBS, pH 7.4, at 60 °C to form liposomes.

Lentiviral transduction

Virus production was as described previously[61]. HEK 293T cells were transfected with pMD2.G and psPAX2 packaging vectors plus lentivectors designed to overexpress or knock down genes using the calcium phosphate method as described previously[61]. Supernatants containing virus particles were filtered and concentrated. Viral infection was performed as described previously[61].

qPCR

RNA was prepared according to the TRIzol reagent protocol. After generation of complementary DNA, qPCR with reverse transcription was performed as described previously[59]. The primers used are listed in Supplementary Table 11.

IP and immunoblotting

Cell lysates were prepared in a buffer containing 50 mM Tris, pH 7.4, 150 mM NaCl and 1 mM EDTA supplemented with protease inhibitors. Cell lysates were incubated with anti-FLAG beads or interested primary antibody (Sigma-Aldrich) overnight and denatured for immunoblotting. Proteins of interest were probed with primary and secondary antibodies. Signals were detected using the SuperSignal West Pico or Femato kits. All immunoblots were imaged using the G:BOX Chemi XX6 gel doc system and quantified with the ImageJ software (NIH).

ChIP–qPCR

Samples were prepared according to the protocol of the SimpleChIP Plus Enzymatic Chromatin IP Kit (catalog no. 9005, Cell Signaling Technology). Immunoprecipitates were exposed to anti-CREB1 (catalog no. SC-240, Santa Cruz Biotechnology) and anti-H3K27Ac antibodies, plus Protein G magnetic beads. After reversing, DNA was enriched; this was followed by qPCR.

Flow cytometry

Cells derived from the bone marrow or spleen samples were washed with PBS containing 1% FCS and then passed through a single-cell strainer and subjected to lysis of red cells. Before flow cytometry, cells were stained with the indicated antibodies in the same buffer. Flow cytometry analysis was performed. Data analysis was performed using FlowJo v.10. Molm13 cell engraftment in mice was determined using an anti-human CD45 antibody. CD45.2$^+$ donor cells from transplants were determined using anti-mouse CD45.1 and CD45.2 antibodies. Mouse HSPCs were determined by staining with anti-mouse lineage antibody, including cKit, Sca-1, CD16 and CD32, and CD34 antibodies and a lineage antibody cocktail, including anti-mouse CD3, CD4, CD8, CD11b, CD11c, CD19, CD41, Ter119, B220, IgM, NK1.1, Gr-1 and interleukin-7 receptor subunit alpha (IL-7Rα). Anti-mouse Mac1, Gr-1, B220 and Ter119 were used to define mouse bone marrow differentiation. We also detected antigen-specific T cells in tumors as described previously[44]. For intracellular staining, fixed cells were incubated once with antibodies against IFN-γ (clone XMG1.2) and granzyme B (clone QA16A02). To define the human primary samples, we used the following markers: T cells (CD3$^+$), B cells (CD19$^+$/CD20$^+$), monocytes (CD14$^+$) and DCs (HLA-DR$^+$CD34$^-$CD33$^-$CD3$^-$CD19$^-$CD20$^-$CD14$^-$CD56$^-$), as well as the immature CD33$^+$CD34$^+$CD45$^{\mathrm{dim}}$ subset. CD69 and IFN-γ staining was used to determine T cell status. For the cell cycle studies, fixed cells were stained with 4,6-diamidino-2-phenylindole (DAPI).

Competitive transplantation

Bone marrow cells (0.5 × 10^{6}per transplant) from CD45.2$^+$ *Prmt9*$^{\mathrm{loxP/loxP}}$ *MxCre*$^+$ or *Prmt9*$^{\mathrm{loxP/loxP}}$*MxCre*$^-$ mice were combined with CD45.1$^+$ bone marrow cells (at 1:1 ratio) and then implanted into lethally irradiated (900 cGy) B6-Ly5.1 mice by intravenous injection. Peripheral blood samples were collected and assessed with CD45.1 and CD45.2 antibodies. Mouse recipients were induced with pIpC (InvivoGen) intraperitoneally 15 mg kg^{-1} every other day for 7 days; CD45.2$^+$ chimerism in peripheral blood was assessed every 4 weeks.

Limiting dilution assays

For the limiting dilution assays, to evaluate LSC frequencies, AML cells were suspended in Colony Forming Cell growth medium with DOX to induce *Prmt9* KD and plated in multi-well plates. To evaluate the frequency of leukemia-initiating cells in vivo, bone marrow cells isolated from Ctrl or *Prmt9* KDMA9 AML mice were injected intravenously into sublethally conditioned recipient mice, as described in Supplementary Table 7. The number of recipient mice with leukemia development was determined in each group. The frequency of LSCs and LICs was determined using the ELDA software.

AML mouse model and in vivo bioluminescence imaging

To assess the effect of *Prmt9* KO and KD in vivo, MA9 or CMM cells were transduced with lentiviral vectors harboring a luciferase reporter. Cells were used for intravenous inoculation into sublethally irradiated CD45.1 B6 mice or WT B6, *Rag2*$^{-/-}$ or *NSGS* mice. As for bioluminescence imaging, mice were administered 150 mg kg^{-1} D-luciferin (GoldBio) within PBS, followed by analysis using Lago X. Bioluminescent signals were quantified using the Aura imaging software (Spectral Instruments Imaging). Total values were determined using the regions of interest and photons s cm^2 sr. To identify the immune subsets contributing to leukemia regression after *Prmt9* KD, we performed antibody-based depletion with an initial dose of combined anti-CD4 and anti-CD8 treatment or anti-NK1.1 treatment administered 1 day before in vivo DOX administration to *Prmt9* KD mice. Antibodies (400 μg) were injected intraperitoneally twice the first week, and then at 200 μg twice weekly to maintain NK or T cell depletion. To assess DC function in *Prmt9* KD outcomes, we implanted Batf3 WT or *Batf3* KO mice with AML cells for further evaluation.

Assessment of cell growth, apoptosis and colony formation

Cell growth was assessed using the CellTiter-Glo Assay Kit (Promega Corporation). Apoptosis was determined using annexin V or DAPI. Colony formation capacity was determined as described previously[58,59].

SILAC-based quantitative proteomics analysis

Proteomics sample preparation. For SILAC, Molm13 cells were cultured in SILAC RPMI 1640 medium (catalog no. 88365, Thermo Fisher Scientific) with 10% FCS (catalog no. A3382001, Thermo Fisher Scientific) and either light L-lysine (catalog no. 89987, Thermo Fisher Scientific) and L-arginine (catalog no. 89989, Thermo Fisher Scientific) for control cells, or heavy lysine (catalog no. 88209, Thermo Fisher Scientific) and L-arginine (catalog no.89990, Thermo Fisher Scientific) for inducible *PRMT9* KD cells, for at least ten passages to ensure full incorporation of light or heavy L-lysine and L-arginine.

After 3 days of DOX induction in both control and *PRMT9* KD cells, light-labeled and heavy-labeled cells were combined at 1:1 ratio. Cells were washed and centrifuged at 300*g* for 5 min. Cell pellets were lysed in 9 M urea with protease and phosphatase inhibitors in HEPES (pH 8.0) buffer. Samples underwent four cycles of sonication for 30 s each using a microtip sonicator (VibraCell VCX130, Sonics & Materials) operating at 50% amplitude. Lysates were centrifuged at 20,000*g* for 15 min; protein quantification was performed by using a bicinchoninic acid (BCA) assay. An equal amount of extracted protein from heavy and light SILAC culture was mixed for further digestion. The sample was first reduced by incubation with dithiothreitol (DTT) (5 mM, 55 °C) and then alkylated by incubation with iodoacetamide (10 mM) in the dark. The sample was diluted fourfold before sequential digestion first with LysC (2 h) and then overnight with Trypsin Gold. Digestion was quenched using trifluoroacetic acid and the sample was desalted using 0.7 ml of a Sep-Pak Classic C18 column (Waters). Eluted peptides were speedvac'd to dryness and reconstituted in 1.4 ml immunoaffinity purification buffer followed by peptide quantification using a BCA assay. We subjected 5% of peptides to global quantitative proteomics analysis and 95% of the rest to methyl-R peptide enrichment. This consisted of sequential incubation of peptides with anti-MMA antibody beads (catalog no. 12235, Cell Signaling Technology) and anti-SDMA antibody beads (catalog no. 13563, Cell Signaling Technology). Enriched peptides were reconstituted in 10 μl loading solvent (98% water, 2% acetonitrile, 0.1% formic acid); 1 μg of nonenriched peptides was used for global protein identification.

Results acquisition. Data were obtained on an Orbitrap Fusion Lumos mass spectrometer (methylated peptides) or Orbitrap Eclipse with FAIMS Pro interface (unmodified peptides) coupled to a U3000 RSLCnano LC system with running binary solvent A (0.1% formic acid in water) and solvent B (0.1% formic acid in acetonitrile) at 300 nl min^{-1}. Methylated peptides (5 μl per injection) were directly loaded on a 25 cm EasySpray C18 column and eluted over a 120-min gradient as follow: 80 min with 2–19% B, 20 min with 19–30% B, 5 min with 30–98% B, followed by 2 min of high organic wash and return to initial conditions in 1 min. Unmodified peptides (1 μg peptides, 5 μl per injection) were directly loaded on a 50-cm EasySpray C18 column and eluted over 240 min using the following gradient: 12 min with 2–5% B, 158 min with 5–19% B, 40 min with 19–30% B, 9 min with 30–90% B, followed by 4 min of high organic wash and return to initial conditions in 2 min. Using a duty cycle of 3 s (Lumos) or 1 s (Eclipse) per FAIMS CV (−40/−60/−80), most abundant precursors were fragmented using higher-energy collisional dissociation (32% normalized collisional energy on Eclipse and 35% normalized collisional energy on Lumos) and measured in the ion trap. Dynamic exclusion was set to 60 s to prevent resampling of previously analyzed precursors.

Proteomics data analysis. MS raw files were searched against the human UniProt protein database (downloaded in 2020, 42,373 entries) and a common contaminant database using MaxQuant v.1.6.17.0. The results were filtered to 1% protein and site false discovery rate (FDR). The resulting methyl peptide SILAC ratios obtained from the MaxQuant evidence.txt output file were normalized to their protein SILAC ratios before further analyses[62].

R-methyl analysis

Motif analysis was performed using the iceLogo web application as described previously[30].

Polysome profiling

We performed polysome profiling as described previously[28]. Engineered Molm13 cells were DOX-induced for 3 days to delete PRMT9 expression and then treated for 5 min with 100 μg ml^{-1} cycloheximide. After treatment, cells were collected and lysed. We prepared sucrose density gradients (15–45% w/v) using a Gradient Master (BioComp Instruments). Then, the supernatant from the cell lysates was separated using centrifugation and fractionation. The collected RNA was further assessed in the qPCR analysis.

OPP protein synthesis assay

Protein synthesis was assessed by using the Click-iT Plus OPP Assay Kit (Thermo Fisher Scientific), with modifications. Briefly, treated cells were exposed to Click-iT OPP, then washed with PBS and fixed. After permeabilization for 15 min, cells were reacted with cocktail, then analyzed using flow cytometry.

In vitro methylation assay

The assay was performed in a 30-μl reaction with 50 mM Tris HCl, pH 7.4, 50 mM NaCl, 50 mM KCl, 1 mM $MgCl_2$ and 1 mM DTT buffer. Specifically, 1 μg purified PABPC1-CT protein or synthesized peptides, 1 μg purified PRMT9 protein and 5 μM of SAM (Cayman Chemical) were combined. Methylated proteins and peptides were detected with immunoblot or dot blot assays using anti-pan-SDMA, anti-pan-MMA, anti-pan-ADMA or our in-house PABPC1 R493me antibody. The R493me antibody was created by Genemed Synthesis. For the ex vivo tritium labeling of the methylation assay, 1 μg purified PRMT9 protein, 1 μg HA-tagged PABPC1 WT or corresponding PABPC1-R481K/R493K/R506K (3RK) protein, which were immunoprecipitated from 293T cells, and 1 μl *S*-adenosyl-L-[methyl-3H] methionine (78 Ci mmol^{-1}) was added to a 30 μl reaction mixture at 30 °C for 1 h. Samples were separated and transferred to polyvinylidene membranes for further assessment.

PRMT9 structure-based virtual screening

The crystal structure of human PRMT9 (Protein Data Bank (PDB) ID 6PDM; 2.45 A resolution) was used for virtual screening. Missing loops were added using a molecular operating environment loop modeler. A box size of 25 × 21 × 27 Å^3 centered around the cocrystalized chemical probe was used for screening, which includes both the SAM pocket and catalytic pocket in the N-terminal methyltransferase domain (amino acids 150–520). To rank the binding affinity, parallel AutoDock Vina[63,64] runs were conducted on a local computer cluster. Seven hundred thousand compounds from the ZINC library were selected using the following criteria: molecular weight 350–450, log $P < 3$, total charge −2e to +2e and availability. In addition, we also screened the NCI library (NCI DTP 260,000 compounds). Each ligand was docked ten times and ranked according to the lowest binding energy score. After screening, we purchased the top 300 candidates (142 of them were available) from the NCI DTP and the top 100 candidates (70 of them were available) from the ZINC library to assess anti-AML activity. To estimate lead compound selectivity, we also performed Vina docking of LD2 into human CARM1 (PDB ID 5U4X), PRMT5 (PDB ID 4X61), PRMT7 (PDB ID 4M38) and PRMT9. To compare LD2 binding to PRMT5 versus PRMT9, we carried out two replicas of 100-ns molecular dynamics simulation of LD2 docked into each.

Saturation transfer difference and Carr–Purcell–Meiboom–Gill NMR assays

Maltose binding protein (MBP)-tagged PRMT9 core methyltransferase domain (150–474) protein was expressed and purified by Genscript. Briefly, the PRMT9 core methyltransferase domain sequence was inserted into the pMAL-c5X vector between the Nde I and EcoR I sites. Tagged protein was expressed in BL21 and purified on an MBP column, followed by Superdex 200 and Q Sepharose columns. Proteins were sterile-filtered and lyophilized after extensive dialysis against the NMR buffer (50 mM NaH_2PO_4, pH 7.5). Deuterium oxide-based sodium phosphate buffer was used with 5% DMSO-d_5. For the STD NMR assay, the molar ratio of LD2 to PRMT9 was 60:1 in which the concentration of PRMT9 was 0.67 μM; 50 μM trimethylsilylpropanoic acid-d_4 was used as the internal reference. The molar ratios between PMRT9 and LD2 were 1:20, 1:40 and 1:60, in addition to a control sample with free LD2. LD2 concentration in the Carr–Purcell–Meiboom–Gill (CPMG) experiments was 40 μM. The NMR saturation transfer difference (STD) experiments were carried out at 25 °C on a 700-MHz Bruker Ascend system equipped with a 5-mm triple resonance cryogenic probe as described previously[65]. The CPMG experiment was performed as described previously[66]. Data were analyzed using Bruker TopSpin v.3.6.

Thermal shift assay

We also assessed whether LD2 binds to PRMT9 directly in vivo; to do so, a cellular thermal shift assay was performed as described previously[39,40]. We first engineered Molm13 cells to overexpress FLAG-tagged PRMT9 WT or PRMT9 mutant (W152A, D258A and E433A; all three residues are predicted drug and PRMT9 binding sites). Five million cells were pretreated with 2.5 μM LD2 overnight. DMSO was used as the control. Cells were aliquoted in each tube and heat-shocked using Thermal Cycler at the indicated temperatures. Cells were then lysed for the immunoblot assay. Experiments were performed using three biological replicates.

Primary AML MNC culture, mass cytometry staining, acquisition and analysis

Two million MNCs from AML bone marrow specimens were cultured per well in 24-well plates in IMDM plus 20% FCS under physiological cytokine conditions as described previously[41,42] (granulocyte-macrophage colony-stimulating factor in 200 pg ml^{-1}, granulocyte colony-stimulating factor in 1 ng ml^{-1}, SCF in 200 pg ml^{-1}, IL-6 in 1 ng ml^{-1}, macrophage inflammatory protein-1 alpha in 200 pg ml^{-1} and leukemia inhibitory factor in 50 pg ml^{-1}). We then used the EasySep Dead Cell Removal Kit (STEMCELL Technologies) to ensure more than 95% living cells before culture. Cells were treated with vehicle (dimethylsulfoxide), 2.5 μM LD2, anti-PD-1 (pembrolizumab, 10 μg ml^{-1}, SIM0010, Bio X Cell) or LD2 plus anti-PD-1 for 4 days at 37 °C. On day 4, cells were pretreated for 6 h with brefeldin A and subjected to CyTOF immunostaining with customized surface or intracellular marker antibodies, according to Fluidigm CyTOF protocols (PN400279A4). An untreated peripheral blood mononuclear cell sample from a healthy donor served as a control for phenotyping. Samples were acquired on a Fluidigm Helios. Data were normalized and saved as FCS files before analysis using the Cytobank software (https://premium.cytobank.org/). After data were cleaned up, spanning-tree progression analysis for density-normalized events was used to cluster AML cells and immune cell subpopulations based on the median level of each.

In silico analysis of CTL levels in primary AML samples

For *CD8A*, *CD8B*, *GZMA*, *GZMB* and *PRF1*, the average expression levels of these genes were used to estimate CTL levels in AML samples[43,67]. We carried out in silico tests to calculate the ratio of PRMT9^{hi} and PRMT9^{lo} patients exhibiting high versus low CTL scores using both GSE144688, which includes 526 samples of patients with AML, and GSE12417, which includes 163 patient samples. For each patient, high versus low CTL scores were decided according to cutoff of 0.5 for the *z*-score. A Fisher's exact test was used to assess significance.

scRNA-seq

Library preparation. Bone marrow cells in MA9-transplanted mice, and bone marrow and spleen cells in Ctrl and *Prmt9* KD mice administered DOX in drinking water over 7 days, were collected for analysis. Single cells were resuspended in 0.4% BSA and loaded to generate an emulsion of single-cell gel beads. Approximately 5,000–10,000 cells were loaded per channel. Libraries were prepared using the Single Cell 3′ Library & Gel Bead, Single Cell 3′ Chip and i7 Multiplex Kits, according to the Single Cell 3′ Reagent Kits v2 User Guide (part no. CG00052 Rev A). Libraries were sequenced on an Illumina HiSeq 4000 system.

Data processing. We used the Cell Ranger Single Cell Software Suite to perform single-cell 3′ gene counting and aggregation of multiple samples to generate raw counts, cell barcodes and gene features. The R package Seurat was run as the platform to implement all data processing procedures[68].

Quality control, normalization and batch removal. Cell quality control was executed as follows: the minimum detected genes (3) in each cell; the minimum number of cells (200) related to each gene; and the maximum fraction (0.2%) of counts from mitochondrial genes per cell barcode. The high-count depth threshold (2,000) was used to filter out potential doublets. Then, the count matrix was normalized to obtain the correct relative gene expression abundance between cells[69]. Then, the R package Harmony was applied to remove batch effects due to biological differences between cell types or states.

Feature selection, dimension reduction and visualization. To retain informative genes with high variability, genes with small variations (below 2) among all cells were filtered out. Then, the dimensions of count matrices were reduced using dedicated dimension reduction algorithms, such as UMAP and *t*-distributed stochastic neighbor embedding (*t*-SNE). Two-dimensional visualization outputs were then generated using the leading reduced components in the UMAP and *t*-SNE plots.

Clustering and annotation. UMAP-related processed data were regarded as the input of cell clustering. Neighborhood distances among all cells were determined to infer the identity of each cell. Then, clusters were acquired via specified distance metrics (Euclidean distance). Furthermore, for each cluster, the R package MAST was used to deduce significant DEGs. These DEGs were considered markers of a cluster and were used for annotation purposes. Annotations were conducted manually by comparing marker genes with the literature and arranging cell categories. In addition, automatic annotation of cell clusters was done using the R package SingleR, as described previously[70]. By combining both annotation styles, the final cell type labels of each cluster were acquired.

GSEA (for T cell and MA9 clusters). For the cell type clusters of interest, GSEA was performed based on preordered genes ranked using MAST-derived ($-\log_{10}(P_{adj}) \times$ sign (log fold change)) with 1,000 permutations[71]. The gene sets of the Hallmark, Kyoto Encyclopedia of Genes and Genomes, chemical genetic perturbation and Gene Ontology-Biological Process categories of the Molecular Signatures Database were considered as the signatures. Finally, specific enriched genes within a cluster were visualized by averaging their expression among all cells in that cluster. Key enriched gene expression was rescaled by *z*-scores and visualized in the heatmap.

T cell subset identification. scRNA-seq uncovered ten distinct T cell clusters (c0–c9). c0 cells expressed *Cd4* and *CD62L*, but not the effector and memory T cell marker *Cd44* or T cell activation genes. Thus, c0 was defined as naive CD4$^+$ T cells. Similarly, c1 cells expressed *Cd8a* and *CD62L* but not *Cd44* or other T cell activation markers and were defined as naive CD8$^+$ T cells. c2 cells expressed *Cd8a*, *Cd44* and *Sell,* and intermediate levels of *Tbx21* (T-bet) and *Eomes*, and represented a memory CD8$^+$ T cell population. c3 cells expressed high *Cd4*, *Cd44* and *Icos*, *Ctla4, Tnfrsf4* and *Pdcd1*, but did not express *CD62L* and were defined as activated and effector CD4$^+$ T cells. c5 cells expressed *Cd44* and showed the highest levels of *Ifng*, *Gzmb*, *Icos*, *Tim-3*, *Il2ra*, *Tnfrsf18* and *Lag3*, considered as differentiated CTLs. c6 cells were defined as T$_{reg}$ cells because they express *Cd4*, *Il2ra (Cd25)* and *Foxp3*. c4, c7, c8 and c9 cells contained both CD4$^+$ and CD8$^+$ T cells. c4 and c9 showed lower levels of activation markers, and lower *CD62L* and higher *Cd44*, suggesting that they represent T$_{eff}$ cell populations. c7 expressed only the naive T cell marker *CD62L*, indicating a naive population, while c8 expressed lower *CD62L* and higher *Cd44*, but did not express other T cell activation markers, suggesting it represents a memory T cell population.

Bulk RNA-seq analysis

Total RNA was prepared using the TRIzol reagent (Thermo Fisher Scientific). RNA quality (RNA integrity number) was assessed and sequenced on an Illumina HiSeq 2500 system. RNA-seq reads were aligned with default settings. Count data were normalized. Genes were defined as differentially expressed if the fold change was less than 1.5 or less than 0.67, with an FDR less than 0.05, and at least one sample showing reads per kilobase per million mapped reads greater than 1. We performed hierarchical clustering of DEGs using Cluster v.3.0 with Pearson correlation distance and average linkage, and visualized them with Java TreeView. Enrichment analysis on the pathways of Hallmark, Kyoto Encyclopedia of Genes and Genomes and chemical genetic perturbation was performed using GSEA.

Detection of cGAMP

cGAMP levels were detected as reported elsewhere[72,73]. THP1 cells were DOX-treated to induce *PRMT9* KD for 2 days; serum-free Phenol Red RPMI (Thermo Fisher Scientific) medium was replaced for another 24 h. Conditioned medium was collected and cGAMP levels were detected using the Enzyme Immunoassay Kit (Arbo Assays). To determine cGAMP levels in the bone marrow microenvironment of control and *Prmt9* KD mice, bone marrow fluid was collected by centrifuging tibias and femurs at 8,000 rpm for 15 s; then, cGAMP levels were assessed.

Lucia luciferase reporter assay

WT (catalog no. thpd-nfis, InvivoGen), *cGAS* KO (catalog no. thpd-kocgas, InvivoGen) and *MAVS* KO (catalog no. thpd-komavs, InvivoGen) THP1-Dual cells were used for the reporter assay. The purchased THP1-Dual cells (InvivoGen) were derived from the human THP1 monocyte line harboring the *Lucia* gene. Reporter cells were further engineered with inducible *PRMT9* shRNA or control shRNA. After DOX treatment to *PRMT9* KD or LD2 to inhibit PRMT9 in these cells, *Lucia* luciferase activity was determined as described by the manufacturer (InvivoGen) by adding QUANTI-Luc reagents and read with a FilterMax F5 microplate reader (Molecular Devices).

Immunofluorescence microscopy

Cells were spun onto glass coverslips, fixed and incubated with primary anti-dsDNA (AE-2), γH2AX or S9.6 antibodies, then with secondary antibody. Slides were then mounted in 90% glycerol solution containing DAPI (Thermo Fisher Scientific) and examined under a ZEISS LSM 880 confocal microscope.

Comet assays

We used the OxiSelect Comet Assay Kit (Cell Biolabs). Briefly, after *PRMT9* KD, THP1 cells were mixed with prewarmed (37 °C) Comet agarose at a 1:10 ratio (v/v), then loaded onto the top of the Comet agarose base layer. Slides were immersed for 60 min in lysis buffer at 4 °C, which was washed with prechilled alkaline solution. After three washes with prechilled Tris/Borate/EDTA buffer, slides were subjected to electrophoresis at 1 V cm^{-1} for 15 min, and then rinsed twice with deionized water. Comets were examined under a widefield ZEISS Axio Observer 7 fluorescence microscope. Approximately 50 cells were determined using the OpenComet software in Image J and shown as olive tail moments[74,75].

Gene editing in THP1 cells

THP1 reporter cells were electroporated with ribonucleoprotein complexes consisting of Cas9 protein and sgRNAs in the Neon Transfection System; 20 µmol l^{-1} guide RNA (gRNA) (as listed in Supplementary Table 11) were mixed at a 1:1 ratio. KO efficiency was assessed using immunoblot analysis.

Cocultures of bone marrow DCs and T cells

As described previously[57], bone marrow cells were cultured with complete RPMI medium containing 20 ng ml^{-1} granulocyte-macrophage colony-stimulating factor (PeproTech). Fresh medium was added on days 3 and 6. $CD8^+$ T cells were isolated from the spleens of OT-1 transgenic mice. MA9-OVA cells were pretreated for 2 days with LD2 and then cocultured overnight with collected bone marrow-derived DCs. Supernatants were collected for IFN-β assessment. Bone marrow-derived DCs were selected using a $CD11c^+$ selection kit (STEMCELL Technologies) and cocultured for 48 h with OT-1 $CD8^+$ T cells. IFN-γ supernatants were assayed using a mouse IFN-γ Flex Set Cytometric Bead Array.

MA9 AML model in vivo treatment and assessment of leukemia-specific immunity

Once leukemia cells were engrafted, MA9 syngeneic transplant mice were treated for 3 weeks with vehicle control, LD2, single anti-PD-1 mAb (catalog no. BE0146, Bio X Cell, 10 mg kg^{-1} intraperitoneally every other day) or LD2 plus anti-PD-1 antibody. LD2 was administered at 10 mg kg^{-1} intravenously twice a day, based on the preliminary pharmacokinetic and pharmacodynamic results. Mice were assessed for overall survival or killed directly to assess MA9 cell engraftment in bone marrow and perform staining with survivin-specific pentamers to assess MA9-specific immunity as described elsewhere[44]. Briefly, the bone marrow of MA9 mice was stained with anti-CD8 together with survivin-specific pentamers. CMV-specific pentamers were the negative controls. The percentage of survivin or CMV pentamer-positive CD8 T cells was assessed using flow cytometry. Secondary transplantations were performed to evaluate LSC activity in each group by assessing MA9 cell engraftment in the bone marrow.

Humanized model

The model was established using MHC class I and II DKO *NSG* mice[49]. To do so, we implanted 2 million MNCs from AML specimens intrafemorally into an irradiated DKO *NSG* mouse. After transplantation, MHC-deficient mice showed long-term (approximately 12 weeks in peripheral blood) engraftment of T and $CD33^+$ cells without developing acute graft-versus-host disease. A panel of human lineage and progenitor cell markers (CD45, CD33, CD34, CD14, CD19, CD20, CD3, CD56, HLA-DR) was used to define T cells, B cells, monocytes, DCs and immature $CD33^+CD34^+CD45^{dim}$ cells. Mice were divided into two groups and treated with vehicle or LD2. Three weeks later, the number and frequency of leukemic $CD34^+$ cells and the number of $CD8^+$ T cells expressing CD69 and IFN-γ were assessed.

Non-Hodgkin lymphoma tumor models

A20 cells (3×10^6) were subcutaneously implanted into syngeneic BALB/c mice. When tumor volume reached 100 mm^3, mice were randomized into treatment groups. Tumor-bearing mice were treated with isotype control (vehicle), anti-PD-1 mAb (10 mg kg^{-1} intraperitoneally every other day for 2 weeks), LD2 (100 mg kg^{-1} intratissue injection daily for 2 weeks) or a combination of LD2 with anti-PD-1. Tumor volume was monitored through the end of the study when a humane endpoint was reached. The maximum tumor size (humane endpoint) permitted by the IACUC is 15 mm (diameter). All animals were euthanized before tumor size reached 15 mm in diameter. The microenvironmental components of tumors were analyzed using immunohistochemistry (IHC) and intracellular staining followed by flow cytometry.

IHC

Fixed A20 tumors were embedded in paraffin. Four-micrometer-thick sections on slides were incubated for 1 h at 60 °C, deparaffinized and then rehydrated before IHC staining. Slides were blocked with 3% H_2O_2. Slides were subjected to antigen retrieval for 15 min at 120 °C in citrate buffer, treated with Tris-buffered saline and incubated for 1 h with anti-mouse CD3 or anti-mouse CD8 antibody. After washing, slides were incubated with secondary antibody. Slides were developed and counterstained with Mayer's hematoxylin solution. Slides were scanned using whole slide imaging and analyzed using the NDP.view2 software (Hamamatsu).

Analysis of tumor-infiltrating cells

Portions of fresh A20 tumors were cut into small pieces, then dissociated with type IV collagenase, type IV DNase and type V hyaluronidase at 37 °C for 30 min. Cell suspensions were passed through a 70-µm strainer and centrifuged at 300*g* for 5 min. Cells were stained for 30 min using a Live-or-Dye Fixable Viability Stain Kit (catalog no. 32018, Biotium). Next, cells were stained with immune cell surface markers (mouse CD45-allophycocyanin, mouse CD3-allophycocyanin/cyanine 7, mouse CD4-Alexa Fluor 700 and mouse CD8-Brilliant Violet 605). After two washes, cells were fixed and permeabilized, then intracellularly stained with mouse IFN-γ-phycoerythrin and granzyme B-fluorescein isothiocyanate antibodies in the permeabilization for the flow analysis. Results were analyzed with FlowJo v.10 (FlowJo LLC).

Statistics and reproducibility

Studies involving independent cohorts of mice were typically performed once, with several exceptions stated in the figure legends. No specific statistical tests were applied to determine sample size; size was established according to our previous experience with the models used. Accordingly, we typically used experimental cohorts of 5–7 mice. The experiments were not randomized. Investigators were not blinded to allocation during the experiments and outcome assessments. Data collection and analysis by all investigators were not performed blinded to the conditions of the experiments. No data were excluded from the analyses.

In general, data from independent experiments are shown as the mean ± s.d. or s.e.m. Statistics were determined using an unpaired, two-tailed Student's *t*-test, a two-way ANOVA, a one-way ANOVA and a two-sided Fisher's exact test. Survival results were analyzed with a log-rank (Mantel–Cox) test and expressed as Kaplan–Meier survival curves. Prism (GraphPad Software) was used for the statistics; the detailed methods are described in each individual figure legend.

Reporting summary

Further information on research design is available in the Nature Portfolio Reporting Summary linked to this article.

Data availability

The scRNA-seq and bulk RNA-seq data that support the findings of this study have been deposited in the Gene Expression Omnibus under accession nos. GSE217195 and GSE217396. The PRMT9 SILAC proteomics data have been deposited in PRIDE under accession no. PXD039441. The human cancer PRMT9 expression data were derived from the TCGA Research Network (http://cancergenome.nih.gov/). The dataset derived from this resource that supports the findings of this study is available in the Source data and Supplementary information. A previously published reference dataset of bone marrow samples from newly diagnosed patients with AML and healthy age-matched controls, the BEAT AML dataset, can be found at http://vizome.org/aml/. The TARGET-AML data can be found under accessions nos. GSE14468, GSE12417, GSE63270 and GSE183415. Other published datasets and information are also available at https://DepMap.org/portal/, https://www.cbioportal.org/ (TCGA PanCancer Atlas Studies), https://www.fobinf.com/ (BloodSpot) and GEPIA http://gepia.cancer-pku.cn/ (GEPIA). Source data for all the main figures, extended data figures and supplementary information have been provided as source data files or supplementary files. All other data supporting the findings of this study are available from the corresponding author upon reasonable request. Source data are provided with this paper.

Code availability

No custom code was created. All the packages used in this study are open-source R packages. Briefly, Seurat v.5.0.0 was used for scRNA-seq data quality control, normalization, feature selection, dimension reduction and visualization. Harmony v.1.1.0 was used for batch removal between different scRNA-seq samples. MAST v.1.26.0 was used for the differential gene expression analysis between scRNA-seq UMAP clusters. SingleR v.2.2.0 was used for the scRNA-seq cell type annotations. edgeR v.3.42.4 was used for differential gene expression analyses between bulk RNA-seq samples. In addition, GSEA v.4.0.3 was implemented for all the pathway enrichment work.

References

1. Talati, C. & Sweet, K. L. Nuclear transport inhibition in acute myeloid leukemia: recent advances and future perspectives. *Int. J. Hematol. Oncol.* **7**, IJH04 (2018).
2. Wall, S. A., Devine, S. & Vasu, S. The who, how and why: allogeneic transplant for acute myeloid leukemia in patients older than 60 years. *Blood Rev.* **31**, 362–369 (2017).
3. Pfirrmann, M. et al. Prediction of post-remission survival in acute myeloid leukaemia: a post-hoc analysis of the AML96 trial. *Lancet Oncol.* **13**, 207–214 (2012).
4. Bose, P., Vachhani, P. & Cortes, J. E. Treatment of relapsed/refractory acute myeloid leukemia. *Curr. Treat. Options Oncol.* **18**, 17 (2017).
5. Daver, N., Alotaibi, A. S., Bücklein, V. & Subklewe, M. T cell-based immunotherapy of acute myeloid leukemia: current concepts and future developments. *Leukemia* **35**, 1843–1863 (2021).
6. Kumar, S. et al. CARM1 inhibition enables immunotherapy of resistant tumors by dual action on tumor cells and T cells. *Cancer Discov.* **11**, 2050–2071 (2021).
7. Kwon, J. & Bakhoum, S. F. The cytosolic DNA-sensing cGAS–STING pathway in cancer. *Cancer Discov.* **10**, 26–39 (2020).
8. Zhang, X., Bai, X.-C. & Chen, Z. J. Structures and mechanisms in the cGAS–STING innate immunity pathway. *Immunity* **53**, 43–53 (2020).
9. Chin, E. N. et al. Antitumor activity of a systemic STING-activating non-nucleotide cGAMP mimetic. *Science* **369**, 993–999 (2020).
10. Yang, Y. & Bedford, M. T. Protein arginine methyltransferases and cancer. *Nat. Rev. Cancer* **13**, 37–50 (2013).
11. Nusinow, D. P. et al. Quantitative proteomics of the cancer cell line encyclopedia. *Cell* **180**, 387–402 (2020).
12. Cerami, E. et al. The cBio cancer genomics portal: an open platform for exploring multidimensional cancer genomics data. *Cancer Discov.* **2**, 401–404 (2012).
13. Siegel, R. L., Miller, K. D., Fuchs, H. E. & Jemal, A. Cancer statistics, 2022. *CA Cancer J. Clin.* **72**, 7–33 (2022).
14. Jung, N., Dai, B., Gentles, A. J., Majeti, R. & Feinberg, A. P. An LSC epigenetic signature is largely mutation independent and implicates the *HOXA* cluster in AML pathogenesis. *Nat. Commun.* **6**, 8489 (2015).
15. Somervaille, T. C. P. et al. Hierarchical maintenance of MLL myeloid leukemia stem cells employs a transcriptional program shared with embryonic rather than adult stem cells. *Cell Stem Cell* **4**, 129–140 (2009).
16. Zhou, K.-R. et al. ChIPBase v2.0: decoding transcriptional regulatory networks of non-coding RNAs and protein-coding genes from ChIP–seq data. *Nucleic Acids Res.* **45**, D43–D50 (2017).
17. Cho, E.-C., Mitton, B. & Sakamoto, K. M. CREB and leukemogenesis. *Crit. Rev. Oncog.* **16**, 37–46 (2011).
18. Bagger, F. O., Kinalis, S. & Rapin, N. BloodSpot: a database of healthy and malignant haematopoiesis updated with purified and single cell mRNA sequencing profiles. *Nucleic Acids Res.* **47**, D881–D885 (2019).
19. Dobson, C. L. et al. The *mll–AF9* gene fusion in mice controls myeloproliferation and specifies acute myeloid leukaemogenesis. *EMBO J.* **18**, 3564–3574 (1999).
20. Corral, J. et al. An *Mll–AF9* fusion gene made by homologous recombination causes acute leukemia in chimeric mice: a method to create fusion oncogenes. *Cell* **85**, 853–861 (1996).
21. Chen, W. et al. Malignant transformation initiated by *Mll–AF9*: gene dosage and critical target cells. *Cancer Cell* **13**, 432–440 (2008).
22. Kotani, S. et al. Molecular pathogenesis of disease progression in *MLL*-rearranged AML. *Leukemia* **33**, 612–624 (2019).
23. Papaemmanuil, E. et al. Genomic classification and prognosis in acute myeloid leukemia. *N. Engl. J. Med.* **374**, 2209–2221 (2016).
24. Zhang, L. et al. Targeting miR-126 in inv(16) acute myeloid leukemia inhibits leukemia development and leukemia stem cell maintenance. *Nat. Commun.* **12**, 6154 (2021).
25. Kuo, Y. H. et al. Cbfβ-SMMHC induces distinct abnormal myeloid progenitors able to develop acute myeloid leukemia. *Cancer Cell* **9**, 57–68 (2006).
26. Krivtsov, A. V. et al. Transformation from committed progenitor to leukaemia stem cell initiated by MLL–AF9. *Nature* **442**, 818–822 (2006).
27. Li, Z. et al. Overexpression and knockout of miR-126 both promote leukemogenesis. *Blood* **126**, 2005–2015 (2015).
28. Weng, H. et al. METTL14 inhibits hematopoietic stem/progenitor differentiation and promotes leukemogenesis via mRNA m^{6}A modification. *Cell Stem Cell* **22**, 191–205 (2018).
29. Yang, Y. et al. PRMT9 is a type II methyltransferase that methylates the splicing factor SAP145. *Nat. Commun.* **6**, 6428 (2015).
30. Maddelein, D. et al. The iceLogo web server and SOAP service for determining protein consensus sequences. *Nucleic Acids Res.* **43**, W543–546 (2015).
31. Colaert, N., Helsens, K., Martens, L., Vandekerckhove, J. & Gevaert, K. Improved visualization of protein consensus sequences by iceLogo. *Nat. Methods* **6**, 786–787 (2009).
32. Wang, X. et al. *N*^{6}-methyladenosine modulates messenger RNA translation efficiency. *Cell* **161**, 1388–1399 (2015).
33. Signer, R. A., Magee, J. A., Salic, A. & Morrison, S. J. Haematopoietic stem cells require a highly regulated protein synthesis rate. *Nature* **509**, 49–54 (2014).
34. An, T., Liu, Y., Gourguechon, S., Wang, C. C. & Li, Z. CDK phosphorylation of translation initiation factors couples protein translation with cell-cycle transition. *Cell Rep.* **25**, 3204–3214 (2018).

35. Brook, M. et al. The multifunctional poly(A)-binding protein (PABP) 1 is subject to extensive dynamic post-translational modification, which molecular modelling suggests plays an important role in co-ordinating its activities. *Biochem. J.* **441**, 803–812 (2012).
36. Melo, E. O., Dhalia, R., Martins de Sa, C., Standart, N. & de Melo Neto, O. P. Identification of a C-terminal poly(A)-binding protein (PABP)-PABP interaction domain: role in cooperative binding to poly(A) and efficient cap distal translational repression. *J. Biol. Chem.* **278**, 46357–46368 (2003).
37. Hoshino, S. Mechanism of the initiation of mRNA decay: role of eRF3 family G proteins. *Wiley Interdiscip. Rev. RNA* **3**, 743–757 (2012).
38. Safaee, N. et al. Interdomain allostery promotes assembly of the poly(A) mRNA complex with PABP and eIF4G. *Mol. Cell* **48**, 375–386 (2012).
39. Jafari, R. et al. The cellular thermal shift assay for evaluating drug target interactions in cells. *Nat. Protoc.* **9**, 2100–2122 (2014).
40. Su, R. et al. Targeting FTO suppresses cancer stem cell maintenance and immune evasion. *Cancer Cell* **38**, 79–96 (2020).
41. Li, L. et al. SIRT1 activation by a c-MYC oncogenic network promotes the maintenance and drug resistance of human FLT3-ITD acute myeloid leukemia stem cells. *Cell Stem Cell* **15**, 431–446 (2014).
42. Bhatia, R., McGlave, P. B., Dewald, G. W., Blazar, B. R. & Verfaillie, C. M. Abnormal function of the bone marrow microenvironment in chronic myelogenous leukemia: role of malignant stromal macrophages. *Blood* **85**, 3636–3645 (1995).
43. Liu, Y. et al. Tumors exploit FTO-mediated regulation of glycolytic metabolism to evade immune surveillance. *Cell Metab.* **33**, 1221–1233 (2021).
44. Stroopinsky, D. et al. Leukemia vaccine overcomes limitations of checkpoint blockade by evoking clonal T cell responses in a murine acute myeloid leukemia model. *Haematologica* **106**, 1330–1342 (2021).
45. Barnett, K. C. et al. Phosphoinositide interactions position cGAS at the plasma membrane to ensure efficient distinction between self- and viral DNA. *Cell* **176**, 1432–1446 (2019).
46. Lu, C. et al. DNA sensing in mismatch repair-deficient tumor cells is essential for anti-tumor immunity. *Cancer Cell* **39**, 96–108 (2021).
47. Kim, S., Kim, D., Cho, S. W., Kim, J. & Kim, J.-S. Highly efficient RNA-guided genome editing in human cells via delivery of purified Cas9 ribonucleoproteins. *Genome Res.* **24**, 1012–1019 (2014).
48. Morales, J. C. et al. XRN2 links transcription termination to DNA damage and replication stress. *PLoS Genet.* **12**, e1006107 (2016).
49. Brehm, M. A. et al. Lack of acute xenogeneic graft-versus-host disease, but retention of T cell function following engraftment of human peripheral blood mononuclear cells in NSG mice deficient in MHC class I and II expression. *FASEB J.* **33**, 3137–3151 (2019).
50. Liu, D. et al. Integrative molecular and clinical modeling of clinical outcomes to PD1 blockade in patients with metastatic melanoma. *Nat. Med.* **25**, 1916–1927 (2019).
51. Mariathasan, S. et al. TGFβ attenuates tumour response to PD-L1 blockade by contributing to exclusion of T cells. *Nature* **554**, 544–548 (2018).
52. Hadjikyriacou, A., Yang, Y., Espejo, A., Bedford, M. T. & Clarke, S. G. Unique features of human protein arginine methyltransferase 9 (PRMT9) and its substrate RNA splicing factor SF3B2. *J. Biol. Chem.* **290**, 16723–16743 (2015).
53. Reilly, A. et al. Immunologic consequences of chemotherapy for acute myeloid leukemia. *J. Pediatr. Hematol. Oncol.* **35**, 46–53 (2013).
54. Vago, L. & Gojo, I. Immune escape and immunotherapy of acute myeloid leukemia. *J. Clin. Investig.* **130**, 1552–1564 (2020).
55. Das, R. K., O'Connor, R. S., Grupp, S. A. & Barrett, D. M. Lingering effects of chemotherapy on mature T cells impair proliferation. *Blood Adv.* **4**, 4653–4664 (2020).
56. Maelfait, J., Bridgeman, A., Benlahrech, A., Cursi, C. & Rehwinkel, J. Restriction by SAMHD1 limits cGAS/STING-dependent innate and adaptive immune responses to HIV-1. *Cell Rep.* **16**, 1492–1501 (2016).
57. Mender, I. et al. Telomere stress potentiates STING-dependent anti-tumor immunity. *Cancer Cell* **38**, 400–411 (2020).
58. Sun, J. et al. SIRT1 activation disrupts maintenance of myelodysplastic syndrome stem and progenitor cells by restoring TET2 function. *Cell Stem Cell* **23**, 355–369 (2018).
59. He, X. et al. PRMT1-mediated FLT3 arginine methylation promotes maintenance of FLT3-ITD$^+$ acute myeloid leukemia. *Blood* **134**, 548–560 (2019).
60. Wunderlich, M. et al. AML cells are differentially sensitive to chemotherapy treatment in a human xenograft model. *Blood* **121**, e90–e97 (2013).
61. Li, L. et al. Activation of p53 by SIRT1 inhibition enhances elimination of CML leukemia stem cells in combination with imatinib. *Cancer Cell* **21**, 266–281 (2012).
62. Musiani, D. et al. Proteomics profiling of arginine methylation defines PRMT5 substrate specificity. *Sci. Signal.* **12**, eaat8388 (2019).
63. Eberhardt, J., Santos-Martins, D., Tillack, A. F. & Forli, S. AutoDock Vina 1.2.0: new docking methods, expanded force field, and Python bindings. *J. Chem. Inf. Model.* **61**, 3891–3898 (2021).
64. Trott, O. & Olson, A. J. AutoDock Vina: improving the speed and accuracy of docking with a new scoring function, efficient optimization, and multithreading. *J. Comput. Chem.* **31**, 455–461 (2010).
65. Mayer, M. & Meyer, B. Group epitope mapping by saturation transfer difference NMR to identify segments of a ligand in direct contact with a protein receptor. *J. Am. Chem. Soc.* **123**, 6108–6117 (2001).
66. Aguilar, J. A., Nilsson, M., Bodenhausen, G. & Morris, G. A. Spin echo NMR spectra without J modulation. *Chem. Commun.* **48**, 811–813 (2012).
67. Jiang, P. et al. Signatures of T cell dysfunction and exclusion predict cancer immunotherapy response. *Nat. Med.* **24**, 1550–1558 (2018).
68. Hao, Y. et al. Integrated analysis of multimodal single-cell data. *Cell* **184**, 3573–3587 (2021).
69. Zhang, H. et al. CDK7 inhibition potentiates genome instability triggering anti-tumor immunity in small cell lung cancer. *Cancer Cell* **37**, 37–54 (2020).
70. Aran, D. et al. Reference-based analysis of lung single-cell sequencing reveals a transitional profibrotic macrophage. *Nat. Immunol.* **20**, 163–172 (2019).
71. Ma, Y. et al. Integrative differential expression and gene set enrichment analysis using summary statistics for scRNA-seq studies. *Nat. Commun.* **11**, 1585 (2020).
72. Li, J. et al. Metastasis and immune evasion from extracellular cGAMP hydrolysis. *Cancer Discov.* **11**, 1212–1227 (2021).
73. Yu, C.-H. et al. TDP-43 triggers mitochondrial DNA release via mPTP to activate cGAS/STING in ALS. *Cell* **183**, 636–649 (2020).
74. Gyori, B. M., Venkatachalam, G., Thiagarajan, P. S., Hsu, D. & Clement, M.-V. OpenComet: an automated tool for comet assay image analysis. *Redox Biol.* **2**, 457–465 (2014).
75. Kumaravel, T. S., Vilhar, B., Faux, S. P. & Jha, A. N. Comet Assay measurements: a perspective. *Cell Biol. Toxicol.* **25**, 53–64 (2009).
76. Zhong, Z. A. et al. Inactivation of the progesterone receptor in Mx1$^+$ cells potentiates osteogenesis in calvaria but not in long bone. *PLoS ONE* **10**, e0139490 (2015).
77. Shannon, P. et al. Cytoscape: a software environment for integrated models of biomolecular interaction networks. *Genome Res.* **13**, 2498–2504 (2003).

Acknowledgements

We thank the COH Comprehensive Cancer Center, and the patients, donors and their physicians for providing primary specimens for this study. This work was supported in part by National Institutes of Health grant nos. R01 HL141336, R01 CA248149, R01 CA279595 and ACS

RSG-19-036001-LIB; the When Everyone Survives Leukemia Research Award; the Tower Cancer Research Foundation Scientific Innovations Award for Senior Investigator the St. Baldrick's Foundation Research Grant Award the Alex's Lemonade Stand Foundation R Accelerated Award; the Vera and Joseph Dresner Foundation Established Investigator Award and the CURE Childhood Cancer Award, all to L. Li, who was also supported by the Gehr Family Center for Leukemia Research. We thank J. Yu and M. Kortylewski (both from City of Hope Medical Center) for providing the *OT-I* mice; Y. Fu (UT Southwestern Medical Center) for providing the A20 cell line; E. Wang (City of Hope Medical Center) for providing the A549 and SW1573 cell lines; R. Salgia and A. Mohanty (both from City of Hope Medical Center) for providing the DMS273 and DMS114 cell lines; and S. Priceman (City of Hope Medical Center) for providing the PC3 and DU145 cell lines. The MA9.6ITD cells (*MLL-AF9* plus *FLT3-ITD*) were established by J. Molley (Cincinnati Children's Hospital Medical Center). We thank Y. Yang (City of Hope Medical Center) for providing the pcDNA3.1-myc-PRMT9 plasmid. We also acknowledge the Animal Resources Center, the Analytical Cytometry Core, Bioinformatics, Light Microscopy, the Integrative Genomics Core, Pathology (Hematopoietic Tissue Biorepository), Integrated Mass Spectrometry, all shared resources from the COHCCC, in part by the NIH/NCI Award no. P30CA33572. We also thank E. Lamar for editing and proofreading. The content of the paper is solely the responsibility of the authors and does not necessarily represent official views of the NIH. The funders had no role in study design, data collection and analysis, decision to publish or preparation of the paper.

Author contributions

H.D. designed and performed the experiments, interpreted the results and wrote the paper. X.H. performed the experiments, including the immunofluorescence and CRISPR–Cas9 experiments, and reviewed the paper. L.Z. assisted with the animal experiments, immunoblots and reviewed the paper. W.C. performed the bioinformatic data mining, RNA-seq and scRNA-seq data analysis. Y.-C.L. performed the compound docking and virtual screen. S.-B.L. designed the animal experiments and performed the data analysis. H.W. collected the clinical sample, performed the qPCR detection and carried out the overall survival analysis. L.X.T.N. performed the lentivirus, retrovirus packaging and transduction, and the animal experiments. M.L. performed the statistical analysis. Y.Z. performed the quantitative MS analyses. D.Z. assisted with the animal experiments. R. Sharma performed the LC–tandem MS data acquisition and analysis and drafted the Methods. P.P. reviewed the SILAC quantitative proteomics analysis and the paper. X.W. reviewed the RNA-seq results. W. Hu performed the NMR experiments. J.W. performed the compound experiments. R. Su provided the mouse and human AML cell lines. J.S., B.V., L. Luznik and I.G. performed the bioinformatics analysis. J.Z., L.G., A.S., J.C., W. Han, B.S., Y.-H.K., J. J., G.M. and Y. Luo reviewed and edited the paper. L. Li designed the study, explained the data and wrote and revised the paper with input from the other authors.

Competing interests

The authors declare no competing interests.

Additional information

Extended data is available for this paper at https://doi.org/10.1038/s43018-024-00736-x.

Supplementary information The online version contains supplementary material available at https://doi.org/10.1038/s43018-024-00736-x.

Correspondence and requests for materials should be addressed to Ling Li.

Peer review information *Nature Cancer* thanks Raffaella Di Micco and the other, anonymous, reviewer(s) for their contribution to the peer review of this work.

Reprints and permissions information is available at www.nature.com/reprints.

---

[1]Department of Hematological Malignancies Translational Science, Gehr Family Center for Leukemia Research, Hematologic Malignancies and Stem Cell Transplantation Institute, Beckman Research Institute, City of Hope Medical Center, Duarte, CA, USA. [2]Integrative Genomics Core, Beckman Research Institute, City of Hope Medical Center, Duarte, CA, USA. [3]Department of Pharmaceutical Sciences, College of Pharmacy, Western University of Health Sciences, Pomona, CA, USA. [4]Suzhou Key Laboratory of Medical Biotechnology, Suzhou Vocational Health College, Suzhou, People's Republic of China. [5]Department of Hematology, the First Affiliated Hospital, Zhejiang University School of Medicine, Hangzhou, People's Republic of China. [6]Division of Biostatistics, Department of Computational and Quantitative Medicine, Beckman Research Institute, City of Hope Medical Center, Duarte, CA, USA. [7]Department of Medicine, Division of Hematology, Lineberger Comprehensive Cancer Center, University of North Carolina, Chapel Hill, NC, USA. [8]Department of Microbiology and Immunology and Department of Pathology and Laboratory Medicine, University of North Carolina School of Medicine, Chapel Hill, NC, USA. [9]Department of Microbiology and Immunology, Computational Medicine Program, Lineberger Comprehensive Cancer Center, University of North Carolina, Chapel Hill, NC, USA. [10]Department of Oncology and Sidney Kimmel Comprehensive Cancer Center, The Johns Hopkins University School of Medicine, Baltimore, MD, USA. [11]Department of Systems Biology, Beckman Research Institute, City of Hope Medical Center, Duarte, CA, USA. [12]Cancer & Cell Biology Division, The Translational Genomics Research Institute, Phoenix, AZ, USA. [13]Integrated Mass Spectrometry Shared Resource, City of Hope Medical Center, Duarte, CA, USA. [14]Department of Computational and Quantitative Medicine, Beckman Research Institute, City of Hope Medical Center, Duarte, CA, USA. [15]Department of Immunology and Theranostics, Beckman Research Institute, City of Hope Medical Center, Duarte, CA, USA. [16]Sir Run Run Shaw Hospital, Zhejiang University, Hangzhou, People's Republic of China. [17]Department of Cancer Genetics and Epigenetics, Beckman Research Institute, City of Hope Medical Center, Duarte, CA, USA. [18]Department of Hematology and HCT, City of Hope Medical Center, Duarte, CA, USA. [19]Department of Pediatrics, Beckman Research Institute, City of Hope Medical Center, Duarte, CA, USA. [20]These authors contributed equally: Haojie Dong, Xin He, Lei Zhang. ✉e-mail: lingli@coh.org

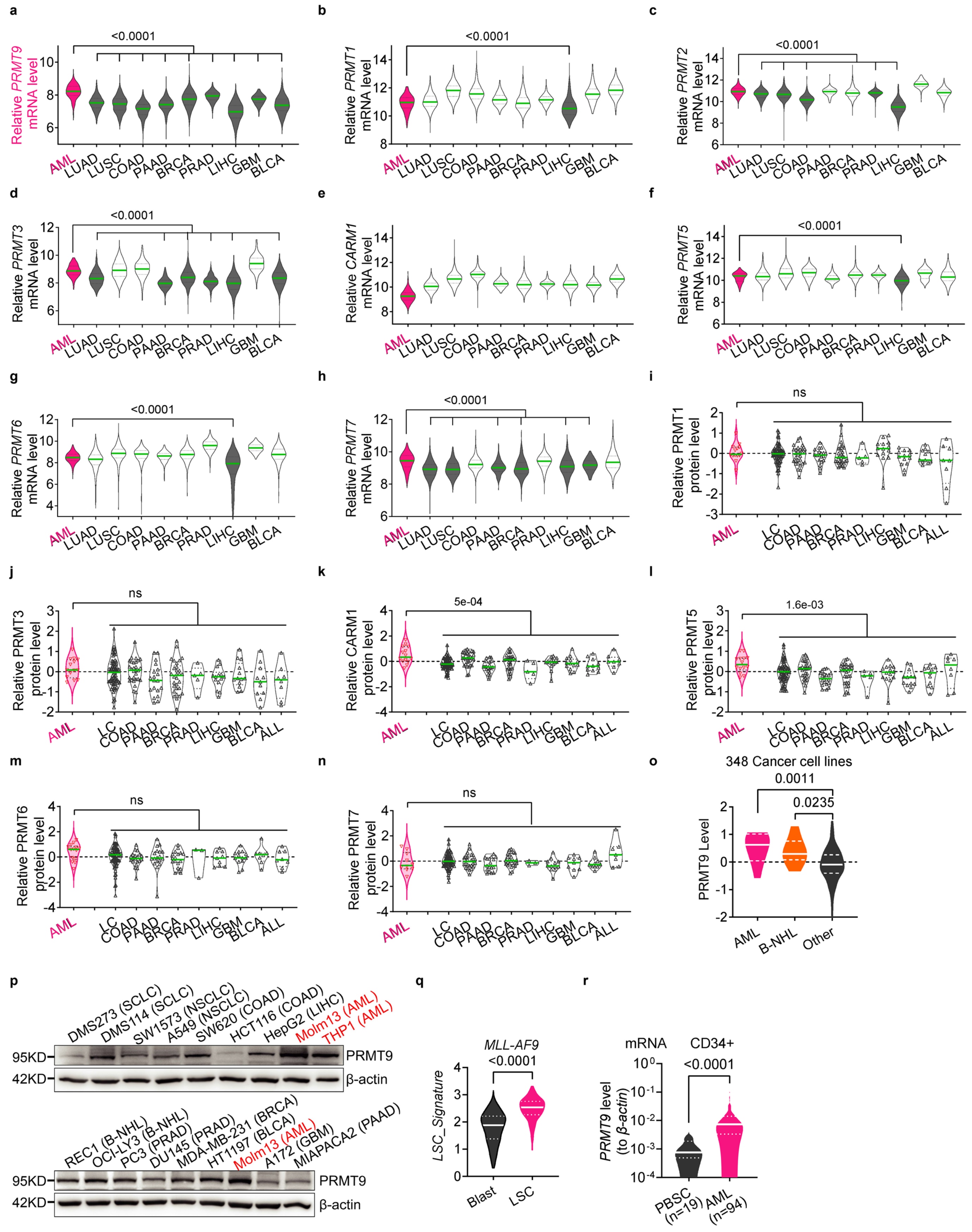

Extended Data Fig. 1 | See next page for caption.

Extended Data Fig. 1 | PRMT9 levels are elevated in AML. a–h, PRMTs mRNA levels in cancers from TCGA PanCancer Atlas. AML (n = 173), Lung adenocarcinoma (LUAD, n = 510), Lung squamous cell carcinoma (LUSC, n = 484), Colon Adenocarcinoma (COAD, n = 438), Pancreatic adenocarcinoma (PAAD, n = 177), Breast Cancer (BRCA, n = 1082), Prostate adenocarcinoma (PRAD, n = 493), Liver Hepatocellular Carcinoma (LIHC, n = 366), Glioblastoma (GBM, n = 160), Bladder Carcinoma (BLCA, n = 407). PRMT expression in AML (red) was compared with other cancers (only with significant difference were indicated). The violin plot in gray indicates PRMTs (except PRMT8 which is undetectable) level was significantly higher in AML than indicated cancer type. P values (a-h) were determined by unpaired two-sided t-tests. 'n' represents the number of patients. **i**–**n**, PRMTs protein levels in AML lines relative to those seen in lines representing the other deadly cancers. AML (n = 14), Lung Cancer (LC, n = 77), COAD (n = 29), PAAD (n = 17), BRCA (n = 29), PRAD (n = 5), LIHC (n = 12), GBM (n = 11), BLCA (n = 9) and Acute Lymphoblastic Leukemia (ALL, n = 8). Data was based on DepMap. P values were determined by unpaired two-sided t test. 'n' represents number of cancer cell lines. **o**, PRMT9 levels in AML (n = 10) and B-NHL (n = 8) lines relative to lines from other deadly cancers (n = 330), based on DepMap. P values were determined by one-way ANOVA. 'n' represents number of cell lines. **p**, PRMT9 protein levels in lines from most-deadly cancers, (n = 1). **q**, Expression level of LSC-signature-genes in LSC (n = 383 cells) and Blast (n = 1191 cells) based on MA9 scRNAseq analyses. P value was determined by unpaired two-sided t test. **r**, Q-PCR analysis of PRMT9 levels in AML CD34+ cells from an in-house cohort (n = 94 patients) and from PBSCs from healthy donors (n = 19). PRMT9 levels were normalized to β-actin. P value was determined by unpaired two-sided t test.

https://doi.org/10.1038/s43018-024-00736-x

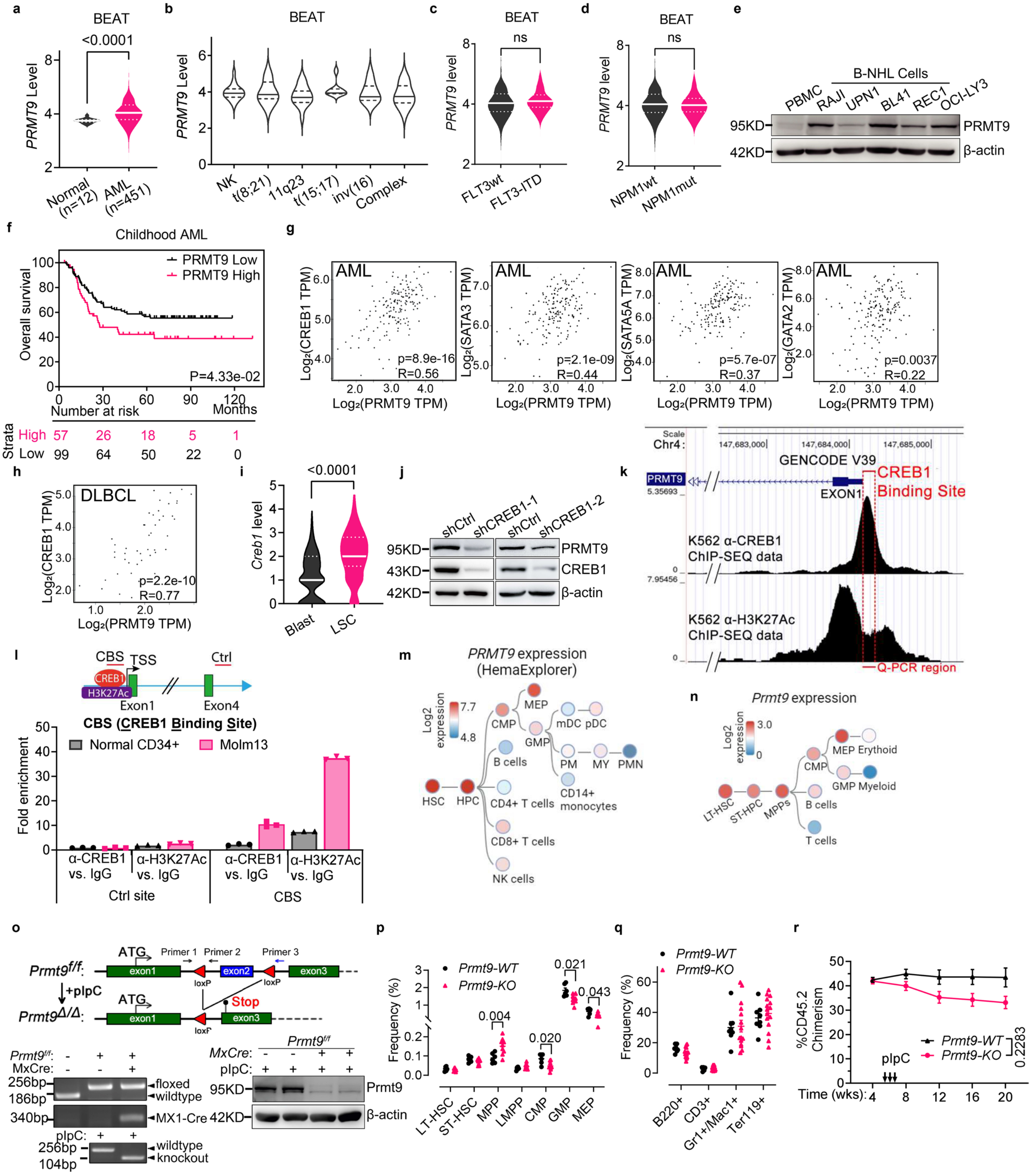

Extended Data Fig. 2 | See next page for caption.

Extended Data Fig. 2 | PRMT9 function is dispensable for normal hematopoiesis. a, *PRMT9* mRNA levels from BEAT AML dataset of mononuclear cells (MNCs) from AML cases (n = 451 patients) and healthy donors (n = 12). P value was determined by unpaired two-sided t test. **b**, *PRMT9* levels in AML cases with different cytogenetic karyotypes from BEAT AML. NK: n = 107, t (8;21): n = 11, 11q23: n = 15, t (15;17): n = 15, inv (16): n = 25, Complex: n = 32. 'n' represents the number of patients. **c, d**, *PRMT9* levels in BEAT AML of FLT3-ITD (c) and NPM1 (d) mutated subsets relative to their WT counterparts. FLT3wt n = 346, FLT3-ITD: n = 105; NPM1wt: n = 340, NPM1mut: n = 108. P value was determined by unpaired two-sided Mann–Whitneyt test. 'n' represents the number of patients. **e**, PRMT9 protein levels in B-NHL lines relative to PBMC control, (n = 1). **f**, Kaplan-Meier survival analysis of a cohort (TARGET-AML) after dichotomization for *PRMT9* levels below (green, n = 99) or above (red, n = 57) 3.55 log2-transformed intensity. The threshold is discovered via Partitioning Around Medoids (PAM). P value was determined by log-rank (Mantel–Cox) test. 'n' represents number of patients. **g, h**, Pearson's correlation coefficient of *CREB1*, *STAT3*, *STAT5A*, and *GATA2* with *PRMT9* levels across TCGA AML cohort (g). Correlation of *CREB1* with *PRMT9* levels across TCGA DLBCL cohort (h). Statistics were determined by pairwise gene correlation analysis as described by GEPIA. Data was sourced from GEPIA. **i**, Expression level of *Creb1* in LSC (n = 383 cells) and Blast (n = 1444 cells) based on MA9 AML scRNAseq analyses. P value was determined by unpaired two-sided t test. **j**, PRMT9 levels after *CREB1* KD. n = 1. **k**, Anti-CREB1 and anti-H3K27Ac ChIP-seq analysis in Molm13. **l**, Upper panel, diagram showing predicted CREB1 binding sites on TSS site in the *PRMT9* promoter. Red bars indicate regions representing CBS (CREB1 Binding Site) and Ctrl sites after ChIP assay. Lower panel, one representative result of ChIP-qPCR analysis of enrichment of CREB1 and H3K27Ac at the CBS site and at a distal control site in Molm13 and normal PBSC CD34+ cells. Similar results were generated from three independent experiments. **m, n**, *PRMT9* mRNA levels in human (m) or murine (n) hematopoietic subset as indicated. Human HSCs are from GSE17054; GMP and MEP cells are from GSE11864; monocytes are from GSE11864 and E-MEXP-1242. Muirne *Prmt9* levels were normalized to Myeloid (Gr1+Mac1+) *Prmt9* mRNA levels and log2-transformed. Data was sourced from Bloodspot. **o**, Schema of the *Prmt9* targeting strategy. The lower left panel shows representative genotyping results of *Prmt9* wt, floxed and KO alleles. Lower right panel, Prmt9 protein levels in BM cells from Prmt9 WT and KO mice. **p**–**q**, Frequency of hematopoietic progenitors (p) and mature lineage cells (q) in mouse BM at 16 weeks after pIpC administration. (p), *Prmt9* WT (n = 6), *Prmt9* KO (n = 9); (q), *Prmt9* WT (n = 8), *Prmt9* KO (n = 15). 'n' represents mice number in each group. Data were presented as mean ± SEM. P values were determined by unpaired two-sided t test. **r**, Competitive transplantation of CD45.2 *Prmt9* KO BM cells with normal CD45.1 BM cells in recipient mice, n = 7 mice/group. The percentage of CD45.2 in PB was assessed. Results represent the mean ± SEM. P was determined by two-way ANOVA.

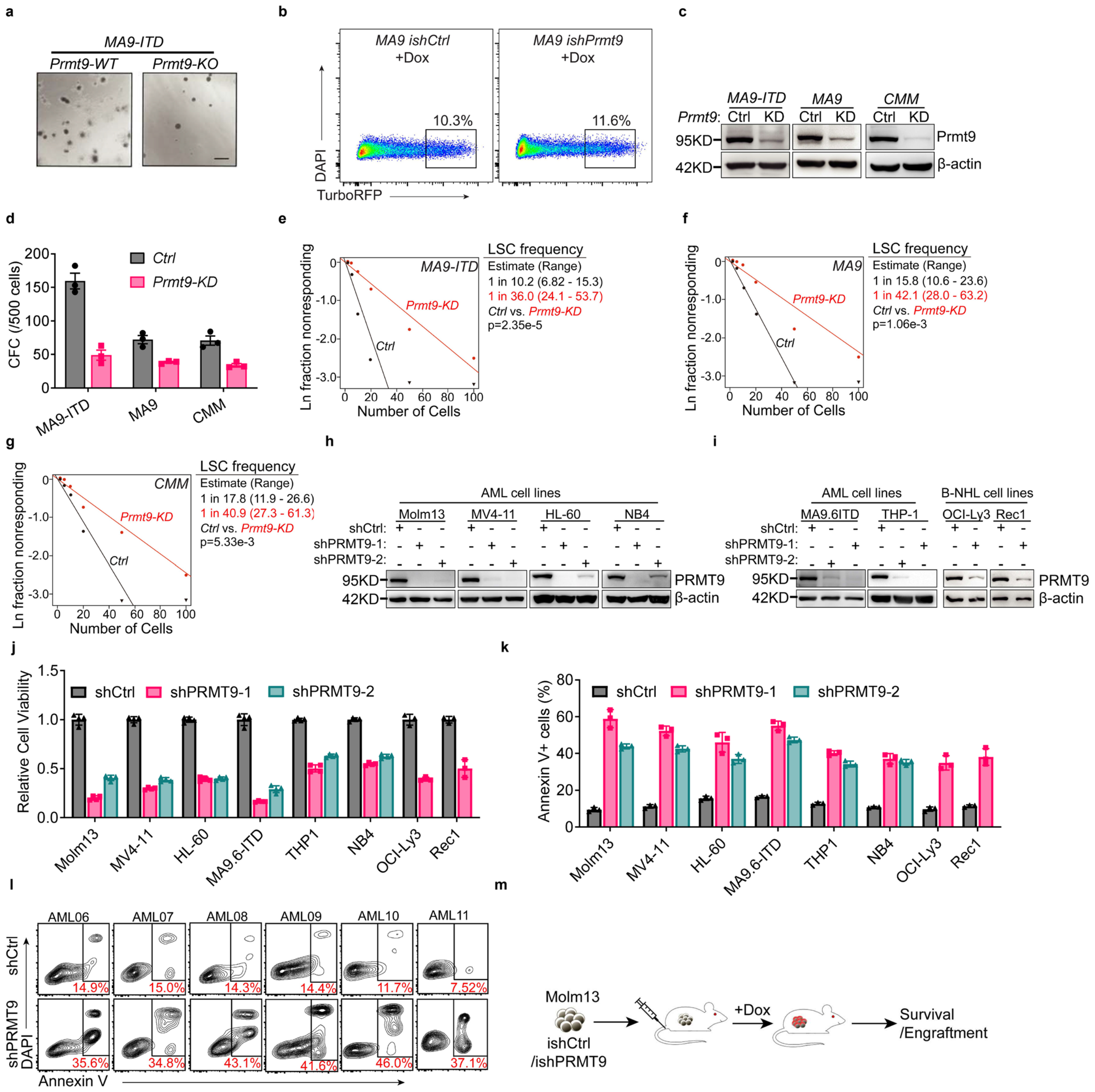

Extended Data Fig. 3 | PRMT9 ablation impairs cancer cell survival. **a**, Representative image of colonies in MA9-ITD cells (n = 5 biological replicates). Scale bar: 1000 µm. **b**, Representative plots show the gating for MA9 cells transduced with Dox-inducible shCtrl and shPrmt9. **c, d**, *Prmt9* KD efficiency in indicated cells, were shown (c). CFC of indicated cells after *Prmt9* KD (d). Results represent the mean ± SD from 3 independent experiments. **e**–**g**, *in vitro* limiting dilution assay (LDA) assay to evaluate the LSC frequency in *Prmt9* KD engineered MA9/FLT3-ITD+ (e), MA9 (f) and CMM (g) AML cells. LSC frequency and p value were calculated using Extreme Limiting Dilution Analysis (ELDA). LSC frequencies are presented as mean ± 95% confidence interval are shown; ELDA were used to analyze χ2 test with 1 degree of freedom. **h**–**k**, Cancer lines as indicated were transduced with shPRMT9 to KD endogenous *PRMT9*. Cell viability (j) by an MTS assay. Apoptosis (k) by Annexin V staining. PRMT9 expression levels were detected (h, i). Results (j, k) represent the mean ± SD from at least 3 (J, n = 4; K, n = 3) independent experiments. **l**, Primary AML CD34+ cells were transduced with shPRMT9-1 and analyzed for apoptosis as above. **m**, Schema of PRMT9 inducible KD Molm13 xenografted in *NSG* mice. Briefly, Molm13 cells were transduced with a DOX-inducible shPRMT9 or control vector and transplanted into mice. Once engraftment was confirmed (>1% in PB), mice were treated with DOX to induce *PRMT9* KD. At endpoint, engraftment was evaluated based on percentage of hCD45 cells in BM. In parallel analysis, mouse survival was analyzed.

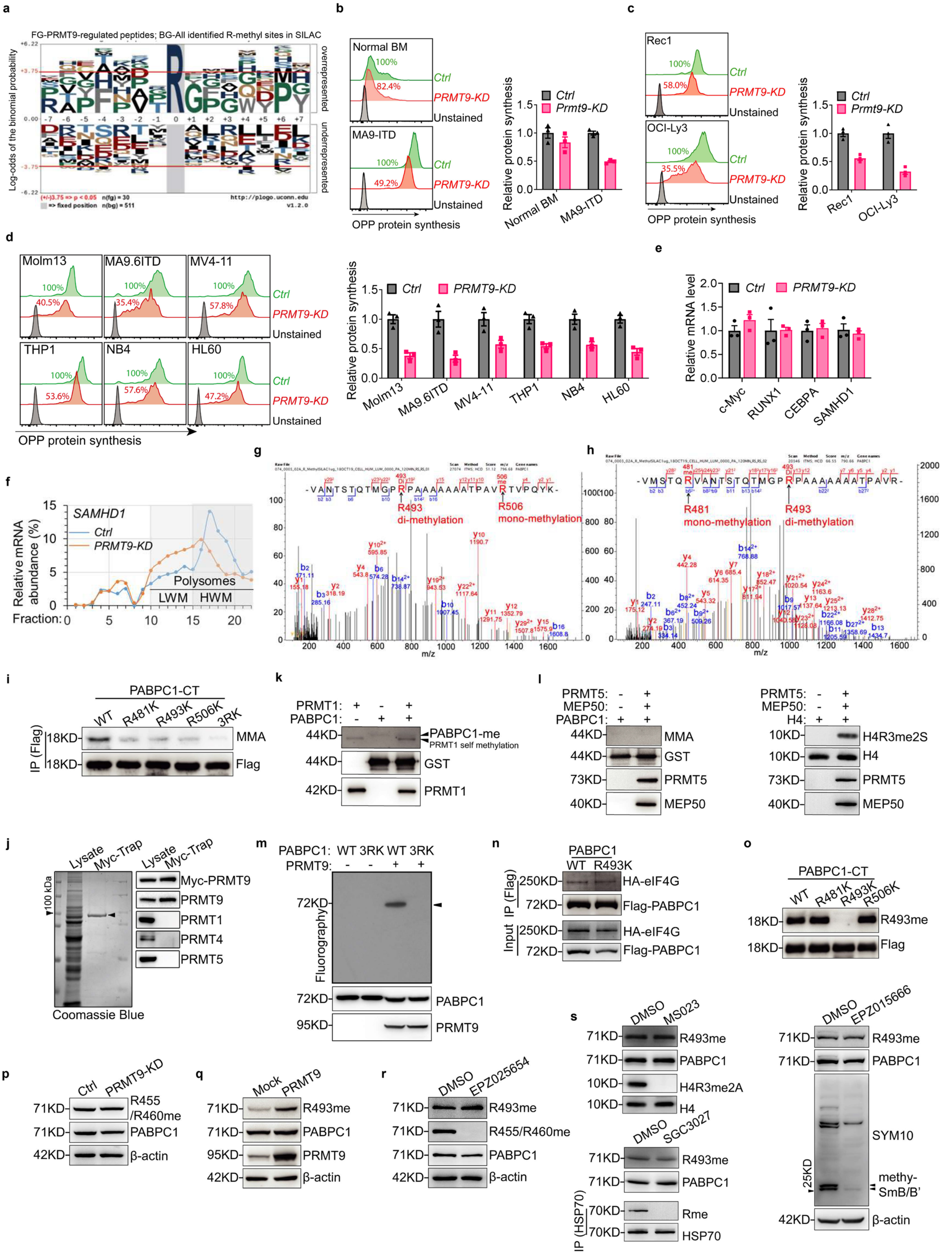

Extended Data Fig. 4 | See next page for caption.

Extended Data Fig. 4 | PRMT9-mediated methylation promotes cancer cell growth. a, iceLogo motif analysis of R-methyl peptides regulated by PRMT9. **b**–**d**, Protein synthesis in normal BM cKit + , MA9-ITD cells (b), B-NHL (Rec1 and OCI-Ly3) (c) and indicated AML lines (d) with shCtrl or shPRMT9. The right panel of (b-d) summarizes the results (n = 3 independent experiments). Data were mean ± SD. **e**, Indicated gene levels in Molm13 (n = 3 independent experiments). Data were mean ± SD. **f**, SAMHD1 levels in RNAs extracted from indicated fractions in a ribosome profiling assay. **g, h**, Spectra of R493, R506 and R481 methylation in LC-MS/MS. **i**, 293 T were transfected with Flag-tagged PABPC1-CT, then subjected to immunoprecipitation and immunoblot (n = 2 independent experiments). **j**, Purification of Myc-tagged PRMT9 by the Myc-Trap. Purity-check with indicated PRMTs antibodies, (n = 1). **k**, In vitro methylation assay of GST-tagged PABPC1-CT mixed with PRMT1 protein, SAM, then analyzed by immunoblot (n = 2 independent experiments). **l**, In vitro methylation assay of GST-tagged PABPC1-CT mixed with PRMT5/MEP50, SAM, then analyzed by immunoblot (n = 2 independent experiments). **m**, Ex-vivo tritium methylation assay using PABPC1-WT and -3RK (R481K/R493K/R506K) immunoprecipitated from 293 T (n = 2 independent experiments). **n**, 293 T were co-transfected with HA-tagged eIF4G plus Flag-tagged PABPC1, then subjected to pull-down and immunoblot (n = 1). **o**, 293 T were transfected with Flag-tagged PABPC1-CT, then subjected to pull-down and immunblot (n = 2 independent experiments). **p**, PABPC1 R455/R460 methylation, after *PRMT9* KD in Molm13 (n = 2 independent experiments). **q**, PABPC1 R493 methylation, after PRMT9 overexpression in Molm13 (n = 2 independent experiments). **r**, PABPC1 methylation, in Molm13 treated with EPZ056544 at 5 µM for 48 hr (n = 2 independent experiments). **s**, PABPC1 R493 methylation, in Molm13 cells treated with PRMT1i (MS023, 5 µM, 48 hr), PRMT5i (EPZ015666, 5 µM, 96 hr) or PRMT7i (SGC3027, 5 µM, 48 hr). H4R3me2A, HSP70me (IP HSP70 and detected with anti-MMA antibody), SDMA (SYM10 antibody) were positive controls for MS023, SGC3027, and EPZ015666 respectively (n = 2 independent experiments).

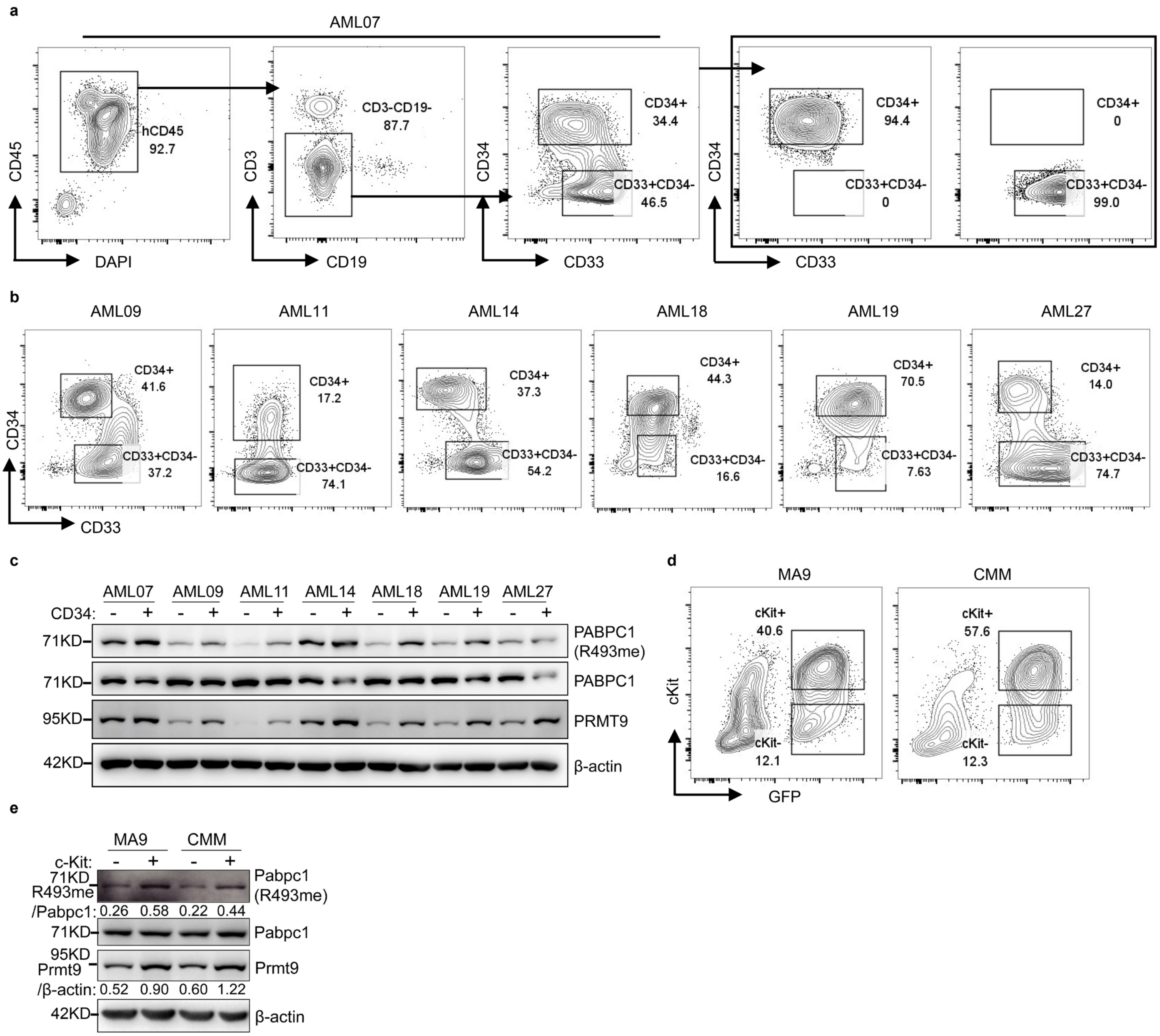

Extended Data Fig. 5 | PRMT9 expression is correlated with R493 methylation. a, representative gating strategy of human AML sample excluding T cells and B cells, and sorting CD34+ subset and CD34-CD33+ leukemia blasts (Blasts). After sorting, the purity of LSC and Blast cells were checked again. **b**, Sorting strategy of six primary AML samples for the LSC and Blasts (n = 6 samples). **c**, PABPC1 R493me, PRMT9 levels in CD34+ subset and Blasts (n = 7 patient samples). **d**, Sorting strategy of cKit+ and cKit- indicated leukemia cells from BM of AML developed mice. **e**, Levels of PABPC1 R493me, Prmt9 in cKit+ and cKit- leukemia cells as indicated (n = 3 independent experiments).

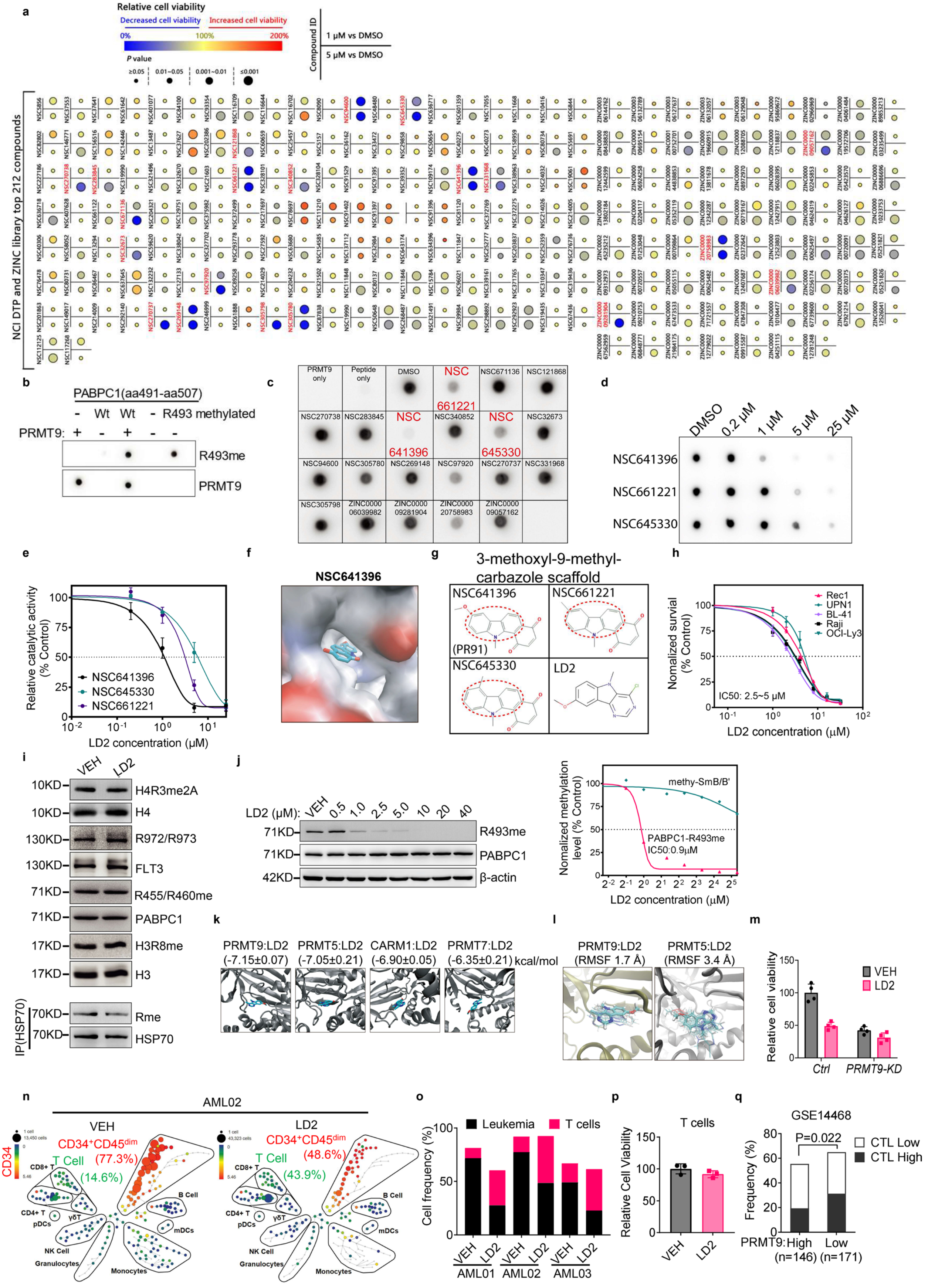

Extended Data Fig. 6 | See next page for caption.

Extended Data Fig. 6 | Identification of a PRMT9 inhibitor. **a**, Effects of hits (142 from NCI-DTP and 70 from ZINC library) on Molm13 viability. Cells were treated for 4 days with 1 or 5 µM compounds. For each compound, the number represents its library ID. Experiments were triplicated; P values were derived from t tests. **b**, R493 methylation assay. PABPC1 peptides (G491-T507) were incubated with PRMT9, and SAM. Catalytic activity was assessed by anti-R493 antibody. Synthesized R493me peptide as positive control. **c**, Catalysis screen of top 20 compounds. PRMT9 protein was pretreated with indicated compound (10 µM), then incubated with PABPC1 peptides and SAM. **d, e**, Catalytic activity of indicated compounds based on R493 methylation assay (d). Inhibition curves were calculated based on intensity of dots and normalized to DMSO (e). Data is mean ± SD (n = 3 independent experiments). **f, g**, NSC641396, NSC661221 and NSC645330 share a carbazole ring scaffold. LD2 is designed based on NSC641396 (g). Docking model of NSC641396 in the catalytic pocket (f). **h**, IC50 analysis of LD2 in B-NHL lines. Cells were treated for 4 days with LD2. Data were mean ± SD (n = 6 independent experiments). **i**, Substrates of PRMT1 (H4R3me2A, FLT3 R972/R973me), CARM1 (PABPC1 R455/R460me), PRMT5 (H3R8me2S), PRMT7 (HSP70me) were assessed in Molm13 treated 2 days with 2.5 µM LD2 (n = 2 independent experiments). **j**, Dose-dependent inhibition of PABPC1 R493 methylation level after 2 days of treatment with LD2 in Molm13 cells (n = 1). Cells were treated with a dose titration of 0.5–40 µM LD2 for 48 hr. The inhibition activity of LD2 to PRMT9 (right red curve) was evaluated by calculating the normalized PABPC1 R493 methylation signal. The inhibition activity of LD2 to PRMT5 (right blue curve) was evaluated by calculating the normalized SmB'B' methylation signal (supplementary Fig. 2). **k**, Vina docking of LD2 with PRMT9, PRMT5, CARM1 or PRMT7 was performed, and the average docking scores (kcal/mol, with standard deviation) were shown. **l**, Molecular dynamics simulation analyses of LD2 with PRMT9 or PRMT5. Smaller root-mean-square-fluctuation (RMSF) of ligand (LD2) in the binding pocket of PRMT9 compared with PRMT5 was shown. **m**, Ctrl and *PRMT9* KD Molm13 were treated for 4 days with LD2 (2.5 uM), and viability was assessed. Data were mean ± SD from 4 independent experiments. **n**, CyTOF of AML MNCs after treatment for 4 days with vehicle or LD2 (2.5 µM). The frequency of CD3 + T cells and CD34+CD45dim AML blasts was noted. **o**, Relative leukemia (CD34+CD45dim) and T cell frequencies before and after LD2 treatment based on CyTOF from 3 samples. **p**, Enriched T cells were treated for 4 days with LD2 (2.5 µM) for 4 days, and cell viability was assessed (n = 3 independent experiments). Data were mean ± SD. **q**, Frequency of PRMT9 high versus low AML samples displaying the Cytotoxic T Lymphocyte (CTL) score high versus low signatures in cohort GSE14468. P value was calculated using two-sided Fisher exact chi-squared test. 'n' represents number of patients.

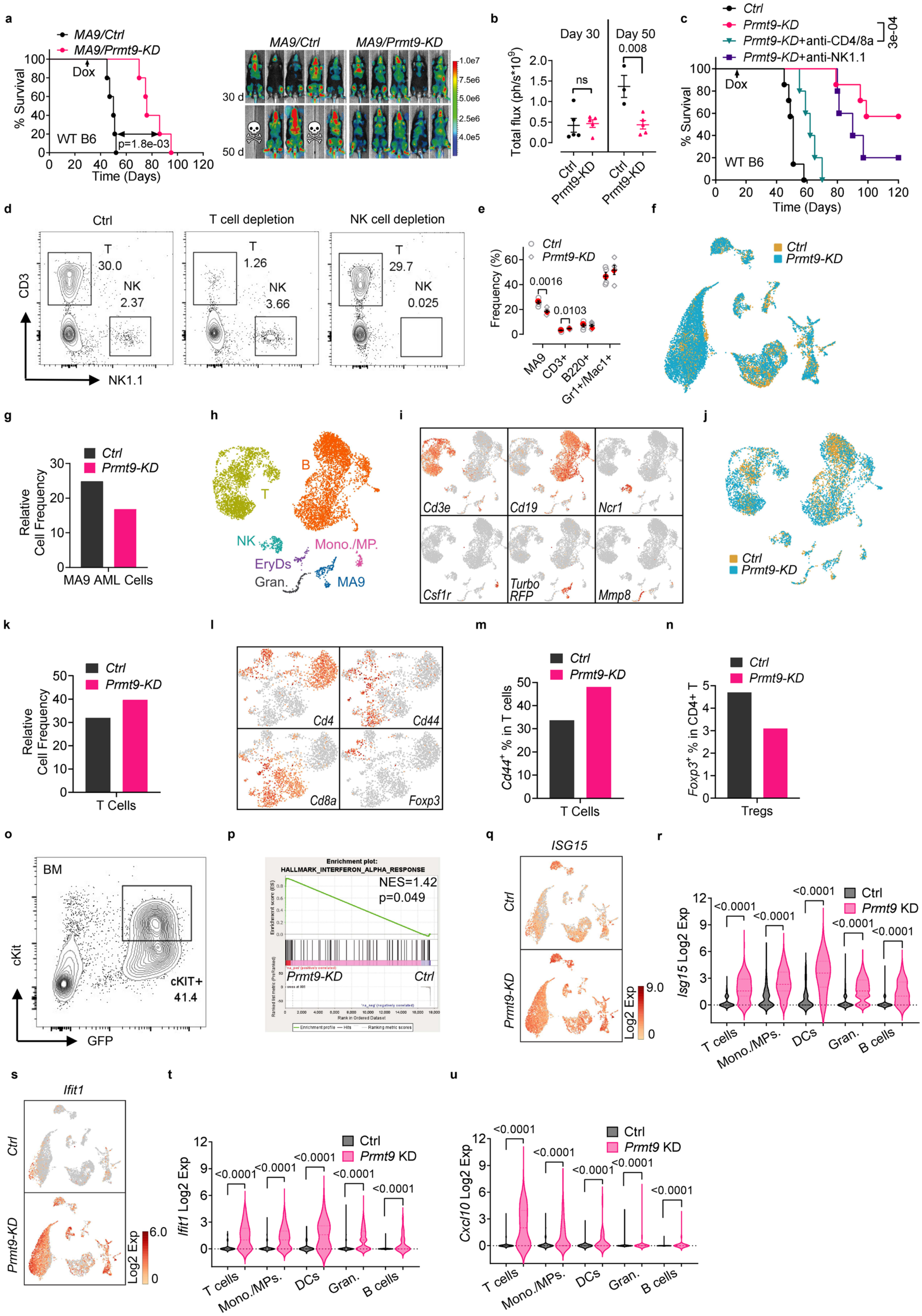

Extended Data Fig. 7 | See next page for caption.

Extended Data Fig. 7 | PRMT9 inhibition eradicates AML in vivo. a, Control or inducible *Prmt9* KD MA9-luciferase cells were injected into wild-type B6 (1×10^6 cells per mouse, n = 5/group). After 30 days when leukemia robustly developed, mice were continuously administered with Dox. Kaplan-Meier curves show survival. P value was determined by log-rank (Mantel–Cox) test. **b**, MA9 AML burden was assessed by bioluminescence imaging over indicated days and the statistics for the quantitative results on day 30 and day 50 from bioluminescence imaging were shown, n = 5 mice/group. Data are presented as mean ± SEM. P values were determined by unpaired two-sided t test. **c**, MA9 AML cells we implanted into WT mice and evaluated progression: 1) Ctrl (*Prmt9* WT), n = 7 mice; 2) *Prmt9* KD, n = 7 mice; 3) *Prmt9* KD with T cell depletion, n = 5 mice; 4) *Prmt9* KD with NK cell depletion, n = 5 mice. Kaplan-Meier curves show survival. P value was determined by log-rank (Mantel–Cox) test. **d**, following engraftment, 1 day prior to in-vivo DOX administration to KD Prmt9, mice are administered with anti-CD4/CD8 treatment or anti-NK1.1 to deplete T or NK cells. Plot of the depletion in PB was shown. **e**, Control or *Prmt9* KD MA9-luciferase cells were injected into wild-type B6 mice (1×10^6 cells per mouse, n = 5). Following engraftment, mice were treated with Dox in drinking water for 7 days. The plot shows the frequency of MA9, CD3 + , B220+ and Gr1 + /Mac1+ cells in BM of each mouse at the time of collection analyzed by flow-cytometry. BM and spleen cells from one representative mouse (with the frequency of each subset highlighted in red) in each group were selected and subjected to scRNA-seq analysis. Data are presented as mean ± SEM. P value of each comparison was determined by unpaired two-sided t test. **f**, identified populations in MA9 BM. **g**, Frequency of AML cells in BM. **h**–**j**, Different populations (h) and markers (i) identified within Ctrl and *Prmt9* KD groups merged in spleen cells. identified spleen populations are shown (j). **k**, T cell frequency in spleen cells. **l**, Expression of T cell marker genes in spleen. **m**, Frequency of Cd44+ cells in BM T cells. **n**, Frequency of Tregs (Foxp3+) in BM CD4 + T cells. **o**, Plot of leukemic BM in MA9 rechallenge. **p**, GSEA analysis of BM T cells. Normalized enrichment scores and family-wise error rate P-value was determined by the GSEA permutation method. The Normalized Enrichment Score is calculated by dividing the Enrichment Score from the actual ranking by the means of the random permutations. An enrichment P-value is calculated by comparing the observed frequency of an annotation term with the frequency expected by chance; individual terms beyond cut-off (p-value ≤ 0.05) are deemed enriched. **q**–**u**, (q-r) UMAP (q) and histogram (r) showing Isg15 expression in indicated BM subpopulation; (s-t) UMAP and histogram showing Ifit1 expression in indicated BM population; (u) Cxcl10 expression in indicated BM populations. Ctrl: T cells, n = 249 cells; Monocytes/Macrophages, n = 631 cells; DCs, n = 108 cells; Granulocytes, n = 3378 cells; B cells, n = 413 cells. *Prmt* KD: T cells, n = 231 cells; Monocytes/Macrophages, n = 469 cells; DCs, n = 57 cells; Granulocytes, n = 3906 cells; B cells, n = 134 cells. For (o, q, r), Data were mean ± SEM. P values were determined by unpaired two-sided t-tests.

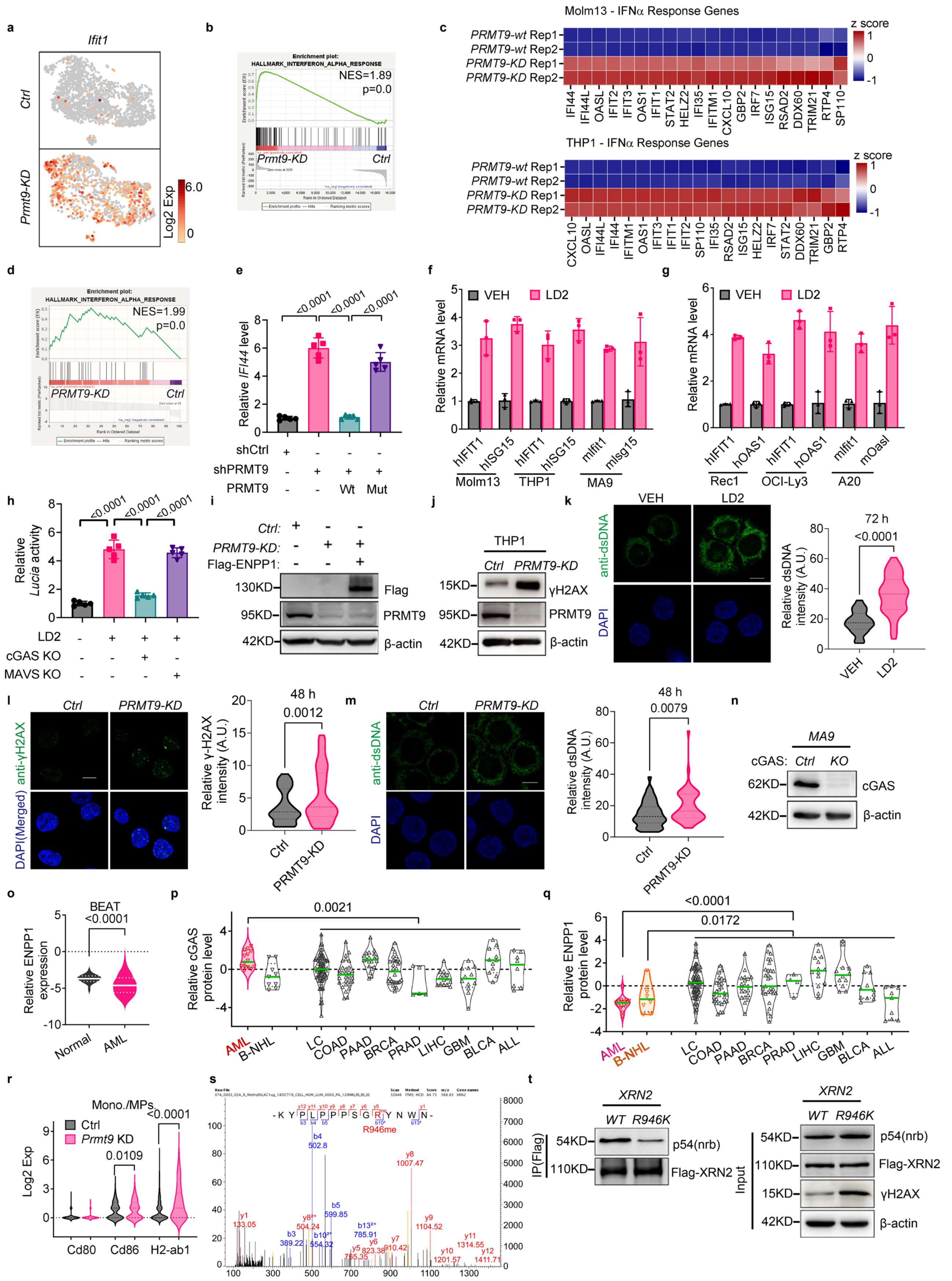

Extended Data Fig. 8 | See next page for caption.

Extended Data Fig. 8 | Immunity following PRMT9 inhibition requires cGAS activity. a, Ifit1 expression in AML cells from BM scRNA-seq. **b**, GSEA analysis of BM T cells. Normalized enrichment scores and family-wise error rate P-value was determined by the GSEA permutation method. **c, d**, RNA-seq of common DEG in *PRMT9* KD versus Ctrl cell lines. Heatmap (c) and GSEA (d) show upregulation of IFNα response genes upon *PRMT9* KD. The color code represents z scores for differential gene expression. For (b) and (d), the normalized enrichment scores and family-wise error rate P-value was determined by the GSEA permutation method. The Normalized Enrichment Score is calculated by dividing the Enrichment Score from the actual ranking by the means of the random permutations. An enrichment P-value is calculated by comparing the observed frequency of an annotation term with the frequency expected by chance; individual terms beyond cut-off (p-value ≤ 0.05) are deemed enriched. **e**, IFI44 expression in Molm13 engineered as indicated (n = 5 independent experiments). Data were mean ± SD. P value was determined by one-way ANOVA. **f, g**, Levels of selected ISG genes (f) in AML and B-NHL lines after 2 days LD2 treatment (n = 3 independent experiments). Data were presented as mean ± SD. **h**, Lucia activity of engineered THP1 after LD2 treatment (n = 5 independent experiments). Data were mean ± SD. P value was determined by one-way ANOVA. **i**, Levels of PRMT9 and Flag-tagged ENPP1 in engineered THP1 cells, (n = 1). **j**, Levels of γH2AX in THP1 cells, (n = 1). **k**, dsDNA by immunostaining in THP1 cells after LD2 treatment for 72 hr. Violin plots (right) summarized dsDNA intensity (n = 50 cells/group). Scale bar, 10 μm. **l**, Immunostaining for γH2AX in Ctrl and *PRMT9* KD THP1 cells. Violin plots (right) summarized γH2AX intensity (n = 100 cells/group). Scale bar, 10 μm. **m**, dsDNA by immunostaining in Ctrl and *PRMT9* KD THP1 cells. Violin plots (right) summarized dsDNA intensity (n = 50 cells/group). Scale bar, 10 μm. P values (k,l,m) were calculated by unpaired two-sided t test. **n**, Levels of cGAS in Ctrl and cGAS-KO MA9 cells (n = 2 independent experiments). **o**, ENPP1 mRNA levels in the BEAT AML (n = 451 AML cases; n = 19 healthy donors). The P value was by unpaired two-sided t test. **p-q**, cGAS and ENPP1 expression in AML and B-NHL lines compared with other cancer cell lines. AML (n = 14), B-NHL (n = 9), LC (n = 77), COAD (n = 30), PAAD (n = 20), BRCA (n = 30), PRAD (n = 5), LIHC (n = 14), GBM (n = 12), BLCA, (n = 11) and ALL (n = 8). P values were by unpaired two-sided t test. 'n' represents number of cell lines. **r**, Cd80, Cd86, H2-ab1 expression in monocytes/macrophages from BM, from scRNA-seq. Ctrl, n = 631 cells; *Prmt9* KD, n = 469 cells. Data were mean ± SEM. P values were determined by unpaired two-sided t-test. **s**, Representative spectrum of XRN2 R946 methylation in SILAC-based methyl-peptide quantitative LC-MS/MS. **t**, 293 T were transfected with Flag-tagged XRN2, then for immunoprecipitation and the interactor detected by immunoblot, (n = 1). γH2AX was detected in the input lysate.

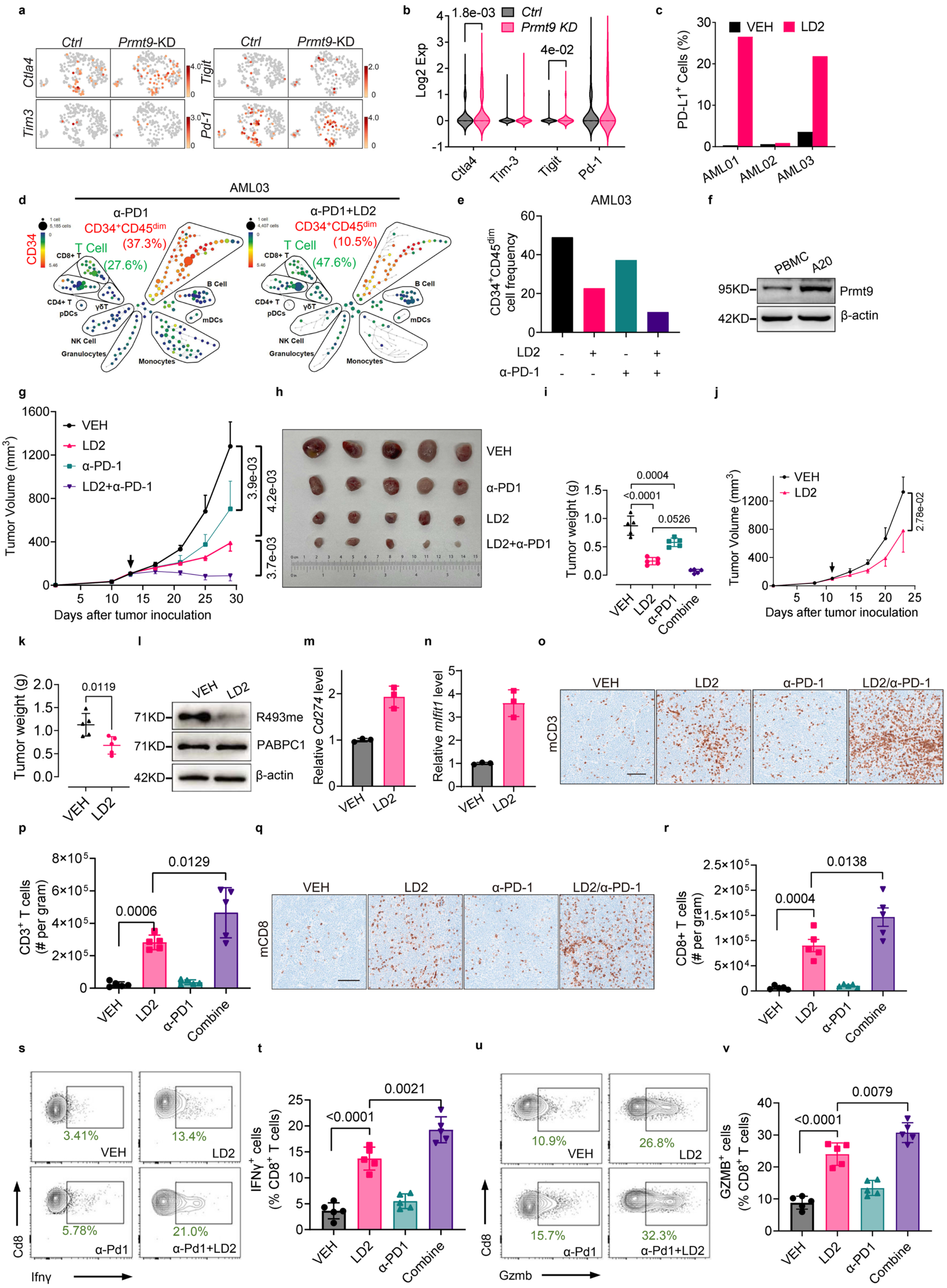

Extended Data Fig. 9 | See next page for caption.

Extended Data Fig. 9 | Combining LD2 with an ICI ablates cancers. **a, b**, UMAP (a) and histogram (b) showing indicated gene expression in T cells from scRNA-seq of Ctrl (n = 249 cells) and *Prmt9* KD (n = 231 cells) BM T cells. Data were mean ± SEM. P values were unpaired two-sided t-test. **c**, Frequency of PD-L1+ cells among leukemic subset (CD34+CD45dim) following treatment LD2 (2.5 μM, 4 days), n = 3 samples. **d, e**, CyTOF of AML MNCs after indicated treatment. The frequency of CD3 + T and CD34+CD45dim AML blasts were noted (d). Relative leukemia (CD34+CD45dim) cell frequencies of (d and right panel of Fig. 4m) were shown in (e). **f**, Prmt9 levels in normal mouse PBMCs or A20 (n = 2 independent experiments). **g, h**, Balb/C mice were inoculated with A20 cells (n = 5 mice/group). Tumor bearing mice were treated with isotype control (VEH), anti-PD1 mAb (10 mg/kg/i.p./q.o.d./2 wks), LD2 (100 mg/kg/ i.t./q.d./2 wks) or combination (n = 5 mice/group). Tumor volume was monitored (g) and pictures were acquired (h). **i**, Weight of A20 tumors in each group (n = 5 mice/group); **j, k**, *NSGS* mice (n = 10 mice) were inoculated with A20 cells. Tumor bearing mice were treated with vehicle or LD2 (100 mg/kg/i.t./ q.d./2 wks, n = 5 mice/group). Final tumor weights are shown (k). Data (g, i, j,k) were mean ± SEM. P values were determined by two-way ANOVA (g, j), one-way ANOVA (i) or unpaired two-sided t test (k). **l**, Levels of R493 methylation in A20 cells treated with LD2 (n = 2 independent experiments). **m, n**, Levels of Cd274 (m) and mIfit1 (n) cells in A20 treated with LD2 (n = 3 independent experiments). Data were mean ± SD. **o**, Representative image of anti-mCD3 IHC staining in indicated groups. Scale bar, 100 μm. **p**, Quantification of CD3 T cells, based on the number of cells per gram of tumor in indicated treatment groups (n = 5 mice/group). Data are presented as mean ± SD. P values were determined by one-way ANOVA. **q, r**, Representative image of anti-mCD8. Scale bar, 100 μm. (r) Quantification of CD8 T cells in indicated groups (n = 5 mice/group). **s–v**, Representative plots showing IFNγ (s) and GZMB (u) expression in CD8 + T cells in indicated treatment groups. Quantification of IFNγ + (t) and GZMB + (v) cells among CD8 + T cells in indicated groups (t, v- n = 5 mice/group). Data (r, t, v) are mean ± SEM. P values (r, t, v) were determined by one-way ANOVA.

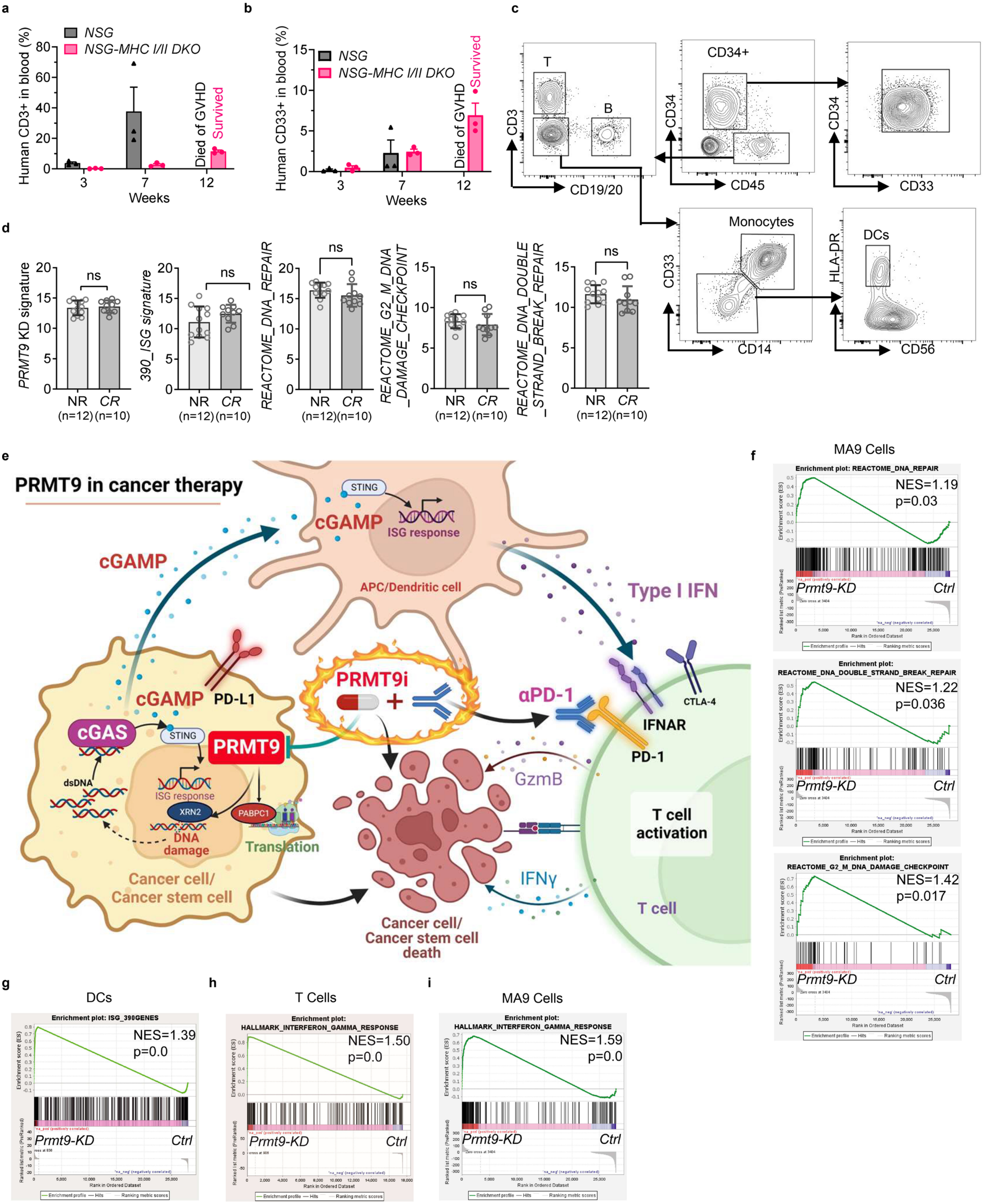

Extended Data Fig. 10 | See next page for caption.

https://doi.org/10.1038/s43018-024-00736-x

Extended Data Fig. 10 | Humanized AML mouse model establishment. **a, b**, Two million AML MNCs were implanted intra-femorally into an irradiated *MHCI/Il1/2* double-KO (*DKO*) *NSG* or regular *NSG* mice (n = 3 mice/group). After transplant, engraftment of CD3 + T cells, CD33+ cells in PB were monitored for 12 weeks. Then, BM engraftment of human hematopoietic subsets including T cells, monocytes and DCs, as well as the immature CD33 + CD34+CD45dim subset were assessed. Data were mean ± SEM. **c**, Representative gating of hematopoietic subsets from *DKO* mouse BM. **d**, Single sample gene set enrichment analysis (ssGSEA) of AML trial dataset GSE183415 which contains samples with clinical responses to PD-1 inhibitors (Complete Response [CR, n = 10] vs. No Response [NR, n = 12]) using the following gene signature: *PRMT9* KD signature, 390 ISG signature, Reactome DNA repair signature, Reactome Double strand break repair signature, and Reactome G2M DNA damage checkpoint signature. 'n' represents patient numbers in indicated group. Data are presented as mean ± SD, statistical comparisons were performed using unpaired two-sided t-test, 'ns' indicates no significance. **e**, Proposed model. **f**, 'REACTOME' signature 'DNA Repair', 'DNA Double Strand Break Repair', 'G2M DNA Damage Checkpoint' plots of GSEA of MA9 AML cells (*Prmt9* KD vs. Ctrl). **g**, 390 ISGs genes signature plot of GSEA of BM DCs (*Prmt9* KD vs. Ctrl). **h**, 'Hallmarks' signature Interferon Gamma Response plot of GSEA of BM T cells (*Prmt9* KD vs. Ctrl). **i**, 'Hallmarks' signature Interferon Gamma Response plot of GSEA of BM MA9 AML cells (*Prmt9* KD vs. Ctrl). For GSEA analysis (g-i), Normalized enrichment scores and family-wise error rate P-value was determined by the GSEA permutation method. The Normalized Enrichment Score is calculated by dividing the Enrichment Score from the actual ranking by the means of the random permutations. An enrichment P-value is calculated by comparing the observed frequency of an annotation term with the frequency expected by chance; individual terms beyond cut-off (p-value ≤ 0.05) are deemed enriched.

Corresponding author(s): Ling Li

Last updated by author(s): Jan 17, 2024

Reporting Summary

Statistics

For all statistical analyses, confirm that the following items are present in the figure legend, table legend, main text, or Methods section.

n/a	Confirmed	
☐	☒	The exact sample size (*n*) for each experimental group/condition, given as a discrete number and unit of measurement
☐	☒	A statement on whether measurements were taken from distinct samples or whether the same sample was measured repeatedly
☐	☒	The statistical test(s) used AND whether they are one- or two-sided *Only common tests should be described solely by name; describe more complex techniques in the Methods section.*
☒	☐	A description of all covariates tested
☐	☒	A description of any assumptions or corrections, such as tests of normality and adjustment for multiple comparisons
☐	☒	A full description of the statistical parameters including central tendency (e.g. means) or other basic estimates (e.g. regression coefficient) AND variation (e.g. standard deviation) or associated estimates of uncertainty (e.g. confidence intervals)
☐	☒	For null hypothesis testing, the test statistic (e.g. *F*, *t*, *r*) with confidence intervals, effect sizes, degrees of freedom and *P* value noted *Give P values as exact values whenever suitable.*
☒	☐	For Bayesian analysis, information on the choice of priors and Markov chain Monte Carlo settings
☒	☐	For hierarchical and complex designs, identification of the appropriate level for tests and full reporting of outcomes
☐	☒	Estimates of effect sizes (e.g. Cohen's *d*, Pearson's *r*), indicating how they were calculated

Our web collection on statistics for biologists contains articles on many of the points above.

Software and code

Policy information about availability of computer code

Data collection	BD FACSDiva(V.8.0) was used to collect flow cytometric data. Aura 4.0.0 was used to collect in vivo Bioluminescence imaging data. GeneSys image acquisition software v1.5.7.0 (Syngene) was used to collect DNA gels and western blots data.
Data analysis	GraphPad Prism 9 was used to generate graphs for in vitro and in vivo assays. FlowJo (v10.8.0) was used for flow cytometric analysis. Image) software v1.53s was used to analyze the relative protein levels in western blot results. MaxQuant v1.6.17.0 was used for SILAC analysis. Cytobank software v10.3 (https://premium.cytobank.org/) was used for CyTOF analysis. Bruker stddiffgp19.3 was used for STD results analysis. Bruker Topspin 3.6 was used for CPMG results analysis. Cell Ranger v6.1.1, R version 4.0.2, package, Seurat v4.0, Harmony v1.1.0, MAST v1.26.0, SingleR v2.2.0 were used for single cell RNAseq analysis. GSEA v4.0.3, Tophat2 v2.0.8, HTseq v0.11.2, edgeR v.3.30.3, Cluster v3.0 were used for bulk RNA seq analysis. Interaction analysis of proteins carrying PRMT9-regulated R-methyl peptides was visualized by Cytoscape 3.10.1. Please see Methods section in manuscript for further details.

For manuscripts utilizing custom algorithms or software that are central to the research but not yet described in published literature, software must be made available to editors and reviewers. We strongly encourage code deposition in a community repository (e.g. GitHub). See the Nature Portfolio guidelines for submitting code & software for further information.

Data

Policy information about availability of data

All manuscripts must include a data availability statement. This statement should provide the following information, where applicable:

- Accession codes, unique identifiers, or web links for publicly available datasets
- A description of any restrictions on data availability
- For clinical datasets or third party data, please ensure that the statement adheres to our policy

All data supporting the findings of this study are available within the article and its Supplementary Information. Human AML cells Molm13 and THP1 RNA-seq raw data and Murine single-cell RNA-seq raw data have been deposited in the GEO database under accession code: GSE217195 and GSE217396. PRMT9 SILAC proteomics data have been deposited to PRIDE with he accession number: PXD039441. Previously published datasets and information info are available with the following links and accession codes: https://DepMap.org/portal/; https://www.cbioportal.org/ (TCGA PanCancer Atlas Studies); http://cancergenome.nih.gov/ (TCGA Research Network, pan-kidney transcriptomic, genomic and clinical data); BEAT AML dataset (http://vizome.org/aml/); https://servers.binf.ku.dk/bloodspot/ (BloodSpot); GEPIA (http://gepia.cancer-pku.cn/); TARGET-AML, GSE14468, GSE12417, GSE63270, GSE183415. Source data are provided with this paper. Requests for resources and reagents can be directed to the lead contact L.L.

Human research participants

Policy information about studies involving human research participants and Sex and Gender in Research.

Reporting on sex and gender	Sex and gender were not relevant in this study.
Population characteristics	Humanspecimens were obtained from the Hematopoietic tissue bank at City of Hope. The covariants associated with each sample were not obtained as they were not relevant for this study.
Recruitment	Participants were recruited by the Hematopoietic tissue bank as part of a standard procedure with informed content and no potential bias.
Ethics oversight	All subjects signed informed consent forms. Sample acquisition was approved by the COH Institutional Review Board in accordance with the Helsinki Declaration.

Note that full information on the approval of the study protocol must also be provided in the manuscript.

Field-specific reporting

Please select the one below that is the best fit for your research. If you are not sure, read the appropriate sections before making your selection.

☒ Life sciences ☐ Behavioural & social sciences ☐ Ecological, evolutionary & environmental sciences

For a reference copy of the document with all sections, see nature.com/documents/nr-reporting-summary-flat.pdf

Life sciences study design

All studies must disclose on these points even when the disclosure is negative.

Sample size	No sample size was pre-determined. Sample size and number of independent experiments are stated in the figure legend or in the Methods or Results section. Three or more independent results were used to perform statistical analyses. Studies involving independent cohorts of mice were typically performed once, with several exceptions stated in the figure legends. No specific statistical tests were applied to determine the sample size, the size was established according to our previous experience with the models used. Accordingly, we typically employed experimental cohorts of five to seven mice.
Data exclusions	No data were excluded from the analyses.
Replication	Replicates were used in all experiments as indicated in text, figure legends and methods. Animal experiments have been repeated as indicated in the figure legends. All other experiments have been repeated at least twice with consonant results. All attempts at replication were successful.
Randomization	The experiments were not randomized.
Blinding	Blinding was not done due to the requirements for case labeling and staffing needs, as knowledge of the grouping information was essential for the staff to conduct the studies.

Reporting for specific materials, systems and methods

We require information from authors about some types of materials, experimental systems and methods used in many studies. Here, indicate whether each material, system or method listed is relevant to your study. If you are not sure if a list item applies to your research, read the appropriate section before selecting a response.

Materials & experimental systems

n/a	Involved in the study
☐	☒ Antibodies
☐	☒ Eukaryotic cell lines
☒	☐ Palaeontology and archaeology
☐	☒ Animals and other organisms
☒	☐ Clinical data
☒	☐ Dual use research of concern

Methods

n/a	Involved in the study
☒	☐ ChIP-seq
☐	☒ Flow cytometry
☒	☐ MRI-based neuroimaging

Antibodies

Antibodies used	Anti-human CD3(BioLegend, Cat#317320; RRID:AB_10916519, 1:100); Anti-human CD45(BioLegend, Cat#368512; RRID:AB_2566372, 1:100); Anti-human CD33(BioLegend, Cat#366608; RRID:AB_2566107, 1:100); Anti-human CD71(BioLegend, Cat#334110; RRID:AB_2563117, 1:100); Anti-human CD11b(BioLegend, Cat#301322; RRID:AB_830644, 1:100); Anti-mouse CD11b(BioLegend, Cat#101212; RRID:AB_312795, 1:100); Anti-mouse CD3(BioLegend, Cat#100206; RRID:AB_312663, 1:100); Anti-mouse CD34(BioLegend, Cat#119310; RRID:AB_1236469, 1:100); Anti-mouse Sar1(BioLegend, Cat#108108; RRID:AB_313345, 1:100); Anti-mouse Ter119(BioLegend, Cat#116244; RRID:AB_2565872, 1:100); Annxin V(BioLegend, Cat#640920; RRID:AB_2561515, 1:100); Anti-human CD19(eBioscience, Cat#13-0199-82; RRID:AB_466388, 1:100); Anti-human CD34(eBioscience, Cat#47-0349-42; RRID:AB_2573956, 1:100); Anti-human CD38(eBioscience, Cat#11-0388-42; RRID:AB_10547895, 1:100); Anti-human CD14(eBioscience, Cat#45-0149-42; RRID:AB_1518736, 1:100); Anti-human CD15(eBioscience, Cat#48-0159-42; RRID:AB_2016661, 1:100); Anti-human CD45(eBioscience, Cat#48-9459-42; RRID:AB_1603240, 1:100); Anti-mouse CD3(eBioscience, Cat#13-0032-82; RRID:AB_2572762, 1:100); Anti-mouse CD4(eBioscience, Cat#13-0041-85; RRID:AB_466326, 1:100); Anti-mouse CD8a(eBioscience, Cat#13-0081-85; RRID:AB_466347, 1:100); Anti-mouse B220(eBioscience, Cat#13-0452-85; RRID:AB_466450, 1:100); Anti-mouse IGM(eBioscience, Cat#13-5790-85; RRID:AB_466676, 1:100); Anti-mouse CD19(eBioscience, Cat#13-0193-85; RRID:AB_657658, 1:100); Anti-mouse CD11b(eBioscience, Cat#13-0112-85; RRID:AB_466360, 1:100); Anti-mouse CD11c(eBioscience, Cat#13-0114-82; RRID:AB_466363, 1:100); Anti-mouse NK1.1(eBioscience, Cat#13-5941-85; RRID:AB_466805, 1:100); Anti-mouse GR1(eBioscience, Cat#13-5931-85; RRID:AB_466801, 1:100); Anti-mouse Ter119(eBioscience, Cat#13-5921-85; RRID:AB_466798, 1:100); Anti-mouse CD127(eBioscience, Cat#13-1271-82; RRID:AB_466588, 1:100); Anti-mouse GR1(eBioscience, Cat#12-5931-82; RRID:AB_466045, 1:100); Anti-mouse CD117(eBioscience, Cat#47-1172-82; RRID:AB_1582226, 1:100); Anti-mouse CD45.2(eBioscience, Cat#11-0454-85; RRID:AB_465062, 1:100); APC anti-mouse CD34 Antibody(Biolegend, Cat#119310, 1:100); Brilliant Violet 605 anti-mouse Ly-6A/E (Sca-1) Antibody(Biolegend, Cat#108134, 1:100); APC/Cyanine7 anti-mouse CD117 (c-kit) Antibody(Biolegend, Cat#135136, 1:100); PE/Cy7 anti-mouse CD16/32 Antibody(Biolegend, Cat#101318, 1:100); Brilliant Violet 605 Streptavidin(Biolegend, Cat#405229, 1:100); APC Annexin V(Biolegend, Cat#640941, 1:100); percp/cyanin5.5 anti-human CD14(Biolegend, Cat#325622, 1:100); APC anti-human CD45(Biolegend, Cat#368512/2D1, 1:100); PE/CY7 anti-human CD11B(Biolegend, Cat#301322/ICRF44, 1:100); FITC anti-human CD15 (SSEA-1) Antibody(Biolegend, Cat#301904/HI98, 1:100); APC anti-mouse CD115(Biolegend, Cat#135510, 1:100); APC/CY7 anti-mouse CD3(Biolegend, Cat#100222, 1:100); CD11B-APC anti-mous and human clone:M1/70(Biolegend, Cat#101212, 1:100); Pacific Blue Anti-mouse Ly-6G/Ly-6C (Gr-1) Clone RB6-8C5(Biolegend, Cat#108430, 1:100); APC/Cyanine7 anti-human CD34(Biolegend, Cat#343614, 1:100); FITC Annexin V(Biolegend, Cat#640906, 1:100); FITC anti-human CD38 Antibody(Biolegend, Cat#356610, 1:100); FITCBV421 anti-human CD15 (SSEA-1) Antibody(Biolegend, Cat#323040/W6D3, 1:100); PE anti-mouse IFN-γ Antibody(Biolegend, Cat#505807, 1:100); FITC anti-human/mouse Granzyme B Recombinant Antibody(Biolegend, Cat#372205, 1:100); Pacific Blue™ anti-mouse CD8a Antibody(Biolegend, Cat#100728, 1:100); APC anti-mouse NK-1.1 Antibody(Biolegend, Cat#108709, 1:100); PE/Cyanine7 anti-mouse CD45.1 Antibody(Biolegend, Cat#110730, 1:100); Alexa Fluor® 700 anti-mouse CD4 Antibody(Biolegend, Cat#100429, 1:100); Alexa Fluor® 700 anti-human CD4 Antibody(Biolegend, Cat#300526, 1:100); Brilliant Violet 605™ anti-human CD8a Antibody(Biolegend, Cat#301039, 1:100); Pacific Blue™ anti-human CD14 Antibody(Biolegend, Cat#301816, 1:100); PE anti-human CD197 (CCR7) Antibody(Biolegend, Cat#353203, 1:100); FITC anti-human CD25 Antibody(Biolegend, Cat#356105, 1:100); PE/Cyanine7 anti-human HLA-DR Antibody(Biolegend, Cat#307615, 1:100); Pacific Blue™ anti-mouse CD45.2 Antibody(Biolegend, Cat#109819, 1:100); PE anti-human CD16(Biolegend, Cat#980102, 1:100); BV510- mouse anti-human CD38 Antibody(Biolegend, Cat#356611, 1:100); AF700 anti-mouse CD4 antibody(Biolegend, Cat#100430, 1:100); PE anti-human IFN-gamma Antibody(Biolegend, Cat#506506, 1:100); Purified anti-human FOXP3 Antibody(Biolegend, Cat#320102, 1:100); Pacific Blue anti-mouse/human CD11b Antibody(Biolegend, Cat#101224, 1:100); FITC anti-human CD279 (PD-1)(Biolegend, Cat#329903, 1:100); PE/Dazzle 594 anti-human CD152 (CTLA-4)(Biolegend, Cat#369615, 1:100); Pacific Blue anti-human CD366 (Tim-3)(Biolegend, Cat#345041, 1:100); PE/Cyanine7 anti-human TIGIT (VSTM3)(Biolegend, Cat#372713, 1:100); FITC anti-mouse CD279 (PD-1) Antibody(Biolegend, Cat#135213, 1:100); PE/Cyanine7 anti-mouse CD223 (LAG-3) Antibody(Biolegend, Cat#125226, 1:100); Brilliant Violet 605™ anti-mouse CD152 Antibody(Biolegend, Cat#106323, 1:100); Alexa Fluor® 647 anti-mouse CD366 (Tim-3) Antibody(Biolegend, Cat#119744, 1:100): PE/Dazzle™ 594 anti-mouse TIGIT (Vstm3) Antibody(Biolegend, Cat#142110, 1:100): APC anti-human CD15 (SSEA-1) Antibody(Biolegend, Cat#301908, 1:100); PE/Dazzle™ 594 anti-mouse CD69 Antibody(Biolegend, Cat#104536, 1:100); APC/Cyanine7 anti-human CD3 Antibody (SK7)(Biolegend, Cat#344818, 1:100); PE anti-human CD56 (NCAM) Antibody(Biolegend, Cat#362508, 1:100); APC anti-mouse NK-1.1 Antibody (S17016D) (Biolegend, Cat#156506, 1:100); Pacific Blue™ anti-human CD16 Antibody(Biolegend, Cat#302024, 1:100); Alexa Fluor® 700 anti-human CD20 Antibody(Biolegend, Cat#302322, 1:100); PE/Dazzle™ 594 anti-human CD34 Antibody(Biolegend, Cat#343533, 1:100); Brilliant Violet 605™ anti-mouse CD25 Antibody(Biolegend, Cat#102036, 1:100); PE anti-mouse/human CD44 Antibody(Biolegend, Cat#103024, 1:100); PE/Cyanine7 anti-mouse CD62L Antibody(Biolegend, Cat#104418, 1:100); Pacific Blue™ anti-mouse FOXP3

	Antibody(Biolegend, Cat#126410, 1:100); PE/Cyanine7 anti-human/mouse Granzyme B Recombinant Antibody(Biolegend, Cat#372214, 1:100); Brilliant Violet 605™ anti-mouse CD8a Antibody(Biolegend, Cat#100744, 1:100); Mouse mAb anti-β-Actin(Cell Singaling Technology, Cat#3700S; RRID:AB_2242334, 1:2000); Rabbit mAb anti-HSP90(Cell Singaling Technology, Cat#4877S; RRID:AB_2233307, 1:2000); Rabbit mAb anti-H3K27ac(Abcam, Cat#ab4729; RRID:AB_2118291, 1:1000); Rabbit mAb anti-Histon H3(Cell Singaling Technology, Cat#4499S; RRID:AB_10544537, 1:1000); Rabbit pAb anti-Histon H4(Abcam, Cat#ab10158; RRID:AB_296888, 1:1000); Rabbit pAb anti-HA tag(Abcam, Cat#ab9110; RRID:AB_307019, 1:2000); Mouse mAb anti-FLAG(Sigma-aldrich, Cat#F1804; RRID:AB_262044, 1:5000); Mouse mAb anti-Myc(Santa Cruz, Cat#sc-40; RRID:AB_627268, 1:1000); Rabbit pAb anti-PABPC1-R493me(This paper, 1:1000); Rabbit pAb anti-PABPC1-R493 Ctrl(This paper, 1:1000); Mouse mAb anti-CREB1(Santa Cruz Cat#sc-240; RRID:AB_627302, 1:1000); Rabbit pAb anti-mouse Prmt9(This paper, 1:1000); Mouse mAb anti-human PRMT9(Millipore, Cat#MABE1112; RRID:AB_2801509, 1:1000); Rabbit anti-SAMHD1(Proteintech, Cat#12586-1-AP; RRID:AB_2183496, 1:1000); Rabbit anti-RUNX1(Proteintech, Cat#25315-1-AP; RRID:AB_2880026, 1:1000); Rabbit mAb anti-CEBPA(Cell Singaling Technology, Cat#8178T, 1:1000); Rabbit anti-pan-MMA(Cell Singaling Technology, Cat#8015S; RRID:AB_10891776, 1:1000); Rabbit anti-pan-SDMA(Cell Singaling Technology, Cat#13222S; RRID:AB_2714013, 1:1000); Rabbit anti-pan-ADMA(Cell Singaling Technology, Cat#13522S; RRID:AB_2665370, 1:1000); Rabbit anti-PABPC1(Cell Singaling Technology, Cat#4992; RRID:AB_10693595, 1:1000); Mouse mAb anti-PABPC1(Santa Cruz, Cat#sc-32318; RRID:AB_628097, 1:1000); Rabbit anti-PRMT1(Cell Singaling Technology, Cat#2449S; RRID:AB_2237696, 1:1000); Rabbit mAb anti-PRMT5(Abcam, Cat#ab109451; RRID:AB_10863428, 1:2000); Rabbit mAb anti-MEP50(Abcam, Cat#ab154190, 1:1000); Rabbit mAb anti-CARM1(Cell Singaling Technology, Cat#3379S; RRID:AB_2068433, 1:1000); Rabbit anti-GST(Proteintech, Cat#10000-0-AP;RRID:AB_11042316, 1:3000); Rabbit mAb anti-PABPC1 R455/R460me(Cell Singaling Technology, Cat#3505S; RRID:AB_2298971, 1:1000); Rabbit anti-FLT3 (S-18)(Santa Cruz, Cat#sc-480; RRID:AB_2104968, 1:1000); FLT3 R972/R973me(Xin He et al., 2018, 1:1000); Rabbit pAb anti-H3R8me(Abcam, Cat#ab130740; RRID:AB_2801510, 1:1000); Rabbit mAb anti-p54(nrb)(Cell Singaling Technology, Cat#10162S, 1:1000); Rabbit mAb anti-γH2AX(Cell Singaling Technology, Cat#9718S; RRID:AB_2118009, 1:1000); Rabbit mAb anti-cGAS(Cell Singaling Technology, Cat#79978S; RRID:AB_2905508, 1:1000); Rabbit mAb anti-XRN2(Cell Singaling Technology, Cat#13760S; RRID:AB_2798309, 1:1000); Rabbit mAb anti-pCHK1 (S345)(Cell Singaling Technology, Cat #2348, 1:1000); Rabbit mAb anti-CHK1(Cell Singaling Technology, Cat #37010, 1:1000); Rabbit mAb anti-pCHK2 (T68)(Cell Singaling Technology, Cat#2197, 1:1000); Rabbit mAb anti-CHK2(Cell Singaling Technology, Cat#6334, 1:1000); Rabbit pAb anti-DDX3X(Millipore Cat#09-860; RRID:AB_1977147, 1:1000); InVivoMAb anti-mouse PD-1 (CD279)(BioXCell, Cat#BE0146; RRID:AB_10949053).
Validation	The antibodies used are established in the field and have been used by a number of groups. RRID was provided in antibody information listed above.

Eukaryotic cell lines

Policy information about cell lines and Sex and Gender in Research

Cell line source(s)	Molm13 (ACC 554, DSMZ), MV4-11 (CRL-9591, ATCC), THP1 (TIB-202, ATCC), NB4 (ACC 207, DSMZ), U937 (CRL-1593.2, ATCC), HL-60 (CCL-240, ATCC), and MA9.6ITD (Gift from Dr. James Mulloy), RAJI (ACC 319, DSMZ), UPN1 (CVCL_A795, Cellosaurus), BL41 (ACC 160, DSMZ), Rec1 (ACC 584, DSMZ), OCI-Ly3 (ACC 761, DSMZ), A20 (Gift from Dr. Yangxin Fu), HEK293FT (R70007, Thermo Fisher), DMS273 (Gift from Dr. Ravi Salgia), DMS114 (Gift from Dr. Ravi Salgia), SW1573 (Gift from Dr. Edward Wang), A549 (Gift from Dr. Edward Wang), SW620 (CCL-227, ATCC), HCT116 (CCL-247, ATCC), HepG2 (HB-8065, ATCC), PC3 (Gift from Dr. Saul Priceman), DU145 (Gift from Dr. Saul Priceman), MDA-MB-231 (CRM-HTB-26, ATCC), HT1197 (CRL-1473, ATCC), A172 (CRL-1620, ATCC), MIAPACA2 (CRM-CRL-1420, ATCC), and HT1080 (CCL-121, ATCC)
Authentication	MA9.6ITD were established by Dr. James Mulloy. DMS273 and DMS114 are gift from Dr. Ravi Salgia, SW1573 and A549 are gift from Dr. Edward Wang, PC3 and DU145 are gift from Dr. Saul Priceman. A20 is gift from Dr. Yangxin Fu. These cells were not authenticated further. All other cell lines are from ATCC, DSMZ, Thermo Fisher, or Cellosaurus.
Mycoplasma contamination	All cell lines were tested negative for mycoplasma.
Commonly misidentified lines (See ICLAC register)	A549 was gift from Dr. Edward Wang, PC3 and DU145 were gift from Dr. Saul Priceman.

Animals and other research organisms

Policy information about studies involving animals; ARRIVE guidelines recommended for reporting animal research, and Sex and Gender in Research

Laboratory animals	In all the experiments, male and female, 6-10 wks old, WT C57BL/6J (JAX #000664), B6(Cg)-Rag2tm1.1Cgn/J (JAX #008449, Rag2-/-), B6(Cg)-Ifnar1tm1.2Ees/J (JAX #028288, Ifnar1-/-), Kmt2atm2(MLLT3)Thr/KsyJ (JAX #009079, MLL-AF9 knockin), B6.129S(C)-Batf3tm1Kmm/J (JAX #013755, Batf3-/-), NOD.Cg-Prkdcscid Il2rgtm1Wjl/SzJ (JAX #005557, NSG), NOD.Cg-Prkdcscid Il2rgtm1Wjl Tg(CMV-IL3,CSF2,KITLG)1Eav/MloySzJ (JAX #013062, NSGS), and NOD.Cg-Prkdcscid H2-K1tm1Bpe H2-Ab1em1Mvw H2-D1tm1Bpe Il2rgtm1Wjl/SzJ JAX #025216, NSG-MHC I/II DKO) mice, B6-Ly5.1 (CD45.1, NCI 564) and BALB/c (NCI 028) mice were available from outside vendor. Male and female mice were housed at the COH Animal Resource Center. All care and experimental procedures followed established institutional guidelines. Mouse room is conditioned at 14-hour light/10-hour dark cycle, temperatures of 65-75° F with 40-60 humidity. The procedure was in accordance with a protocol approved by the Institutional Animal Care and Use Committee at COHCCC.
Wild animals	No wild animals used in this study.
Reporting on sex	Sex and genders were not considered in this study design.
Field-collected samples	No field-collected samples in this study.

Ethics oversight	Mice purchased were acclimated to housing conditions for at least one week at the COH Animal Resource Center prior to experiments. Colonies for each mouse strain were maintained in the same animal facility. All mouse experiments procedures were completed in accordance with the Guidelines for the Care and Use of Laboratory Animals and were approved by the Institutional Animal Care and Use Committees at COHCCC. The experiments were performed in accordance with a protocol approved by the COHCCC Institutional Animal Care and Use Committees (15046). The maximal tumor size (humane endpoint) permitted by IACUC is 15mm (diameter). All the animals were euthanized before the tumor size reached 15mm in diameter. All our animals' maximal tumor size did not exceed 15mm.

Note that full information on the approval of the study protocol must also be provided in the manuscript.

Flow Cytometry

Plots

Confirm that:

☒ The axis labels state the marker and fluorochrome used (e.g. CD4-FITC).

☒ The axis scales are clearly visible. Include numbers along axes only for bottom left plot of group (a 'group' is an analysis of identical markers).

☒ All plots are contour plots with outliers or pseudocolor plots.

☒ A numerical value for number of cells or percentage (with statistics) is provided.

Methodology

Sample preparation	BM was obtained from mouse tibias and femurs of both legs by aspiration. Spleens were removed from mice and pressed with the end of a syringe. Cells were washed with PBS containing 1% FBS and then passed through a 70-µm cell strainer and subjected to lysis of red blood cells. Before flow cytometry analysis, cells were washed twice in PBS containing 1% FBS and stained with indicated antibodies in the same buffer for 25 minutes at 4°C.
Instrument	BD LSRFortessa X-20; BD LSR II; BD Fusion
Software	BD FACSDiva Software (version 8.0); FlowJo (v10.8.0)
Cell population abundance	The abundance of the relevant cell populations within post-sort fractions were determined by analyzing again using BD Fusion, Fortessa X-20 or LSR II.
Gating strategy	All samples are FSC-A and SSC-A gated, followed by FSC-A/FSC-H, SSC-A/SSC-H gating to select singlets. Subsequent relevant gating was set based on appropriate compensation using single-stained compensation controls.

☒ Tick this box to confirm that a figure exemplifying the gating strategy is provided in the Supplementary Information.